



THE HONG KONG
POLYTECHNIC UNIVERSITY

香港理工大學

Pao Yue-kong Library

包玉剛圖書館

Copyright Undertaking

This thesis is protected by copyright, with all rights reserved.

By reading and using the thesis, the reader understands and agrees to the following terms:

1. The reader will abide by the rules and legal ordinances governing copyright regarding the use of the thesis.
2. The reader will use the thesis for the purpose of research or private study only and not for distribution or further reproduction or any other purpose.
3. The reader agrees to indemnify and hold the University harmless from and against any loss, damage, cost, liability or expenses arising from copyright infringement or unauthorized usage.

IMPORTANT

If you have reasons to believe that any materials in this thesis are deemed not suitable to be distributed in this form, or a copyright owner having difficulty with the material being included in our database, please contact lbsys@polyu.edu.hk providing details. The Library will look into your claim and consider taking remedial action upon receipt of the written requests.

**DEVELOPMENT OF NOVEL CROSSFLOW ULTRAFILTRATION
MODULE INTEGRATED WITH ULTRASONIC TRANSDUCERS FOR
HERBAL EXTRACTS PURIFICATION**

WANG SAN JU

Ph.D

The Hong Kong Polytechnic University

2012



Department of Applied Biology and Chemical Technology

**DEVELOPMENT OF NOVEL CROSSFLOW ULTRAFILTRATION
MODULE INTEGRATED WITH ULTRASONIC TRANSDUCERS FOR
HERBAL EXTRACTS PURIFICATION**

WANG SAN JU

A thesis submitted
in partial fulfilment of the requirements
for the degree of
Doctor of Philosophy

June 2011

CERTIFICATE OF ORIGINALITY

I hereby declare that this thesis is my own work and that, to the best of my knowledge and belief, it reproduces no material previously published or written, nor material that has been accepted for the award of any other degree or diploma, except where due acknowledgement has been made in the text.

_____ (Signed)

WANG SAN JU (Name of student)

ABSTRACT

A major obstacle of applying membrane filtration for purification and separation of herbal extracts is the rapid decline of permeate flux resulting from membrane fouling. With the addition of ultrasound (US) irradiation, the combination effects of acoustic cavitation, microstreaming and micro-jets are capable of keeping the particle away from membrane surface to elevate filtration efficiency. However, with conventional configuration, only 10% of ultrasonic intensity can transmit into the membrane filtration channel when propagating through housing material. Rather than immersing crossflow (CF) module into ultrasonic bath, in our study, a customized CF module integrated with ultrasonic transducers was fabricated and operated in stainless steel water bath. A resistance in series model was adapted to evaluate the fouling profile of polysaccharides suspension derived from *Radix Astragalus* water extracts (RAE). The filtration enhancement factor increased significantly from 1.31 to 2.95 with 28 KHz at 200W input comparing to previous conventional setup. With either continuous or intermitted mode of ultrasonic irradiation, DI-H₂O flux of 30 kDa PES membrane recovered to 100% after water flushing. The fouling profile of polysaccharides extract was dominated by reversible fouling taking up to 80% of total resistance. US irradiation dramatically decreased not only the reversible fouling contributed by cake layer and concentration polarization but also the irreversible fouling caused by pore blocking. Evidence was presented by the detected sonic acoustic pressure distribution inside the crossflow channel. The morphology of fouled membrane and ultrasonic irradiated fouled membrane were characterized using SEM. Furthermore, polysaccharides MW and MW distribution of tested solutions were investigated with GPC.

In order to further improve the filtration efficiency, polypropylene permeate spacer was replaced by stainless steel (S.S.) permeate spacers with various porosities. Six sets of S.S. permeate spacers were inserted into CF module to evaluate the effect of porosity on permeate flux as well as on RAE filtration enhancement when irradiating with ultrasound in both US enhanced and integrated system. Without proper support to membrane, higher frictional resistance as well as localized turbulent induced by flow across the membrane surface became reasons for significant DI-H₂O flux loss. In the contrast, under the irradiation of US, these reasons turned into positive driving forces for enhanced permeation. The relative RAE filtration enhancement factors presented completely contrary tendencies for the two CF systems when plotting as the function of spacer porosity. The different mechanisms of US effect in these two CF systems played important role. By simply replacing the PP spacer with S.S spacer in permeate channel, the RAE filtration enhancement increased 28% more in US enhanced system and 45% more in US integrated system.

Response Surface Methodology (RSM) coupled with Box–Behnken design (BBD) of experiments were employed to investigate the effects of control variables (ultrasound output power, porosity of permeate spacer and transmembrane pressure) on the absolute permeate collection for RAE Ultrafiltration in US integrated CF system. The optimal operational conditions established by RSM and desirability function approach were as follow: a US output power of 120W, a spacer porosity of 60.8% and a TMP of 20 psi. By applying these process parameter values, maximal responses have been predicted. Under these conditions, the permeation efficiency can be improved up to 211%.

PUBLICATIONS

Refereed journal articles:

- Cai, M., Wang, S.J., Zheng, Y.P. and Liang, H.H. Effect of ultrasound on ultrafiltration of *Radix Astragalus* extracts and cleaning of fouled membrane, Separation and Purification Technology. Vol. 68, pp. 351-356 (2009)

Conference presentations:

- Wang, S.J. and Liang, H.H. Ultrasound enhanced crossflow Ultrafiltration for the purification of polysaccharides in Huang Qi extracts. Proceedings. International Conference of Natural Products and Traditional Medicine. Xi'An, China, 16-18 Oct. 2009
- Wang, S.J. and Liang, H.H. Development of novel crossflow Ultrafiltration Module integrated with Ultrasonic transducers for herbal extracts. Proceedings. 6th Conference of Aseasian Membrane Society. Sydney, Australia, 22-24 Nov. 2010

ACKNOWLEDGEMENTS

I would like to express my gratitude to all those who gave me the possibility to complete this thesis.

The preparation of this document would not have been possible without the guidance and support from Dr. HanHua Liang, my chief research supervisor. I would like to thank for his trust and inspiration throughout the study, for helping me set clear objectives, for encouraging me deal with difficulties and unexpected problems, for guiding me all the time of research and writing of this thesis.

I am particularly grateful for my co-workers, Ming Cai and Qun Chen. The coordination and interaction in the team created an interest and instructive learning environment.

My appreciation also goes to colleagues from the Department of ABCT. I want to thank them for all their help, support, interest and valuable hints. Especially I am obliged to Monica Kwok, Fiona Tong and Peggy Kwok in department office; Yiukwok Au and Yuiwah Shui in technical laboratory. The support from industry centre has been instrumental in facilitating the experimental modules. That's how idea and theory transform into real world application. Thank you very much, Mr. CY Koo and Mr. He.

Finally, I would like to give my special thank to my family. If not for the love, encouragement, support and patience, I would not be able to finish my study.

TABLE OF CONTENTS

CERTIFICATE OF ORIGINALITY	ii
ABSTRACT	iii
PUBLICATIONS	v
ACKNOWLEDGEMENTS	vi
TABLE OF CONTENTS	vii
LIST OF FIGURES	xi
LIST OF TABLES	xiv
LIST OF ABBREVIATIONS	xv
Chapter 1. Introduction	1
1.1. Background	1
1.2. Statement of problems.....	2
1.3. Objectives.....	5
Chapter 2. Literature Review	7
2.1. Radix Astragalus	7
2.1.1. Nature of Radix Astragalus	7
2.1.2. Polysaccharides in plant cells.....	9
2.1.3. Physicochemical properties & Applications of Polysaccharides	11
2.2. Membrane Separation Technology	13
2.2.1. Principal of membrane separation.....	13
2.2.2. Crossflow filtration modules	14
2.2.3. Ultrafiltration applied for Polysaccharides in TCM.....	18
2.2.4. Membrane fouling & mechanism.....	19
2.2.5. Current models for optimizing crossflow Ultrafiltration process	21
2.2.6. Techniques to prevent fouling and enhance performance.....	24
2.3. Key parameters in ultrasound enhanced filtration	25
2.3.1. Ultrasound fundamental	25
2.3.2. Ultrasonic transducer.....	28
2.3.3. Ultrasonic bubble collapse	30
2.3.4. Principal mechanisms of ultrasonic effects in Membrane Filtration.....	31
2.3.4.1. Acoustic Cavitations.....	32
2.3.4.2. Acoustic streaming	34
2.3.4.3. Microstreaming.....	35
2.3.4.4. Microstreamers	35
2.3.4.5. Micro-jet	36
Chapter 3. Methodologies & Experiments.....	38
3.1. <i>Radix Astragalus</i> Extracts	38

3.1.1. <i>Radix Astragalus</i> water extraction	38
3.1.2. Viscosity measurement of polysaccharides extracts	39
3.1.3. GPC	39
3.2. Membrane filtration module	40
3.2.1. PMMA crossflow cell	40
3.2.2. Stainless steel crossflow cell	41
3.2.3. Ultrasound transducer integrated CF module.....	42
3.2.4. US enhanced CF module vs. US integrated CF module	43
3.2.5. Membrane Characterization	44
3.3. Ultrasound transducers and intensity measurement.....	44
3.3.1. US transducer designed for enhanced CF module	44
3.3.2. US transducer designed for integrated CF module	46
3.3.3. Intensity measurement.....	46
3.3.4. Aluminium foil paper test for cavitation effect.....	47
3.4. RAE Ultrafiltration process.....	47
3.4.1. Ultrafiltration process control	47
3.4.2. Feed velocity & Reynolds number.....	49
3.4.3. Membrane cleaning process	50
3.5. Hydraulic model of filtration resistance.....	51
3.5.1. Resistance in series model in RAE filtration.....	51
3.5.2. Resistance in series model in US enhanced/integrated system	52
3.6. Modification of crossflow permeate spacer	53
3.6.1. US irradiation onto various materials.....	53
3.6.2. Stainless steel permeate spacers	53
Chapter 4. Ultrafiltration Fouling Profile of RAE	55
4.1. Characterization of US transducers.....	55
4.1.1. Intensity in water bath	55
4.1.2. Intensity in near zone region	56
4.1.3. Intensity inside the UF crossflow cell	57
4.1.3.1. Measured in crossflow cell in water bath.....	58
4.1.3.2. Measured in integrated crossflow cell	58
4.2. Characterization of Polysaccharides extract	59
4.2.1. RAE Viscosity property	59
4.2.2. GPC analysis on MW and MW distribution of polysaccharides.....	60
4.2.2.1. Original RAE.....	60
4.2.2.2. US irradiated RAE.....	62
4.3. Ultrafiltration Fouling profile of polysaccharides extracts	64
4.3.1. ANOVA analysis.....	64
4.3.2. Effect of feed velocity	66
4.3.3. Effect of TMP.....	69
4.3.4. Effect of MWCO	72

4.4. Chapter Summary.....	74
Chapter 5. Ultrasound enhanced crossflow Ultrafiltration of RAE.....	75
5.1. Effect of US frequency.....	75
5.2. Effect of US irradiation direction.....	76
5.3. Effect of MWCO on US enhancement.....	81
5.4. Effect of feed velocity on US enhancement.....	82
5.5. Membrane Morphology	83
5.6. Chapter Summary.....	84
Chapter 6. Ultrasound integrated crossflow Ultrafiltration of RAE	85
6.1. Effect of US operation modes	85
6.2. Effect of US output power and characterization of US transducer	87
6.3. Effect of feed spacer.....	90
6.4. Effect of pre-filtration of feed solution	91
6.5. External Ultrasonic Cleaning	93
6.6. Chapter Summary.....	94
Chapter 7. Effect of permeate spacer in US enhanced/integrated CF module.....	96
7.1. Test of effect of US irradiation on support materials in water bath.....	96
7.2. Effect of S.S. permeate spacer on US enhanced <i>RAE</i> Ultrafiltration.....	98
7.2.1. Effect of US irradiation on DI-H ₂ O flux without permeate spacer	98
7.2.2. Effect of permeate spacer on US enhanced RAE filtration.....	100
7.2.3. Effect of the porosity of S.S. permeate spacer on DI-H ₂ O flux compensation and permeate support resistance	103
7.2.4. Effect of the porosity of S.S. permeate spacer on flux enhancement in US enhanced CF filtration process	105
7.3. Effect of the porosity of S.S. permeate spacer on flux enhancement in US Integrated CF filtration process	107
7.4. Chapter Summary.....	110
Chapter 8. RSM & optimization of permeate spacer porosity in US integrated system	112
8.1. Experimental protocol.....	113
8.2. Analysis.....	115
8.3. Pareto chart.....	119
8.4. Response surface and contour plots of effects on responses.....	121
8.4.1. Response surface and contour plots of three variables on DI-H ₂ O compensation	121

8.4.2. Response surface and contour plots of three variables on permeate collection.....	123
8.5. Optimization: desirability function approach.....	125
8.6. Chapter Summary.....	131
Chapter 9. Conclusions & Recommendation for Future work.....	132
9.1. Conclusions	132
9.2. Recommendation for Future work	135
9.2.1. Specific energy consumption in US integrated CF module	135
9.2.2. Fabrication and optimization of a pilot scale US integrated module ...	137
References.....	140

LIST OF FIGURES

Figure 2-1	<i>Radix Astragalus</i> Plant and root	7
Figure 2-2	Chemical structure of monosaccharides in <i>Astragalus</i> extracts	9
Figure 2-3	Molecular weight distribution of polysaccharides extracted from RA.....	9
Figure 2-4	Plant cell wall structure	11
Figure 2-5	Crossflow filtration vs. Dead-end filtration.....	15
Figure 2-6	Crossflow filtration membrane test unit in patent US 4,846,970	17
Figure 2-7	GE Sepa™ CF II Med/High Foulant System	17
Figure 2-8	Sound energy reflection and transmission at interface of water and steel.....	28
Figure 2-9	Reproduced scheme of transducer: 1 protecting plate; 2 piezoelectric discs; 3 housing; 4 electrical current generator.....	29
Figure 2-10	Proposed mechanism for particle removal from membrane surface with ultrasound cleaning.....	32
Figure 2-11	Acoustic cavitation in a homogenous liquid medium	34
Figure 2-12	Liquid jet generates at liquid-solid interface	37
Figure 3-1	PMMA crossflow module	40
Figure 3-2	The scheme of Membrane Module 1.stainless steel support; 2.Feed/retentate channel and feed spacer; 3.Membrane; 4.Permeate channel and permeate spacer; 5.O-rings; 6.Permeate Openings; 7.Screws; 8.Feed/Retentate/Permeate outlet ports	41
Figure 3-3	Photo of ultrasound integrated crossflow module	42
Figure 3-4	US enhanced CF module vs. US integrated CF module.....	43
Figure 3-5	Distribution of transducer disk inside stainless steel housing	45
Figure 3-6	The schematic diagram of ultrasonic integrated crossflow UF system	49
Figure 3-7	Six stainless steel permeate spacer, the porosity of six spacers were 18.5%, 35.9%, 46.2%, 62.0%, 69.3% and 78.0%	54
Figure 4-1	Ultrasound intensities measured in water bath at central point and keep 30 mm away from transducer surface for both 28 kHz and 45 kHz.....	55
Figure 4-2	US intensity distribution profile along the central line in water bath and CF cell.....	56
Figure 4-3	28 kHz Ultrasound intensities measured in water bath at 3 cm and 1 mm away from transducer surface.....	57
Figure 4-4	Strong noise that distorting the wave in the near field zone.....	59
Figure 4-5	Effect of temperature and concentration on rheological properties of RAE	60

Figure 4-6	GPC results of five original samples	62
Figure 4-7	GPC chromatography: A: original RAE solution B: ultrasound irradiated RAE solution under 400W 60 min in glass beaker	63
Figure 4-8	Effect of flow velocity on permeation profile of RAE under constant TMP of 15 psi.....	67
Figure 4-9	Effect of feed velocity on fouling resistance under TMP of 15 psi. A: Total resistance as a function of total permeate collection; B: Reversible fouling resistance (R_{rf}) and irreversible fouling resistance (R_{if}) as a function of feed velocity	68
Figure 4-10	Effect of TMP on total permeate collection and steady-state flux at feed velocity of 0.2 m/s	70
Figure 4-11	Effect of TMP on fouling resistance at feed velocity of 0.2 m/s. A: Total resistance as a function of total permeate collection; B: Reversible fouling resistance (R_{rf}) and irreversible fouling resistance (R_{if}) as a function of TMP	71
Figure 4-12	Effect of TMP on total resistance at feed velocity of 0.8 m/s	72
Figure 4-13	Effect of membranes MWCO on flux decline rate at feed velocity of 0.3 m/s and TMP of 15 psi	73
Figure 4-14	Effect of membranes on three resistances (R_{if} , R_{rf} and R_m) at feed velocity of 0.2 m/s and TMP of 15 psi	74
Figure 5-1	Effect of ultrasonic frequency on permeation profile of RAE at feed velocity of 0.2 m/s, TMP of 15 psi and MWCO of 30 kDa	76
Figure 5-2	Permeate/TMP profile of UF process: without US irradiation versus US irradiation from either feed or permeate side of membrane	78
Figure 5-3	Effect of ultrasound irradiation direction on filtration enhancement factor at 15/0.2/30 kDa/200 W. a: ultrasound transducer; b: feed side of crossflow module; c: permeate side of crossflow module.....	79
Figure 5-4	Effect of ultrasound irradiation direction on three resistances (R_{if} , R_{rf} and R_m) at feed velocity of 0.2 m/s, TMP of 15 psi, MWCO of 30 kDa, frequency of 28 KHz and output power of 200 W.....	80
Figure 5-5	Effect of MWCO and feed velocity on ultrasound irradiation enhancement at 15/0.3/28KHz/200W. A: Effect of MWCO; B: Effect of feed velocity	82
Figure 5-6	Membrane SEM images. A. Fouled membrane generated by RAE Ultrafiltration at 15/0.2/30 kDa; B. treated membrane after 60 min US irradiation during RAE Ultrafiltration at 15/0.2/30 kDa/200W.....	84
Figure 6-1	Effect of irradiation mode on filtration profile of RAE at 200 W output power, TMP of 15 psi and feed velocity of 0.2 m/s	86
Figure 6-2	Effect of US output power on RAE filtration profile at TMP of 15 psi and feed velocity of 0.2 m/s.....	88
Figure 6-3	Effect of US power output on filtration enhancement factor	89

Figure 6-4	Effect of feed spacer on fouling resistance at TMP of 15 psi and feed velocity of 0.2 m/s	91
Figure 6-5	Effect of pre-filtration of RAE on total resistance	92
Figure 6-6	Effect of US on filtered and non-filtered RAE suspensions.....	93
Figure 6-7	SEM of the surface of membrane. A: RAE fouled membrane; B: after 10 min water flushing; C: after 10 min US irradiation under 400 W of output power; D: after 60 min US irradiation under 400 W of output power	94
Figure 7-1	Ultrasonic cavitation effect on aluminium paper with varied support under 200 W output power for 60 sec irradiation.....	97
Figure 7-2	DI-H ₂ O flux recorded in CF system under varied US irradiation	99
Figure 7-3	RAE filtration profile at TMP of 15 psi and Velocity of 0.2 m/s: A: Without permeate spacer; B: With S.S. permeate spacer of porosity of 18.5%.....	101
Figure 7-4	The effect of permeate spacer on US enhanced filtration, comparison of DI-H ₂ O flux, RAE steady state flux and after flushing DI-H ₂ O flux	103
Figure 7-5	DI-H ₂ O flux vs porosity of S.S. permeate support at various TMP	105
Figure 7-6	Effect of spacer porosity on US enhanced system	107
Figure 7-7	Effect of spacer porosity on US integrated system.....	109
Figure 7-8	Effect of spacer porosity on relative filtration enhancement factors in two systems.	110
Figure 8-1	Observed values compared to the predicted values given by the two response surface models	118
Figure 8-2	The linear, quadratic and cross-effects of each independent variable displayed in Pareto chart.....	120
Figure 8-3	Response surface and contour plots of three variables on DI-H ₂ O compensation	122
Figure 8-4	Response surface and contour plots of three variables on permeate collection	124
Figure 8-5	Desirability profile.....	129
Figure 8-6	Profiles for predicted values and desirability	130
Figure 9-1	Energy consumption in varied filtration processes	137
Figure 9-2	Multi-stage recirculation process	139

LIST OF TABLES

Table 2-1	Tonify TCM summarized from Chinese Herbal Medicine Materia Medica 3rd version [1]	12
Table 2-2	Five distinct periods of physical phenomena during flux decline in Microfiltration	20
Table 2-3	Acoustic impedances and reflection coefficients of common used materials.....	27
Table 3-1	Calculated near zone region for all three ultrasonic transducers used in experiments.....	46
Table 3-2	Reynolds number corresponding to feed flow rate and velocity	50
Table 4-1	The experimental set values for three independent variables.....	65
Table 4-2	Fractional factorial design and experimental outcomes of total permeate collection.....	65
Table 4-3	Regression statistics and analysis of variance (ANOVA) for total permeate collection.....	65
Table 7-1	The resistance generated by the S.S permeate support as the function of support porosity	104
Table 8-1	Box-Behnken design (BBD) for modified S.S. permeate spacer in US integrated filtration system	114
Table 8-2	Regression equation coefficients for responses and model validation	116
Table 8-3	Analysis of variance (ANOVA) of the modelled responses.....	117
Table 8-4	Desirability value and predicted responses	129
Table 8-5	Developed optimization condition and overall desirability.....	131

LIST OF ABBREVIATIONS

ANOVA	Analysis of Variance
BBD	Box-Behnken design
CF	Crossflow
DI-H ₂ O	Deionized water
GPC	Gel permeation chromatograph
MF	Microfiltration
MWCO	Molecular weight cut off
PES	Polyethersulfone
NF	Nanofiltration
PMMA	Polymethyl methacrylate
PP	Polypropylene
RAE	<i>Radix Astragalus</i> extracts
<i>Re</i>	Reynolds number
RO	Reverse Osmosis
RSM	Response Surface Methodology
S.S.	Stainless steel
TCM	Traditional Chinese medicine
TMP	Transmembrane pressure
UF	Ultrafiltration
US	Ultrasound

Chapter 1. Introduction

1.1. Background

With a history of more than 3000 years, Traditional Chinese Medicine (TCM) has built up strong reputation in diagnosing and curing diseases [1]. Recently, many international pharmaceutical companies are using TCMs as resource to discover and study natural bioactive compounds [2]. In general, investigations of bioactive components in TCM involve pulverization, slicing, bleaching, soaking, extraction, separation and purification followed by *in vitro* or *in vivo* pharmacological screening and analysis. Regarding the separation process, membrane separation has been recognized as a well-developed technique for the concentration and separation of different components from mixtures with regard to its diversity in materials and structures [3]. Despite of the state-of-art design of membrane filtration system, membrane fouling is inevitably inherent to all separation processes. Fouling results in severe flux decline, a drop in operational efficiency and boost up the energy consumption. Eventually, it would not only reduce the productivity of the separation process but also alter the separation characteristics of applied membranes. Membrane fouling is essentially a combined result of absorption and deposition of feed material onto the membrane surface and into the pores. The adsorption of solute particles on the membrane surface is governed by interactions between solutes and membrane material; while pore plugging is mainly governed by the size of particle and membrane pore size as well as operating conditions such as transmembrane pressure, shear rate and temperature [4]. In a particular membrane filtration process, fouling could be attributed to different mechanisms dominated by feed solution properties and operational conditions. In terms of the Ultrafiltration (UF) process of

polysaccharides extracted from herbal extracts, the nature of polysaccharides, the diversity of molecular weight (MW) and MW distribution as well as the complication of the polysaccharide molecular structures could inevitably trigger higher tendency to foul the membranes than other processed solutions. It is well accepted that the primary target in optimization of membrane separation process is to achieve maximum permeate flow of desired product with minimum energy cost, namely, high permeability as well as high productivity.

Numerous technologies have been developed to overcome the fouling limitations with hydrodynamic approaches aiming at increasing the shear rate and flow instability inside the filtration modules. These approaches include introducing secondary flow and pulsed flow, inserting spacers and high shear rate device, and applying vibrations, external electronic field and ultrasonic irradiation [5]. Ultrasonic irradiation is proved to be an effective approach employed in membrane filtration process. A simple, fast, cost-effective crossflow filtration system for the application of TCM isolation and purification is most desirable for both industrial engineers and academic researchers. This project crosses field boundaries with work being carried out in chemistry, physics, industrial centre and the collaboration with equipment companies. The novel ultrasound (US) integrated crossflow (CF) filtration technique would make significant contributions in TCM, food technology and biotechnology where filtration is an essential step.

1.2. Statement of problems

Under the irradiation of ultrasound, the filtration process can be operated more efficiently and for prolong periods without frequent cleaning. Possible mechanisms involved in ultrasonic membrane cleaning include the formation, growth and collapse

of microbubbles in the liquid. Associated with acoustic cavitations, mechanical agitation and increased shear forces may be responsible for keeping the particles away from membrane surface as well as inside the pores [6]. Thus the construction of a looser, more porous fouling cake layer resulted in reduced concentration polarization and pore blockage [7]. Moreover, another two specific effects should be considered. Acoustic streaming can initiate the agglomeration process of those fine particles. Sufficient vibration energy generated by the system can keep the particles partly suspended and thus create more free channels for solvent transportation. Even though ultrasonic energy has been widely used in a variety of industrial engineering processes such as extraction, cleaning, emulsification and degassing, there is still a lack of in-depth investigation on the mechanisms of ultrasonic induced membrane filtration. The US induced effects on membrane filtration are dependent on a number of factors including the orientation and position of the ultrasonic transducer, ultrasonic power intensity and frequency, filtration module, operating pressure, and nature of processed solution as well as membrane configurations [8]. The dramatic loss of sonic power occurred during the propagation along housing material hindered this particular technique to be well adapted into existing filtration modules. As of today, in terms of crossflow UF and microfiltration processes with assistance of ultrasonic radiation, all experimental approaches are still limited as immersing the commercialized filtration modules into ultrasonic bath to enable effective radiation [9-12,13]. Particularly in most of Muthukumaran [11,12,14] group's work, they adapted Millipore Minitan membrane unit as filtration module. The standard unit composed of stainless steel holders of thickness 1.1 cm and acrylic manifolds of thickness 2.3 cm, within membrane was placed. The whole setup dramatically decreased the ultrasonic irradiation efficiency. Several key technical factors

including ultrasound fundamental theory, module design in ultrasound assisted membrane filtration and the effects of varied operation parameters on filtration behaviour and membrane morphology have been reviewed [15,16]. Not only is the membrane erosion due to ultrasonic irradiation undesirable for the commercialization of this technique but also the difficulties of integrating transducer into membrane modules has hindered the scale up of this art.

Conventional crossflow modules normally build up in closed and compact system with accurately designed channel dimension to ensure sufficient flow velocity, thus the spare space available for embedding transducers is very limited. An ultrasonic bath has limitations because the acoustic intensity declines significantly by propagation through the membrane housing materials. Alternative approach was applied to immobilize a piezoelectric disk into the housing of a commercial Osmotic crossflow cell sealing with Styrofoam and silicone [17]. Despite the interruption and complexity caused by the sealants, the cleaning process had to be operated under lower output power of 45.2 W preferably with fouled PVDF membranes to avoid the damage to membrane surface. Filtermat Oy [18], a company in Finland, modified ceramic crossflow filter tubes by rotating them against the ultrasonic transducer with back flushing. Up to days, the pilot scale and industrial units still limit at microfiltration process with high concentration of suspended particles. Carmen [19] patented a filtration apparatus with ultrasonic generator mounted onto tubular membrane module through permeate chamber. Sufficient sound power has to produced to pass through the permeate frame and medium to induce cavitations effect. A recent invention [20] utilized ultrasound energy for fouled filtration membrane cleaning. The claim discovered all possible membrane configurations including tubular, flat sheet, hollow fibre and spiral wound can be fixed with

ultrasonic transducers. Other than that, a compact and portable filtration system comprising a plurality of filter units sets assembled with one or more ultrasound transducer has been patented in 2007 [21]. The claims are promising in terms of the potential application on manufacturing line. However, as today there is still no practical application has been done to validating those research findings. To address these limitations, a simple and effective approach to integrate ultrasound transducer into customized crossflow filtration system was developed in our study. The work was motivated by the increasing attention in introducing both membrane and ultrasonic technologies for separation and purification of natural product extracts.

1.3. Objectives

The goal of this research is to fill the gap in current available ultrasonic assisted membrane filtration applications by developing a novel crossflow filtration module integrated with ultrasound transducer for enhanced filtration efficiency. Specifically, the project is aimed at applying transformed filtration system for the separation and purification of TCM. Upon a comprehensive discussion of ultrasound theories and applications, the aim should be accomplished with the following objectives: Customize a versatile crossflow filtration module to be adapted in ultrasonic bath; Design and build a laboratory scale crossflow filtration unit integrated with ultrasound transducers; Perform the membrane Ultrafiltration with *Radix Astragalus* extracts to investigate the fouling behaviour of particular solute under controlled experimental conditions; Apply ultrasonic irradiation effect to Ultrafiltration process and evaluate the effect of ultrasonic irradiation on membrane fouling resistance. Upon the completion the pioneer work, the modification of permeates spacer in the CF module will be carried out. Moreover, response surface

methodology will be applied and a mathematical model will be established to predict the performance of this dynamic filtration process and optimize the operational factors.

Chapter 2. Literature Review

2.1. Radix Astragalus

2.1.1. Nature of Radix Astragalus

Radix Astragalus (Huang Qi), derived from the Chinese herb *Astragalus membranaceus* (Fisch.), is one of the most popular components prescribed by traditional Chinese medicinal practitioners. *Astragalus membranaceus* (Latin): membranous milk-vetch root (English), huang qi (Chinese), ogi (Japanese), and hwanggi (Korean) favourite mostly pine forests and sandy soils and are cultivated widely in china, Siberia and northern Korea. The major active components in *Astragalus* root contain polysaccharides, saponins, flavonoids, proteins and divalent and monovalent cation as well as trace elements of europium, tantalum, hafnium and thorium [22]. Good quality of *Astragalus* root are long, thick and unbranched without blackish or hollow central core, rather soft texture and fresh yellow centre as shown in Figure 2-1.



Figure 2-1 *Radix Astragalus* Plant and root

The chemical composition of bioactive components in *Astragalus* has been systematically studied. A multi-component total analytical method [23] was applied to compare the fingerprint chromatograms and purified sixty-six active components from *Astragalus* extracts. A reliable HPLC-DAD-ELSD method was developed to qualitatively and quantitatively detect twelve major flavonoids and five saponins extracted from different part of *Astragalus* [22]. With stepwise ethanol precipitation method, Polysaccharides found in *Astragalus* have been classified as polysaccharides (PS)-A, -B, -C, and -D by the method of stepwise ethanol precipitation. PS-A is identified as α -(1, 4) and α -(1, 6) glucan in a ratio of 5:2; PS-B and PS-C are classified as α -(1,4) glucans; PS-D is a heteropolysaccharide composed of glucose, arabinose and rhamnose in a 9:3:2 ratio. Guan's [24] group developed a new saccharide mapping technique to differentiate unknown polysaccharides in *Astragalus* based on their enzymatic hydrolysis properties and identified the monosaccharide units by HPLC-DAD-MS. They discovered that glucose, galactose, rhamnose, mannose, maltose, and disaccharides of hexose compose the units of backbone and branch of PS by glycosidic linkages. Figure 2-2 demonstrated some chemical structures of monosaccharides determined in this study. Moreover, the molecular weights of two polysaccharides fractions purified from *Radix* water extract were 1699 kDa and 1197 kDa analyzed by HPLC-GPC [25]. On the other hand, by applying membrane Ultrafiltration technique, the molecular weight distribution of polysaccharides in RAE was found having wide distribution ranging from 3 kDa up to over 150 kDa as shown in Figure 2-3 [26]. Two major groups of molecular weight dominate the constitution of total polysaccharides extracted from RA, one take inhabit 38.9% with MW smaller than 3 kDa and the other one inhabit 43.4% with MW larger than 150 kDa.

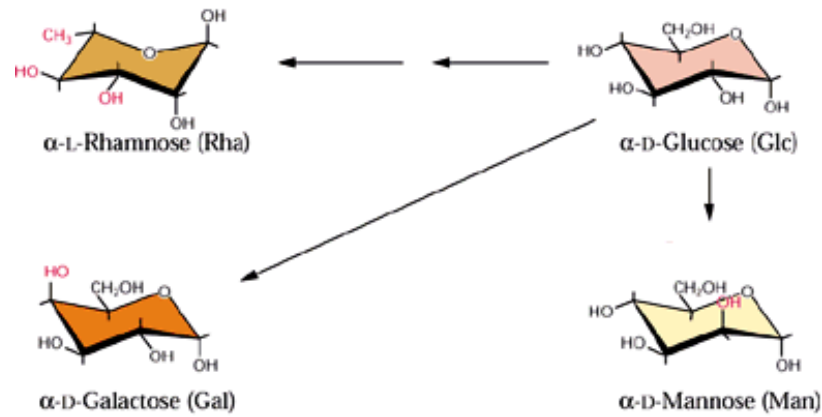


Figure 2-2 Chemical structure of monosaccharides in *Astragalus* extracts

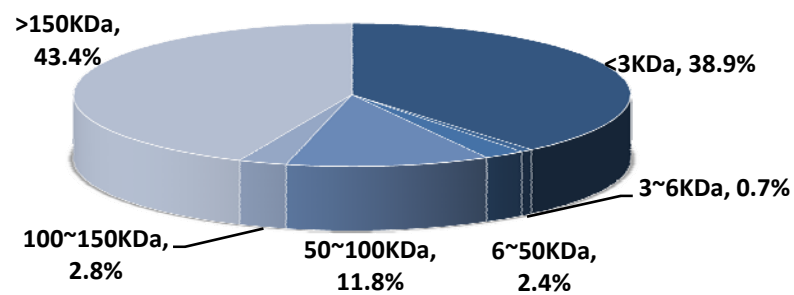


Figure 2-3 Molecular weight distribution of polysaccharides extracted from RA

2.1.2. Polysaccharides in plant cells

According to the production routes, there are three categories for polysaccharides, namely, nature biopolymers, synthesized polysaccharides from carbohydrates and isolation from fermentation processes. Although polysaccharides are active components subjected to the cell walls and physiological liquids of living features, those extracted from plants bring up new insights into the market due to renewable resources and multifunction [27]. Polysaccharides appear in varied configurations from varied locations in varied plants. The major polysaccharides in

the primary and secondary walls include cellulose, hemicellulose and pectin in different proportions. Plant cells are protected by a rigid fibrous component known as cellulose. Aside from being the primary building material for plants, cellulose can be used to make paper, film, explosives, and plastics, as well as many other industrial applications. Comparing to the primary cell wall, the much thicker and stronger secondary wall donates the most carbohydrates in biomass [27,28]. It is well accepted that hemicelluloses can be defined in four classes differing in side-chain types, distribution, localization and the type of glycoside linkages in the macromolecular backbone: xyloglucans, mannans, β -glucans and xylans which represent the main hemicellulose components extractable from secondary cell wall of plants [29]. In contrast to celluloses that are crystalline, strong, and resistant to hydrolysis, hemicelluloses consisting 500~3000 sugar unit have more random, amorphous structure with little strength. Three classes of pectin polysaccharides have been characterized: homogalacturonans, rhamnogalacturonans, and substituted galacturonans [29]. The applications of pectin are mainly adopted in the production of jelly, jam, marmalade, and other confections. Pectin is composed of an acidic polysaccharide and several types of neutral sugars [30]. A visualized scheme is illustrated in Figure 2-4 [31], the celluloses (blue) and hemicelluloses (yellow) are covalently crosslinked to organize a cellulose- hemicellulose network, which is embedded in the branched pectin's matrix (purple).

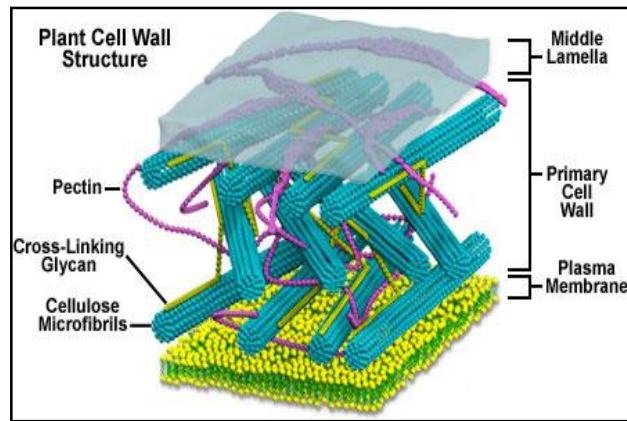


Figure 2-4 Plant cell wall structure

2.1.3. Physicochemical properties & Applications of Polysaccharides

Traditional Chinese medicine defines health as body integrity, adaptability, continuity, and balance with the doctor prescribing traditional plant, animal, and mineral remedies to sustain a self-regulatory status in the body (a balance of yin and yang)” [32]. Studies on pharmacology and clinical practice confirmed the unique biological functions of *Radix Astragalus* extracts. *Radix Astragalus* offers stronger tonifying effect to spleen and lung qi and improving the fluid metabolism by raising the yang qi to muscle layer and exterior body. The key characteristics of *Astragalus* are also involved stopping sweating, facilitating urination, accelerating the recovery of inflammation sites and generating redevelopment of fresh [1]. *Astragalus* is used for treating the common cold and upper respiratory infections; to strengthen and regulate the immune system; and to increase the production of blood cells particularly for those with chronic degenerative diseases such as cancer [33]. It is also used orally for chronic nephritis, diabetes as well as an antibacterial and antiviral agent. The therapeutic effect of this herb strongly depends on the preparation forms and the synergized other components in the formula.

In preclinical studies, saponin astragaloside IV was found to be able to increase the fibrinolytic potential of cultured human endothelial cells in vitro [34]. The presence of aminobutyric acid in *Astragalus* extraction exhibits hypotensive activity [35]. The root extract could remarkably stimulate the proliferation of murine spleen cells of mice [36]. A flavonoid fraction from the leaf and stem increased cell-mediated immunological response in mice [37].

In particular, polysaccharides extracted from TCM have been extensively investigated due to their distinguished therapeutic properties and low toxicity. Chang [38] reviewed the bioactivities of polysaccharides in Chinese herbs which are characterized as tonic in nature. Tonifying herbs can strength the physiological process of the body and provide extensive defences against disease. Tonics can be used in treating patterns of deficiency in the following four aspects, namely Qi, blood, Yin and Yang [1]. Most herbs that tonifying the Qi, blood and Yin are sweet and cold yet those tonifying the Yang are generally bitter and warm. Some representative herbs containing at least one of major known constituents, such as monosaccharides, oligosaccharides and polysaccharides classified as sweet taste tonic are outlined in Table 2-1.

Table 2-1 Tonify TCM summarized from Chinese Herbal Medicine Materia Medica 3rd version [1]

Tonify Qi	Tonify Blood	Tonify Yin
<i>Ginseng Radix</i> (Ren shen)	<i>Rehamiae Radix Preparata</i> (Di Huang)	<i>Glehniae Radix</i> (Sha Shen)
<i>Astragali Radix</i> (Huang Qi)	<i>Angelicae Sinensis Radix</i> (Dang Gui)	<i>Panacis Quinquefolii Radix</i> (Xi Yang Shen)
<i>Godonopsis Radix</i> (Dan Shen)	<i>Longan Arillus</i> (Long Yan)	<i>Asparagi Radix</i> (Tian Men Dong)
<i>Pseudostellariae Radix</i> (Tai Zi Shen)		<i>Polygonati Odorati Rhizoma</i> (Yu Zhu)
<i>Jujubae Frutis</i> (Da Zao)		<i>Sesami Semen Nigrum</i> (Hei Zi Ma)

The diversity of molecular weight, conformation and compositions of polysaccharides as well as the position isolated from plants determine the bioactivities of polysaccharides. For example, the various physiological effects of xylan-rich extracts have been reviewed including antimutagenic, antioxidant, anticomplementary and anti-HIV activities [29]. Many traditional Chinese medicines can be combined with western medicine to enhance the cancer therapy. The important immunomodulatory property of polysaccharides is mainly attributed by a β 1-3, 1-4 or 1-6 branch chains configurations. These configurations can increase the level of immune response resulting in a binding of specific antibody. Moreover, it is cited that those polysaccharides with anionic structures and higher molecular weight seem to be more stimulatory [31]. *Astragalus* polysaccharides particularly PS-D has drawn a great deal of attention due to its immunomodulatory functions. Tomoda et al. [39] reported that a polysaccharide with MW of 60 kDa extracted from *Astragalus* root improved immunopotentiating activity in the carbon clearance test. Kajimura et al. [40] isolated two active polysaccharides fractions with MW of 120 kDa and 220 kDa and confirmed the productivity level of IgG increased significantly in mice with the treatment of the two fractions.

2.2. Membrane Separation Technology

2.2.1. Principal of membrane separation

“Membrane” refers more than one single item, but a large variety of structures and materials with specific properties. During the past couple of decades, membrane technology has been recognized as a sophisticated solution for a wide variety of separations in industries. Membrane technology fits in various chemical technology disciplines including material science, chemistry, chemical engineering and process

control. By definition, membrane is a barrier to separate two components. There are wide varieties of membranes that differ in chemical/physical properties and structures. In terms of the origin of membrane, there are natural membranes and synthesized membranes which including polymeric, ceramic, metal and liquid membranes. In terms of the structure of synthesized membrane, there are symmetrical membranes covering both porous and dense type. In contrast to uniformly distributed structural membranes, anisotropic membranes having thin effective separation layer supported by porous structure benefit almost all commercial processes with higher transport rate. The most developed pressure-driven membrane separation processes in industry are Microfiltration (MF), Ultrafiltration (UF), Nanofiltration (NF) and Reverse Osmosis (RO), where the first two process share the pore-flow mechanism and RO follows exactly dense solution-diffusion separation. NF membrane with average pore size in the range of $5\text{\AA}\sim 10\text{\AA}$ exhibits the intermediate transport behaviour between pore-flow and solution-diffusion. NF is a low pressure RO technology and has been successfully used for the water softening to remove hard, colour and high organic contents in feed water [4]. It is straightforward to distinguish between various processes with regard to membrane structure. In the case of Ultrafiltration, membrane usually has an asymmetric structure with a thin, dense top layer (thickness $0.1\sim 1.0\ \mu\text{m}$, pore size $10\sim 1000\ \text{\AA}$) supporting by a porous layer. The dense top layer performs the separation while the porous substrate provides mechanical strength. Therefore, the hydraulic resistance to mass transfer is almost completely determined by top layer.

2.2.2. Crossflow filtration modules

In a crossflow membrane filtration system, the transportation of particle is governed by two major actions: negative direction which moving the particles toward the membrane surface and positive direction involving shifting them away from the membrane surface. The negative forces include van der Waals attraction (F_A), gravity (F_G) and permeation drag (F_d), while the positive forces depend on electrical double layer repulsion (F_R), Brownian diffusion (F_B), shear-induced diffusion (F_S) and lateral inertial lift (F_l). The momentum situation of a particular particle is dominated by the sum of all imposed forces in a flow channel.

$$F = \frac{\pi}{6} d_p^3 \rho_p \frac{dv_p}{dt} = (F_R + F_B + F_S + F_l) - (F_A + F_G + F_d) \quad (2-1)$$

where d_p is the particle diameter, ρ_p is the density of particle and v_p is the particle transport velocity.

Membrane processes are characterized as the motion that the feed stream is divided into the retentate stream and the permeate stream. Ultrafiltration processes generally performed at pressure below 100 psi.

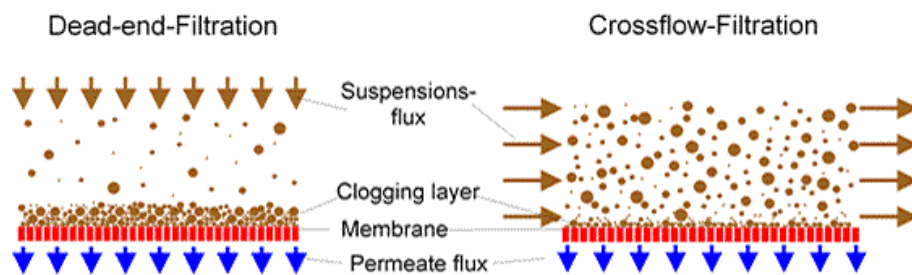


Figure 2-5 Crossflow filtration vs. Dead-end filtration

In large-scale industrial membrane filtration, crossflow (tangential-flow filtration) is commonly employed over dead-end filtration (shown in Figure 2-5).

Comparing to dead end filtration, in crossflow filtration, the fluid stream runs in tangential direction to membrane surface, initiating a pressure difference across the membrane. The movement of the feed solution across the membrane surface can prevent the buildup of foulants on the surface gradually. Driven by pressure, the solvent part and smaller size solute of the filtrate can pass unhindered through the membrane while residual components are re-circulated back to feed. In this system, the feed solution can be easily maintained at constant composition, and the turbulence at the membrane surface generated by flow hydrodynamic characteristics can be manipulated to minimize the fouling.

The first patent described the cross-flow filtration membrane test unit was issued in 1989 [41], and the typical design of a unit has been defined as two cell bodies, a pair of O-rings, a feed spacer cavity and a permeate carrier cavity. As displayed in Figure 2-6, the patent claimed that the unique design unit can be used to characterize the performance of all types of membranes and alternatively the feed spacer (No. 20 part) can be manipulated to restrict the flow to be either laminar or turbulent motion. Upon the commercialization of this technique, GE Sepa™ CF II Med/High foulant system (Figure 2-7) manufactured by GE Osmonics had benefited numbers of research groups in terms of membranes studies, protein separation and purification, food technologies as well as other chemical processing.

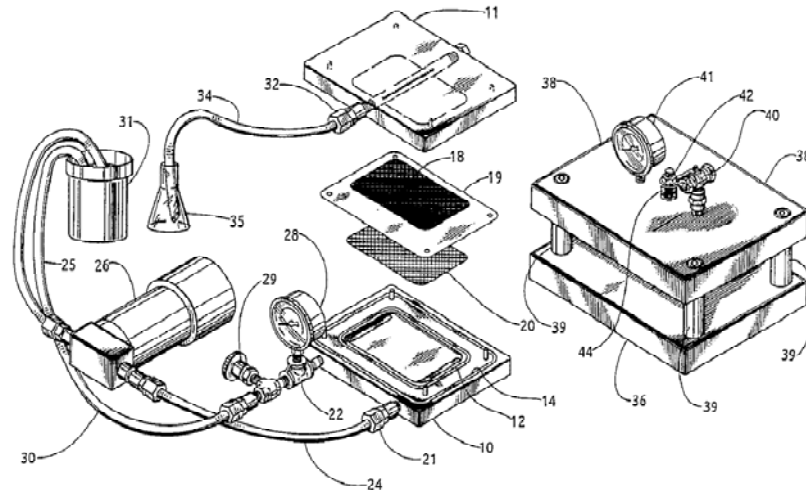


Figure 2-6 Crossflow filtration membrane test unit in patent US 4,846,970



Figure 2-7 GE Sepa™ CF II Med/High Foulant System

Apart from other components in a membrane filtration module, feed spacer has been systematically studied in crossflow filtration and spiral wound membranes [42-52]. The pioneer idea claimed in patent US 6,989,097 [52] described how the unique design of cross-section shape of the spacer strands can promote the fluid dynamics as well as constrain a feed channel between adjacent membranes. Computational fluid dynamics technique was applied in the patent to estimate the pressure drop

across the membrane module and the velocity profiles comparing the novel design with prior art.

2.2.3. Ultrafiltration applied for Polysaccharides in TCM

Ultrafiltration is traditionally adopted to retain macromolecules and colloids from a solution. Remarkable growing interests in the research of TCM have broadened up the market of membrane filtration applied in food and biotechnology industries. Ultrafiltration employs a finely porous membrane with average pore diameter of 10 to 1000Å to separate water and microsolute from macromolecules and colloids. There are no strict lines to distinguish between Ultrafiltration and other membrane separation processes such as microfiltration and reverse osmosis when only pore size is concerned. The pore size /pore size distribution of membrane required for the separation is determined by the particle size and chemical properties of the solute. The MW range and distribution of polysaccharides in TCM enable Ultrafiltration the desired separation process in both laboratory and industrial scale. Comparing to MF, UF membrane favours asymmetric structure with a denser surface layer which eventually generate higher hydrodynamic resistance [53]. The crude polysaccharides solution with broad molecular weight distribution from 6 kDa to 2300 kDa extracted from *Urtica fissa* [54] was subjected to MWCO of 5 kDa hollow fibre membrane filtration to concentrate. The active components were capable of directly inhibiting cell proliferation of HeLa cells in BPH (Benign Prostate hyperplasia) treatment. Buranov et. al [55] purified polymeric Hemicellulose in wheat and corn bran using MWCO of 30 kDa PES membrane. Similar technique was applied to purify crude polysaccharides extracted from *codonopsis Radix* (Dangshen) and the immunological activity of increasing lymphocytes proliferation in vitro was

confirmed [56]. Another group [57] applied 30 kDa spiral wound PES membrane to purify two groups of polysaccharides (MW 45 kDa and 128 kDa) from *E. Angustifolia Radix* extracts. It validated that higher MW polysaccharides subjected to enzymatic degradation. The structure and bioactivity of pectin isolated from *Prunus dulcis* (almond) [58] was studied to exhibit stronger lymphocyte stimulatory effects in both in vivo and in vitro experiments. Upon above applications, membrane material, MWCO and membrane module configurations should be taken into account according to the nature of extracted polysaccharides.

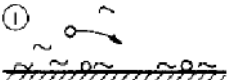
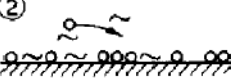
2.2.4. Membrane fouling & mechanism

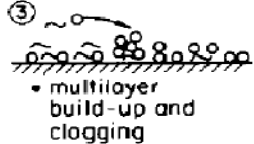
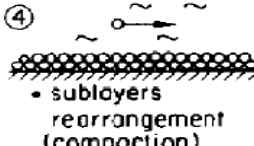
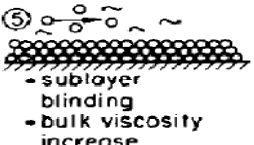
Due to the complex nature, TCM has a high tendency to foul the membranes during filtration process. Particularly, an exaggerated fouling situation would be encountered in the case of polysaccharides as solute since there are stronger aggregation tendency contributed by the glycosyl side chains [29]. In general, fouling are the adsorption and deposition of material present in the feed solution on the membrane leading to loss of efficiency of the separation process. Fouling will result in severe flux decline, a drop in operational efficiency and increase the energy consumption. Fouling reduce not only the productivity of the process but also changes the separation characteristics of the membrane. There are four major categories of parameters which can affect the membrane fouling: Physicochemical properties of the solute, molecular weight, hydrophobicity, electrostatic charge, shape; physicochemical parameters of the feed solution, e.g. solute concentration, pH, salt concentration; Physicochemical properties of the membrane, e.g. hydrophobicity, electrostatic charge, reactive groups; Membrane morphology, i.e. pore size, pore shape, straight pores vs. pore network; The operating parameters, e.g.

TMP, permeate flux, system hydrodynamics. Membrane fouling is mainly a combined result of absorption and deposition of feed material onto the membrane surface and within the pores.

The adsorption of solute particles on the membrane surface is governed by chemical interaction between solutes and membrane material; while the pore plugging is mainly governed by the size of particle and membrane pore size as well as operating condition such as transmembrane pressure, shear rate and temperature [4]. Concentration polarization brings out reversible fouling and membrane permeability is recoverable after certain cleaning process. In contrast, particle adsorption to membrane surface and inside the pores increase the filtration resistance and steer a permanent lose of membrane permeability [59]. In a particular membrane filtration, fouling could be attributed with different mechanisms due to the feed properties and operational conditions. Usually, in the initial stages, membrane fouling could be dominated by pore construction and pore blocking. Once the foulants have accumulated on the membrane surface to form cake layer, cake formation and concentration polarization become the leading mechanism. Especially, five distinct periods of physical phenomena during flux decline have been extracted from the experimental literatures (shown in Table 2-2) [60].

Table 2-2 Five distinct periods of physical phenomena during flux decline in Microfiltration

<p>①</p>  <ul style="list-style-type: none"> • sorption of dissolved solutes internally • initial deposit 	<p>At initial stage, as soon as the membrane is exposed to the macromolecules in solution, the kinetics of macromolecule absorption into the pore will be fast and strong binding capacity.</p>
<p>②</p>  <ul style="list-style-type: none"> • sublayer deposit (below monolayer) 	<p>Suspended particles begin to deposit onto membrane surface to build up the first sublayer and the permeate flux will not be decreased until the whole monolayer forms.</p>

 <p>③ • multilayer build-up and clogging</p>	<p>As multisublayers building up on the membrane, the two forces, migration of solids towards the membrane and back-migration to the bulk, competes resulting in a relatively constant permeation flux.</p>
 <p>④ • sublayers rearrangement (compaction)</p>	<p>As the sublayers grow and become densified, the flux decline rate decreased since mass transfer coefficient for permeate flow is mainly dominated by particle rearrangement.</p>
 <p>⑤ • sublayer blinding • bulk viscosity increase</p>	<p>A rapid drop in permeation velocity is observed when the concentration in bulk solution increased.</p>

Membrane fouling consequent from combining overall effects of the properties of feed solution, nature of membrane material, membrane module design and operating conditions. In terms of the UF process of polysaccharides in herbal extracts, the nature of polysaccharides, the diversity of molecular weight distribution as well as complicity of polysaccharides structures could affect the performance of the separation process.

2.2.5. Current models for optimizing crossflow Ultrafiltration process

Numerous models have been developed to predict the permeate flux as a function of operating parameters, membrane properties and feed properties in UF to identify the relations between operation and performance. Commonly used models for modelling the flux through the membrane as the function of transmembrane pressure include following [61]:

Pore flow model

$$J_v = \frac{\epsilon_m d_p^2 \Delta P}{32 \mu l_p} \quad (2-2)$$

Resistance model

$$J_v = \frac{\Delta P}{R_m} \quad (2-3)$$

Osmotic pressure model

$$J_v = \frac{\Delta P - \Delta \pi}{R_m + R_{cp}} \quad (2-4)$$

where ε_m is the membrane porosity; d_p the average pore diameter; μ the fluid viscosity; l_p the average pore length; J_v the membrane flux; ΔP the transmembrane pressure difference; $\Delta \pi$ the osmotic pressure difference; R_{cp} the gel layer resistance; and R_m is the membrane resistance. Pore flow model predicts the permeate flux in the pressure control region based on Hagen-Poiseuille's law when assuming that the membrane has identical cylindrical pore structure which uniformly distributed on the membrane surface and the solute concentration should be adequate low to be neglected. At most Ultrafiltration processes, the total membrane hydraulic resistance can be used to calculate permeate flux with resistance model. Both pore flow model and resistance model are developed based on the argument that a linear relationship exists between the membrane flux and transmembrane pressure under relatively low pressure. In the case that the concentration of solute at membrane surface is significantly higher than that in the bulk solution, the osmotic pressure at the membrane surface is no longer negligible. Osmotic pressure model can be applied to describe the permeate flux. As the transmembrane pressure increases, the permeate flux will be increasing at early stage. With the building up of solute concentration near membrane surface, the increase of osmotic pressure could compensate the positive effect of transmembrane pressure. As a result, during filtration of

concentrated solution at high TMP, permeate flux may not show a linear correlation with increase in transmembrane pressure. And the dependency of the permeate flux on TMP decreased gradually with the increasing of applied TMP [62].

The investigation of various parameters on flux decline and membrane fouling mechanisms has been extensively carried out to provide practical guidance in process design and operations. When it comes to individual filtration process, theoretical and experimental customization upon this description should be done based on the operational parameters. Zhang & Song [63,64] claimed that the permeate flux of uniform spherical silica colloids (26,50 nm in diameter) in crossflow filtration (20 nm in pore size) declined with time as cake layer growing till the steady states. With the evaluations of varied TMP, shear rate, particle size and feed concentration, steady state flux was discovered to be independent of TMP as the increasing of cake layer thickness comprised the increasing of pressure. In contrast, shear rate benefited the increase of steady flux as well as shorting the time achieving the steady state. In food industry, typical membrane bioreactor suffered dramatic flux decline due to the contents of microbial cells and extracellular polymeric substances (EPS) in suspended solids, whereas, the purification of polysaccharides in TCM would face the same challenge. Nataraj et al. [65] quantified the correlation between the properties of model polysaccharides xanthan (3 MD), actigum CS11 (0.5 MD) and glucan, and membrane fouling (10 kDa, 30 kDa) which was classified as standard pore blocking, complete pore blocking and cake buildup. They claimed that the membrane pore size made great impact on the respective fouling behaviour, the permeate flux couldn't reach at a steady state for all polysaccharides suspensions with 30KDa membrane. The resistance in series model indicated that the fouling of membrane with smaller pore size predominantly governed with so called "external fouling" where the cake

layer built up. On the other hand, the internal fouling (pore plugging/pore narrowing) underwent with larger pore size membrane filtration. The above studies conducted membrane fouling only with model solutions, however, the real suspensions extracted from herbal products are far more complex and polydisperse. In order to address this issue, Baruah and Belfort [66] pioneered the Aggregate Transport Model, a global model to predict the performance of general UF process incorporating both monodisperse and polydisperse suspensions. The generality of this model was further validated by real case studies in which pH, ionic strength, solutes polydispersity, membrane pore size distribution, MWCO and operating conditions were all merged into algorithm developed with computational protocols. Despite all the advances this model could offer, proper customization must be applied to individual UF process in terms of varied membrane chemistry, channel geometries and flow dynamics.

2.2.6. Techniques to prevent fouling and enhance performance

Numerous technologies have been developed in alleviating the limitations of Ultrafiltration processes caused by membrane fouling. Approaches adapted in industries to control concentration polarization and fouling include chemical, hydrodynamic, and physical methods [5]. Regarding the pre-treatment of feed solutions, prefiltration with larger pore size filter would be able to remove those impurities, bacterial and virus. Surface modifications including manipulating negatively charged membrane and increasing the hydrophilicity as well as tailoring chemistry properties of the membrane can favour a less fouling filtration process. Polyethersulfone (PES) membrane is the most popular choice for polysaccharides Ultrafiltration due to easy manufacture, cheap capital cost, and sustainable chemical

and mechanical stability. When the hydrodynamic parameters are concerned, the introductions of secondary flow, pulsed flow, vibrating and rotating membrane are implementing into practical filtration process. The concept of vibratory shear-enhanced process has been adopted by Aeronfilter® [67] to create anti-fouling membrane system. External electronic field and Ultrasonic irradiation are extensively discovered to improve the filtration efficiency and cleaning efficiency. Many strategies aiming at enhanced membrane filtration performance involve extra energy input and additional facilities. Therefore, the requirement of distinguishing the trade-off between productivity and capital cost urges expertise to come across more optimized system design.

2.3. Key parameters in ultrasound enhanced filtration

2.3.1. Ultrasound fundamental

Ultrasound is cyclic sound wave with a frequency beyond the upper limit of human hearing. Sound waves are vibrations or oscillations of particles of gases, solids or liquids where the wave travelling through. In general, there are four types of waves based on the mode of particles vibration with respect to the direction of the propagation of the waves, namely, longitude, shear, surface and plate waves [68]. Longitudinal wave that causes compression and rarefaction of the molecules in the medium is widely used as this type of wave can propagate in any medium and have greater velocity comparing to other motions [69]. For longitudinal wave, the direction of propagation of wave is the same as the direction of particles oscillation. Longitudinal sound waves are the easiest to produce and can be converted to other types. Wave that travels perpendicular to the direction of particle oscillation is called shear wave or transverse wave. Shear waves travel at slower speeds than

longitudinal waves, and can only propagate in solid bodies. As for surface wave, it moves at the surface of a material with the particles moving in elliptical orbits. The last type of sound waves is the plate wave. The movement of particles of these waves are as same as shear wave, but plate waves can only be generated in very thin pieces of material.

The sound velocities in a variety of materials at 25 °C are shown in Table 2-3. What happens when waves travel cross from one medium into another? The propagation of waves normally involves four possible behaviours when exhibiting at the boundary of two mediums, namely reflection, diffraction, transmission and refraction. When sound incidence is perpendicular to the interface, it breaks into reflection and transmission waves without direction alternation. As soon as sound is incident at an angle, the reflected waves have equal angle whereas the transmitted waves undergo a change both in direction and speed known as refraction. The acoustic impedance (Z) is a characteristic of specific material and the product of its density and acoustic velocity. Ultrasonic waves are reflected at the interface of two mediums wherever there is a difference in acoustic impedances. The more difference in Z , the greater percentage of energy will be reflected at the boundary [68, 69]. This phenomenon introduced the definition of reflection coefficient which is expressed in equation:

$$R = \frac{Z_2 - Z_1}{Z_2 + Z_1} \quad (2-5)$$

The calculated values of acoustic impedances and reflection coefficients of common used material are given in Table 2-3 [70]. For example, 88% energy will be reflected when ultrasound wave strikes the interface of water and stainless steel as presented in Figure 2-8. As for the amplitude of the reflected and transmitted waves at water-steel

interface, the reflected wave amplitude is almost the same as the incident amplitude, where the transmitted amplitude doubles the incident one. In summary, the higher density of the medium will always result in a lower wave speed as well as shorter wavelength as ultrasound wave transmitting at the boundary of two mediums. However the frequency of a wave is not altered by crossing a boundary.

Table 2-3 Acoustic impedances and reflection coefficients of common used materials

Material	Velocity m/s	Z X10⁶ kg/m²s	R%
Air	331	0.000426	99.9
Castor oil		1.45	0.09
Water	1495	1.46	0.04
Sea water	1531	1.54	--
Pine		1.57	0.009
Oak	500	2.90	9.4
Polypropylene	920	1.97	5.6
Concrete	3658	8.0	46
Silver	2679	16.7	70
Aluminium		26.3	80
Stainless steel	4998	47	88

What happens to sound wave travelling inside the same medium? By definition, attenuation is the reduction in amplitude of the ultrasound beam as a function of distance through the medium. The propagation of ultrasonic waves in structural materials is preliminary dominated by the degree of texture, anisotropy, elasticity, and homogeneity of the medium [71]. Attenuation is attributed to both of the scattering from microscopic interface in the material and energy absorbed due to heat conversion [69]. Attenuation coefficients are used to quantify the decrease of the transmitted ultrasound amplitude through a media as a function of frequency. Nowadays, power ultrasound application in industry has become well accepted. With the diversity of applications in automotive/electronic/mechanical inspection, optical

cleaning, medical diagnosis, chemical synthesis and process control as well as other industries, ultrasound is playing an important role in modern manufacturing.

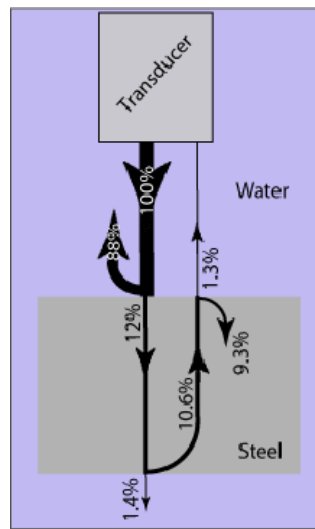


Figure 2-8 Sound energy reflection and transmission at interface of water and steel

2.3.2. Ultrasonic transducer

An ultrasonic transducer has durable functions of generating and receiving ultrasonic vibration. The conversion between the electrical pulse and the mechanical vibrations is the essence for ultrasonic application. The constructions of two major electromechanical transducers are based on either the electrostrictive or the piezoelectric effect [72]. The active element of a transducer is generally a piece of polarized material. As soon as an electric field is applied, the polarized molecules will rearrange the direction to align with the electric field. This phenomenon is known as electrostriction. On the other hand, a polarized material such as quartz (SiO_2) or barium titanate (BaTiO_3) will generate an electric field when subjected to imposed mechanical force, which is called piezoelectric effect. A typical ultrasonic transducer contains several parts, one or more sets of active element such as piezoelectric discs, a protecting plate and housing [73] as shown in Figure 2-9.

Among these segments, piezoelectric disc is fundamental element which transforms electric energy into sound and sound into electric energy reversibly. The protecting plate is normally made of resistant material such as stainless steel and can be mounted on the top of piezoelectric by welding techniques. The main function of the plate is to protect active element from wear and corrosion and serve as acoustic transformer when subjecting to water bath. Practically, an acoustic coupling layer would be applied to improve the sound transmission from the disc through the plate to the medium. The housing is preferably a highly attenuated and dense material such as copper alloy. By adapting different housing materials, impedance between the housing and the piezoelectric can be modified to achieve desired transducer resolution as well as sensitivity.

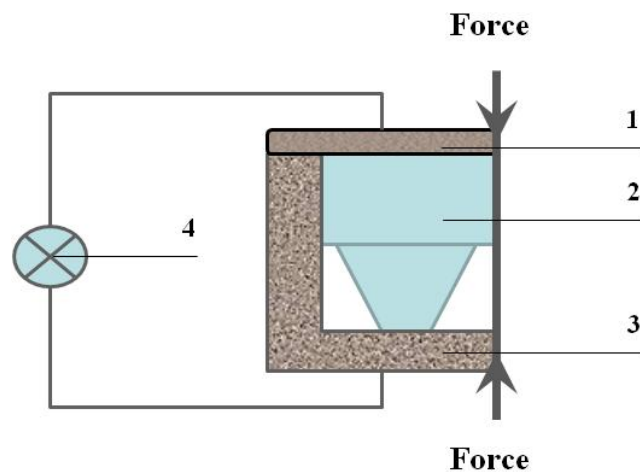


Figure 2-9 Reproduced scheme of transducer: 1 protecting plate; 2 piezoelectric discs; 3 housing; 4 electrical current generator

An analytic formula to calculate the pressure amplitude along the axis of a flat, circular oscillating piston is given by Krantkramer:

$$P = \left| 2P_0 \sin \left[\frac{\pi}{\lambda} \left(\sqrt{a^2 + y^2} - a \right) \right] \right| \quad (2-6)$$

Where a is the transducer radius, y is the distance along the axis from the piston surface, and P_0 is the pressure amplitude at the piston surface. By applying a computer code, Johnson [74] was able to predict the entire expression for the pressure on the axis in the near fields of both circular flat and focused transducers. By selecting specific dimension of piston, material properties and oscillation frequency, the agreement between the theory and modelling calculation was excellent. Comparing the recorded peak value of pressure amplitude, this particular zone had relatively lower steady-state pressure and numerical distortable noise.

2.3.3. Ultrasonic bubble collapse

The collapse of an isolated empty spherical cavity in a liquid under hydrostatic pressure was first analyzed by Rayleigh in 1917 [75]. In his classic work, the radius of cavity was assumed to be zero to generate a collapse velocity. Following this original analysis, experimental and theoretical evidence has accumulated to prove that mechanical damage can only occur when bubbles collapse near the damage surface. Kornfeld and Suvorov [76] proposed the idea that bubble cavities can collapse in asymmetric expression resulting in the formation of micro-jets, which was developed by involution of one side of the cavity and across through, then penetrating to the other side. As the asymmetric collapse occurs near a solid surface, the “water hammer” is formed due to the impact of liquid-solid interface. Advanced observation on actual bubble collapse near rigid surface in static circumstances has been systematically investigated afterwards [77,78]. With the development of modern motion photography technique, the dynamic pattern of bubble collapse could be monitored and confirmed previous hypotheses. In the study of Bourne and Field

[79] carried out on metal surface, they illustrated that the cavities had diameter of 9 mm and produced a shock of 7 GPa when keeping 20mm from the metal surface.

2.3.4. Principal mechanisms of ultrasonic effects in Membrane Filtration

Membrane fouling as well as other filtration processes. The loss of permeability is mainly a combined mechanism of membrane particles adsorption, pore blocking and cake layer formation as well as concentration polarization phenomena. The adsorption of solute particles on the membrane surface is governed by chemical interaction between solutes and membrane material; while the pore plugging is mainly governed by the size of particle and membrane pore size as well as operating condition such as transmembrane pressure, shear rate and temperature [4]. Concentration polarization brings out reversible fouling and membrane permeability is recoverable after certain cleaning process. In contrast, particle adsorption to membrane surface and inside the pores increase the filtration resistance and steer a permanent lose of membrane permeability [59]. In general, the integration of ultrasonic irradiation in membrane filtration is proposed as the consequence of both primary phenomena (cavitation, radiation pressure, acoustic streaming) and secondary phenomena (dispersion, coagulation) [15]. More specifically, possible mechanism for particles being removed or detached from membrane surface with ultrasound irradiation has been proposed as acoustic cavitations, micro-jets (cavitations collapse on the surface of fouling layer), microstreamers (cavitations bubble without collapse inside the fouling layer), microstreaming (motion generated by cavitation bubbles undergo direct oscillation in liquid without collapse) and

acoustic streaming (steady circular waves in high intensity field) as well as associated effects induced by vibration and shock wave, as shown in Figure 2-10 [8].

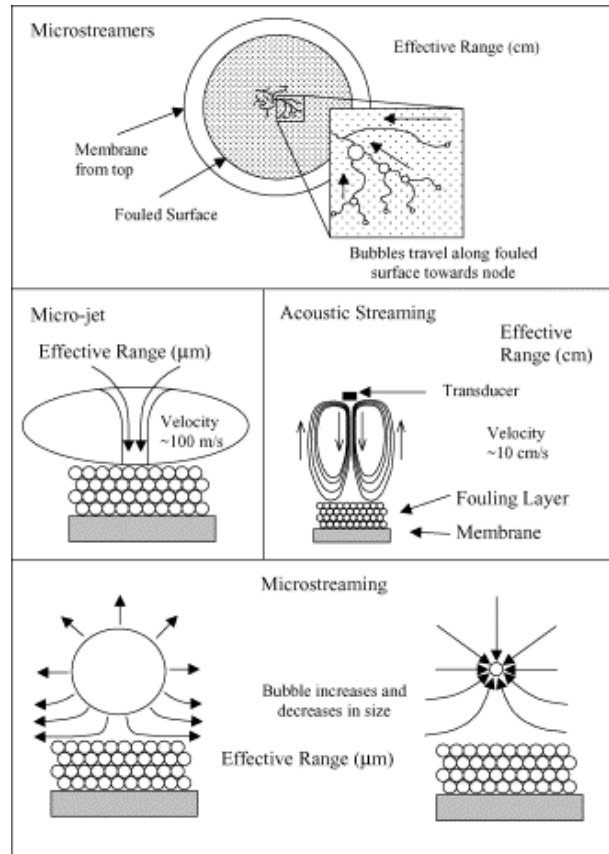


Figure 2-10 Proposed mechanism for particle removal from membrane surface with ultrasound cleaning

2.3.4.1. Acoustic Cavitations

Cavitation refers to the formation and the subsequent dynamic transformation of bubbles in liquid when the pressure of the liquid falls below its vapour pressure. Cavitations can be classified as two types-transient and stable [80]. Cavitation is one of the possible mechanisms to explain the interaction of ultrasound with an aqueous media. In a liquid system, the formation of gaseous cavities is the start of cavitation. During ultrasound compression and rarefaction, the bubble-liquid interface

continually varies in shape and size as liquid molecules diffuse in and out of the bubble core. As soon as the bubble expands to a size that has to surrender to its surface tension, the bubble will collapse (Figure 2-11). The impact energy released by implosion of the bubble collapse burst onto the surface of the object, interactions occurred in both physical and chemical manners. In physical terms a "micro brushing" effect is achieved at high frequency. The chemical effects of ultrasound do not come from a direct interaction with molecular species. Cavitation bubbles collapse generates highly localized extreme of heating (~ 5000 K), and pressures (~ 1000 atm), and enormous heating rates ($>10^9$ K/sec) [81]. Such violent implosions are known as Transient Cavitations and generally can be formed by lower frequency ultrasound with intensities larger than $10\text{W}/\text{cm}^2$ [82]. Shock waves induced by sudden collapse of cavitation bubbles are also contributed to disrupt the flow stability in filtration channel and promote mass transport through membrane.

In contrast to transient cavitations' violent implosions and less than one cycle life time, stable cavitation features the small amplitude oscillations around an equilibrium size [80,83] and last for many acoustic cycles. The lifetime of a bubble is defined as the time period between cavitation inception and the first collapse of the bubble. Thus the lifetime of cavitation bubbles is dependent on whether there is sufficient time for gas or vapor diffusion into the cavity during the rarefactions stage. In a recent study, Arora et al [84] found that increasing the concentration of cavitation nuclei could extend the lifetime of the cavitation cluster.

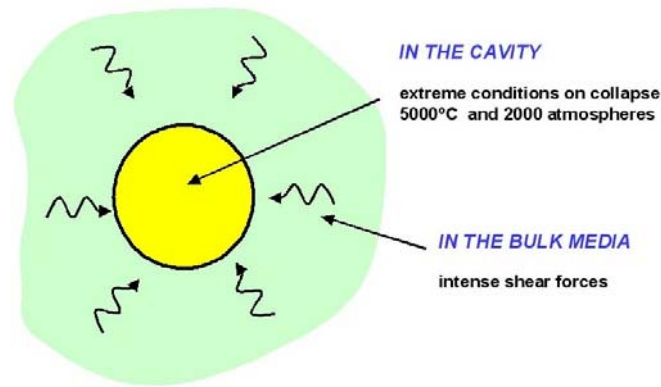


Figure 2-11 Acoustic cavitation in a homogenous liquid medium

Cavitation threshold is the minimum value of the acoustic pressure amplitude required for the microbubbles to undergo transformation. In unsaturated liquid medium, cavitation is associated with gradually presented gas bubbles. Theoretically, when the gas tension is reduced to 25% of its saturation value, cavitation threshold increases linearly up to 7 bars to generate distinguishable, audible violent collapse [80]. The threshold has been confirmed to increase with the increasing of hydrostatic pressure, frequency, power input as well as dissolved ions. In contrast, a decrease in threshold could be associated when increasing surface tension, temperature, dissolved solids and gases. In order to avoid cavitation-induced damage to membrane surface, mild effect can be achieved under the following conditions: high pressure, high frequency, low surface tension, low temperature and contaminant free medium.

2.3.4.2. Acoustic streaming

The formation of acoustic streaming does not require the collapse of cavitation bubbles. Acoustic streaming occurs nearby the surrounding area of the bubbles, oscillates around its resonant size and generates severe shear stress in the medium.

The resonant district of acoustic streaming is around couple of centimetres to tens of centimetres with velocities in the range of 10 cm/s. This removal mechanism is expected to be effective near surfaces with loosely attached particles or dissolvable surfaces [85]. Acoustic streaming can continuously migrate those suspended particles away from membrane surface. The motion velocity is affected by ultrasound frequency, intensity, geometry, liquid density, viscosity and sound speed in the anchored liquid [86]. Higher power intensities tend to generate greater acoustic streaming effect. In addition, with same ultrasound power intensity higher frequency have higher energy absorption and thus greater acoustic streaming flow than lower frequencies [80].

2.3.4.3. Microstreaming

Microstreaming is a time-independent circulation of fluid occurring in the vicinity of bubbles. Bubble radiates acoustic energy when it oscillates thus cause rapid fluctuations along the direction of fluid movement, and promotes significant shear forces [87]. The active range of this mechanism is equivalent to a bubble diameter which depending on amplitude of acoustic pressure and frequency. When a cavitation bubble approaches a cake layer surface, microstreaming will result in a dynamic velocity profile that will exert drag forces on particles leading to its removal.

2.3.4.4. Microstreamers

Like microstreaming, microstreamers are also cavitation mechanisms without a collapse of bubbles. In contrast to the violent collapse of an individual cavity, stable cavitation in a saturated liquid is normally associated with gradually appeared

gas bubbles. It is called “microstreamers”. When a bubble in a liquid is subjected to pressure field, it can undergo volume pulsations. As long as the acoustic pressure gradient is non-zero, it can couple with the bubble oscillations to produce a translational force on the bubble. This is so called the primary Bjerknes force [88]. It is believed that [70, 82] the migration of the bubbles is driven by the Bjerknes force existing between pulsating bubbles in a pressure field [89]. The bubbles travel in ribbon like structures with velocities higher than the average velocity of the media [90], conjugating as they interact with other bubbles.

2.3.4.5. Micro-jet

At liquid-solid interface, collapsing of inertial bubbles near the surface exhibit asymmetric feature and lead to the formation of high velocity micro-jets as displayed in Figure 2-12. The bubble wall accelerates more on the side opposite to a solid surface, resulting in the formation of a strong jet of water with an estimated velocity of 100–200 m/s [87]. The effective range of micro-jets is on the order of the bubble diameter. These liquid jets can penetrate through cake layer built up on membrane surface and still generate secondary stress waves. A research group [83] investigated the shock wave emission as cavitation bubble collapsing on Aluminium wall. Calculating from the propagation velocity of the shock front recorded by a high-speed photography, the peak pressure at the bubble wall can reach up to 8 GPa.

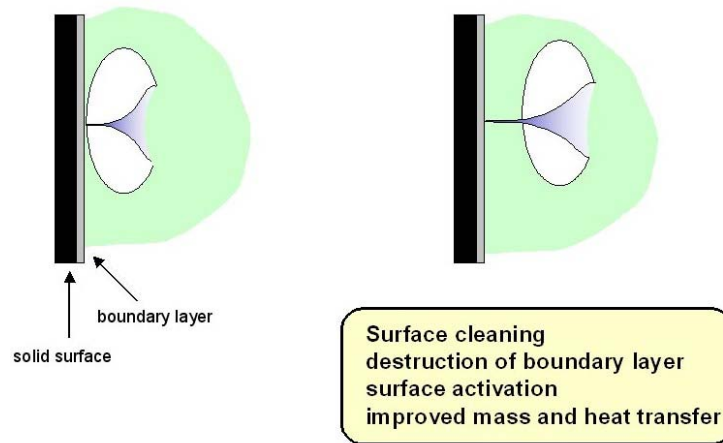


Figure 2-12 Liquid jet generates at liquid-solid interface

Even though numbers of studies reported that ultrasound increased membrane permeability by either reducing the cake layer or by introducing additional shear force, the argument on the effect of acoustic cavitation or streaming has never ceased [91]. The synergized effects are capable of dispatching particles away from membrane surface and stalling particles moving towards the membrane surface. In association with the application of ultrasonic cleaning and defouling, variables contributing to higher cavitation intensity are low frequency, high hydrostatic pressure, and low temperature. On the other hand, more bubbles and large bubbles are formed as acoustic intensity increases till cavitation efficiency reaches to a critical level. Ultrasonic irradiation does not affect the intrinsic permeability of the treated membrane. Ultrasound can work as an additional force to break down the cake layer and decrease the solute concentration polarization layer near the membrane surface but not effective in removing particles which have been plugged inside the pores of membrane. The exact mechanism of ultrasound induced permeation effect is still an open area, more in-depth research and comprehensive discussions are carrying on before serious commercialization of this technique.

Chapter 3. Methodologies & Experiments

3.1. *Radix Astragalus* Extracts

3.1.1. *Radix Astragalus* water extraction

Radix Astragalus water extracts were used as a model solution in this study. The raw herb was purchased from Hong Kong local market and then pulverized into powder by a grinder (DF-15, DADE, China) without any pre-treatment. A conventional solvent extraction method was applied to extract the polysaccharides. Briefly, 100 g of grind sample was soaked in 1 L DI-H₂O for one hour then heated under reflux at 95 °C for one hr. The liquid suspension was filtered and 0.8 L DI-H₂O was added to the remaining residue, followed by extraction for another one more hour. Two portions of polysaccharide suspensions were mixed before the addition of 0.01% NaN₃ (Aldrich, USA) to prevent the growth of bacteria or fungus. The suspension was first vacuum filtered with filter paper of 6µm pore size in double layers before running through crossflow filtration unit. The MW of polysaccharides extracted from *Radix* has broad distribution ranging from 3 kDa to 360 kDa, in which over 40% of polysaccharides have MW greater than 150 kDa [26]. The polysaccharides extracted from *Radix Astragalus* include α-(1,4) glucan, α-(1,6) glucan and a heteropolysaccharide with glucose, arabinose and rhamnose with 9:3:2 ratio. The common physic-chemical properties are that most of the polysaccharides are linear polymers with negative or zero charge and present with random-coil conformations.

3.1.2. Viscosity measurement of polysaccharides extracts

The viscosity of RAE extracts was determined using an Ubbelohde type viscometer. This measurement was conducted in a precisely temperature controlled water bath with temperature varying from 10 to 50 °C. Concentrated RAE suspensions were prepared with rotary evaporator with certain amount of water evaporated under vacuum at 70 °C and then were balanced in water bath before the measurement. The solution viscosity was expressed as a relative viscosity against water.

3.1.3. GPC

Dextran standards and samples were dissolved in distilled water at a concentration of 3.0 mg/ml and analyzed on Gel Permeation Chromatography system equipped with a Waters 1515 isocratic HPLC pump, Waters 2414 refractive index (RI) detector, a set of TSKgel G5000PWxl and TSKgel G3000PWxl columns (7.8 × 300 mm, Tosoh Co., Ltd). GPC measurements were operated at 35 °C employing 0.02 mol/L of KH_2PO_4 as eluent with flow rate of 0.6 ml/min. Injection volumes were 20 μl with a run time of 50 min per sample. The calibration curve was obtained with 6 Dextran GPC standards purchased from Sigma-Aldrich with following molecular weight: 1000, 5000, 12000, 50000, 150000 and 670000. An aliquot of 20 ml sample solution was centrifuged at 6000rpm for 5mins, and the supernatant was collected and filtered with Aervent-50 0.2 μm capsule filter (Millipore) before sample loading process.

3.2. Membrane filtration module

3.2.1. PMMA crossflow cell

A preliminary experimental was carried out with a customized membrane module made of PMMA (Polymethylmethacrylate) according to the description in a patent [41]. PMMA was transparent material so that the dynamic flow could be directly observed and most importantly, acoustic impedance difference between polymer and water was the smallest comparing to other materials. Thus the penetration of ultrasonic irradiation through membrane housing could be maximized. With a test run in ultrasonic water bath, serious corrosion and damage to the cell body were observed as shown in Figure 3-1. The explanation behind this observation might be that some cavitations bubble trapped inside the sealing cavity released heat suddenly in a limit area.



Figure 3-1 PMMA crossflow module

Most membrane modules are now being made with polymer materials. Disposable Millipore Pellicon XL compact module holding fixed PES membrane was applied to evaluate how its screen material polypropylene could withstand US irradiation. DI-H₂O was pressured through membrane module under irradiation of US power of 200 W for 1 hr at TMP of 15 psi. Permeate flux was recorded remaining at 152.8±6.2 LMH constantly. The commercial compact module avoided the formation of cavity so as cavitations bubbles could not accumulate and collapse to cause damage to the body.

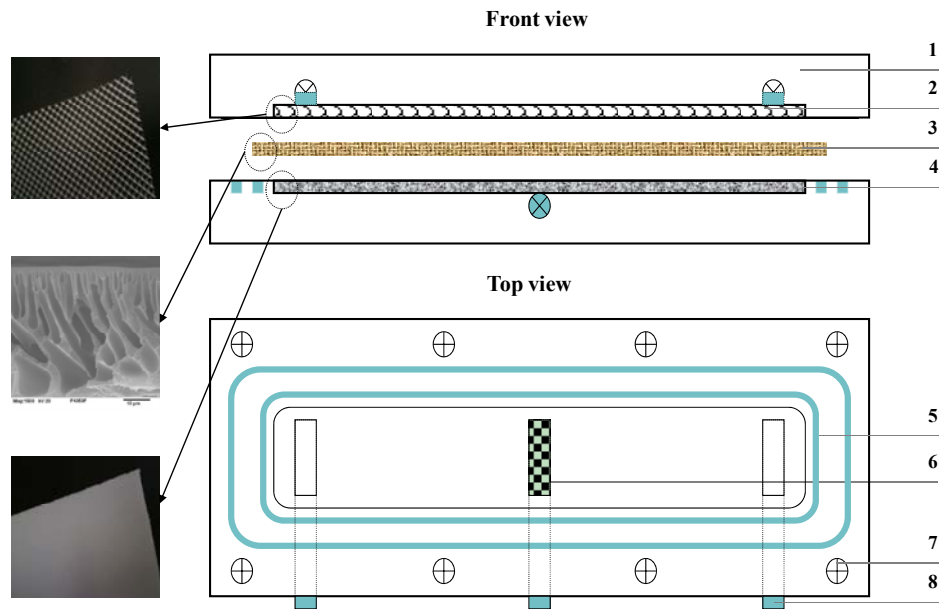


Figure 3-2 The scheme of Membrane Module 1.stainless steel support; 2.Feed/retentate channel and feed spacer; 3.Membrane; 4.Permeate channel and permeate spacer; 5.O-rings; 6.Permeate Openings; 7.Screws; 8.Feed/Retentate/Permeate outlet ports

3.2.2. Stainless steel crossflow cell

Regardless of the weight and cost, in order to withstand the impulsive high temperature and pressure caused by bubble collapse, the entire body of the filtration

cell was made of stainless steel. The scheme of membrane module was displayed in Figure 3-2. The channel dimensions of both feed and permeate were $200 \text{ mm} \times 40 \text{ mm} \times 1.27 \text{ mm}$ (length \times width \times height). The thickness of S.S. housing was 5 mm which remaining 3.73 mm for US to penetrate. The mesh-like feed spacer Naltex PP90, donated by Delstar Technologies Inc., defined the fluid path and promoted greater fluid turbulence, which reduced concentration polarization and membrane fouling. The permeate carrier was made of a porous polypropylene sheet with an average pore size of 80~120 μm . A double O-ring seal in the cell body provided a leak-proof seal.

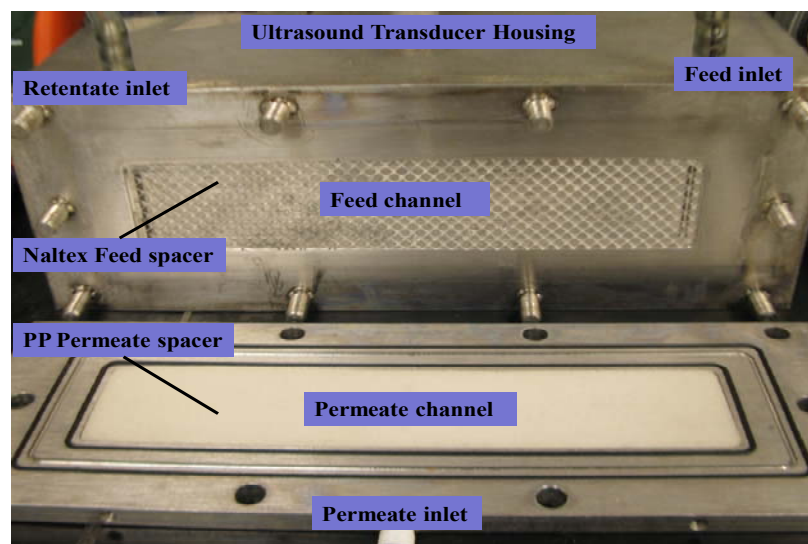


Figure 3-3 Photo of ultrasound integrated crossflow module

3.2.3. Ultrasound transducer integrated CF module

According to the description of US patent 7,161,282 [73], ultrasonic transducer used in fluidic media contains three parts namely a protecting plate, piezoelectric discs and a housing joining together by either welding or mechanical/electrical force.

The plate is normally made of stainless steel and the thickness of the plate corresponds to half a wavelength of the sound in the plate. In our setup, the thickness of stainless steel housing plate was 5 mm. Feed channel of crossflow module was fabricated on the ultrasound transducer housing plate by photo chemical milling process as shown in Figure 3-3. The channel dimensions of both feed and permeate were $200\text{ mm} \times 40\text{ mm} \times 1.27\text{ mm}$ (length \times width \times height). Other configurations were as same as individual S.S. CF cell.

3.2.4. US enhanced CF module vs. US integrated CF module

Two operation systems were defined as shown in Figure 3-4. The upper scheme represented US enhanced CF module in which US transducer and CF cell were separated and operated in water bath. The lower scheme represented US integrated CF module in which US transducer was integrated with CF cell to form a joint piece.

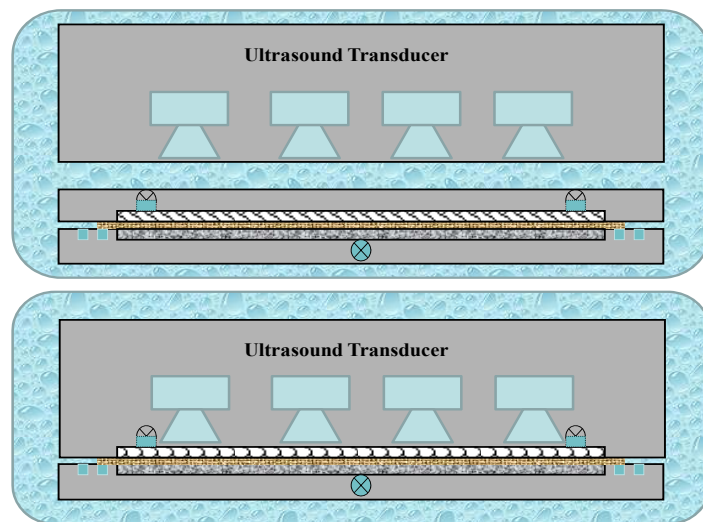


Figure 3-4 US enhanced CF module vs. US integrated CF module

3.2.5. Membrane Characterization

A series of Polyethersulfone (PES; Kochmembrane, USA) membranes with MWCO of 5 kDa, 10 kDa or 30 kDa were used in this setup. Those membranes had average porosity of support layer 0.7~0.8 and skin layer 0.05, tortuosity of 1.5~2.5 and thickness of 250 μm . Virgin membranes were equilibrated with DI- H_2O for 24hrs in order to remove any preservative residues. After each experiment, the fouled membrane was rinsed throughout and reserved in contaminant free DI- H_2O for further use. Membrane surface morphology was examined by a scanning electron microscope (SEM) (JEOL, JSM6335, Japan). All specimens were freeze-dried and coated with a thin layer of gold before observation.

3.3. Ultrasound transducers and intensity measurement

3.3.1. US transducer designed for enhanced CF module

The stainless steel plate (Kamut, China) holding 4 disc ultrasonic transducers inside has dimensions of 280 mm long, 100 mm wide and 80 mm high. The transducers connected with an ultrasonic generator have tunable output power ranging from 0 to 400 W. The plate was immersed in a 320 mm \times 200 mm \times 120 mm stainless steel water bath. Membrane filtration module was positioned 30mm from the transducer surface during ultrasonic irradiation period. Hydrophone measurements were conducted by placing the hydrophone needle aligned with ultrasonic wave. Acoustic pressure represents the amplitude of alternating stress on a

material by propagating ultrasonic wave. An example picture (Figure 3-5) illustrated the distribution of transducer disc inside S.S. body.



Figure 3-5 Distribution of transducer disk inside stainless steel housing

Each of piezoelectric transducer emits spherical ultrasonic waves to the surrounding medium. These spherical waves interfere with each other resulting in a system of maxima and minima in intensity in the near field region. The distribution of ultrasound waves and the intensity of the energy carried by it are defined by ultrasonic beam. The length of the near field is a function of the transducer frequency and the diameter of the crystal, which can be calculated as [92] :

$$N = \frac{D^2}{4\lambda} \quad (3-1)$$

Based on the diameter of transducer disk, the near zone lengths were calculated for three ultrasound transducers used in experiment (Table 3-1). The intensity varies irregularly inside the near field and decreases with the distance.

Table 3-1 Calculated near zone region for all three ultrasonic transducers used in experiments

Frequency λ (KHz)	Diameter D (mm)	Near zone length N(cm)
28	72	2.5
45	45	1.5
100	45	3.4

3.3.2. US transducer designed for integrated CF module

In order to utilize the ultrasound power intensity maximally, a compact and portable filtration module was integrated with ultrasonic transducer. In this setup, the feed side component of filtration module worked as the housing of ultrasonic resonance. Thus the cassette offers dual function of filtration as well as sonication for improved cleaning efficiency. The configurations of US transducer as well as the filtration channel was controlled as the same as previous setup.

3.3.3. Intensity measurement

A needle hydrophone with 1mm diameter tip (Precision Acoustics, UK), power transformer (PAC 300, BIO-RAD, CA, US) and an oscilloscope (TDS 1002B, Tektronix, Japan) was used to measure the US power intensity inside UF cell as well as in the water bath. Membrane filtration module was positioned 30mm from the transducer surface during ultrasonic irradiation period. Hydrophone measurements were conducted by placing the hydrophone needle aligned with ultrasonic wave. Acoustic pressure represents the amplitude of alternating stress on a material by propagating ultrasonic wave.

$$P = \frac{V}{M(f)} \quad (3-2)$$

Where P is the acoustic pressure, V the measured voltage, and $M(f)$ the sensitivity of the hydrophone as the function of frequency 630.96 MV/MPa

$$I = \frac{P^2}{\rho c} \quad (3-3)$$

Where I is the intensity, ρ the density of the propagating medium which is water in our experimental setup, and c is the velocity of sound in water with a value of 1480 m/s at room temperature.

3.3.4. Aluminium foil paper test for cavitation effect

Cavitation effect was evaluated applying aluminium foil paper test method. A section of aluminium foil paper was cut out with the size of 10 cm × 28 cm and weighted. The section was then immersed into ultrasonic water bath vertically facing the shiny side to the transducer while keeping 2 cm away from the surface of transducer. The foil test was conducted for the duration of 1min for each ultrasonic irradiation. After drying at room temperature, the weights of radiated foils were collected. The weight loss of foil paper is proportional to the cavitation effect induced by ultrasonic transducer.

3.4. RAE Ultrafiltration process

3.4.1. Ultrafiltration process control

The schematic diagram of ultrasonic enhanced/integrated crossflow UF system is illustrated in Figure 3-6. The polysaccharide extraction was delivered from a 1L

feed tank through a variable speed gear pump (Micropump 75211-15). The feed solution passed over a digital flow sensor (Colaparmar 32550-11) before entering the channel of crossflow filtration module through an inlet tube. TMP was monitored and recorded by a manometer (Technika, AZ, USA) connected to both feed inlet and permeate outlet. The manometer had a digital display that could measure pressure ranging from -70 psi to 70 psi. A valve on the recirculation line was used to constrain the retentate flow to adjust the TMP alternatively. This setup allowed a precise control of applied TMP and crossflow feed velocity. During the filtration, the retentate was recycled back into the feed tank while permeate was collected and recorded with a digital balance connected with LoggerPro software for data processing. A fresh membrane sheet was used in every single run. Prior to the *RAE* UF process, DI-H₂O was running throughout the system for 30 min under designed parameters (TMP and feed velocity) to condition the membrane and minimize the experimental error. DI-H₂O flux was measured before and after *RAE* filtration for the calculation of membrane resistance. After each experiment, the filtration unit was operated for 1 hr with DI-H₂O to remove any residual left in the circulation system. The temperature of the feed solution during the filtration was kept constant at 22 °C by adding ice to water bath to dispatch the heat generated by ultrasonic irradiation.

Heat generated in water bath was systemically studied. Under the hydraulic condition, the temperature in water bath increased from 24.2 to 24.4 °C with feed velocity of 0.3 m/s and TMP of 15 psi for entire 60 min filtration. With the irradiation of US 200W output under same velocity and TMP, water bath temperature increased from 24.2 to 32.1 °C. 16.5% more temperature increasing was observed as feed velocity was speed up from 0.3 m/s to 0.4 m/s. The incorporation of

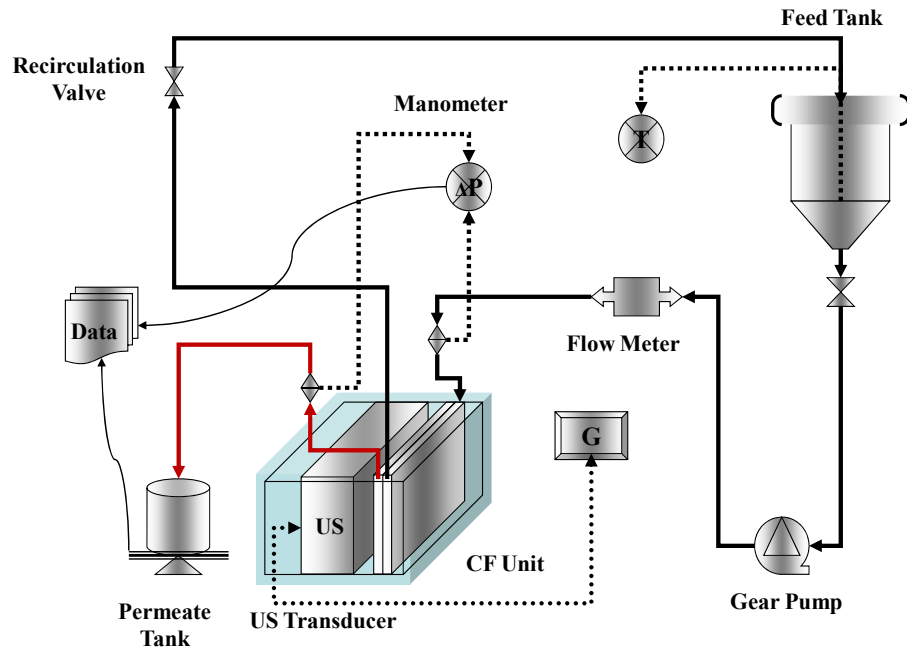


Figure 3-6 The schematic diagram of ultrasonic integrated crossflow UF system

cooling system in this filtration setup could shield the effect induced by heat and emphasize the acoustic effect derived from ultrasound.

3.4.2. Feed velocity & Reynolds number

Reynolds number is a dimensionless parameter used to describe the nature of fluid flow across the surface of object. Our calculation of the Reynolds Number in a rectangular duct was based on:

$$Re = \frac{D_e V \rho}{\mu} \quad (3-4)$$

Where D_e was the equivalent diameter, V was the feed velocity, ρ the density of feed solution and μ the kinematic viscosity. L and W were the diameters of cross-section of crossflow cell. D_e of rectangular duct was defined by:

$$D_e = \frac{2LW}{(L + W)} \quad (3-5)$$

The feed velocity (V) was calculated by

$$V = \frac{U}{A} = \frac{U}{LW} \quad (3-6)$$

Where U was the bulk flow rate. Thus Reynolds number Re can be expressed by

$$Re = \frac{D_e V \rho}{\mu} = \frac{2U\rho}{(L + W)\mu} \quad (3-7)$$

Table 3-2 Reynolds number corresponding to feed flow rate and velocity

Flow rate (ml/min)	Velocity(m/s)	Reynolds number
460	0.150	371
612	0.200	494
918	0.300	741
1225	0.400	989
1530	0.500	1236
1835	0.600	1482
2143	0.700	1731
2448	0.800	1977
2848	0.931	2300

The Reynolds Number can be used to determine if flow is laminar ($Re < 2300$), transient ($2300 < Re < 4000$) or turbulent ($Re > 4000$). The maximum flow rate of experimental set up was operated under 2848ml/min to sustain a laminar flow condition for all runs (refer to Table 3-2) .

3.4.3. Membrane cleaning process

After applied membrane was fouled with *RAE* solution, the feed solution was switched to DI-H₂O for cleaning. In order to characterize membrane regeneration effect, three cleaning methods were introduced to recover membrane permeability,

namely water flushing, ultrasonic on-site cleaning and ultrasonic mobile cleaning. All cleaning durations were kept for 10 min. Water flushing was performed under same feed velocity as *RAE* filtration without permeate stream. Ultrasonic on-site cleaning was carried out without feed flow during ultrasonic irradiation, and ultrasonic mobile cleaning was associated with pre-determined flushing velocity during irradiation process.

3.5. Hydraulic model of filtration resistance

3.5.1. Resistance in series model in *RAE* filtration

The resistance in series model developed from Darcy Law is given as:

$$J(t) = \frac{\Delta P}{\mu(t) (R_m + R_{rf} + R_{if})} \quad (3-8)$$

where R_m is the membrane hydraulic resistance, R_{rf} reversible fouling resistance contributed by cake layer and concentration polarization, R_{if} irreversible fouling generated by particles adsorption to the membrane surface and inside the pores; ΔP the transmembrane pressure, and μ the permeate viscosity. The individual components of resistance were calculated according to a well accepted evaluation method. Both phenomena limited the permeation efficiency by increasing hydraulic resistance to the permeate flow. In all experiments, membrane DI-H₂O flux was initially measured to calculate the membrane resistance R_m . After the filtration with *RAE*, membrane was flushed with DI-H₂O for 10 min under same feed velocity in the filtration channel without permeate flow. The steady state flux was determined by averaging the last 20 recorded value of permeate collection. R_{total} was determined from the steady state flux after fouling and $(R_m + R_{if})$ calculated after water flushing.

For modelling the process, the main mechanisms for flux decline could be defined as standard pore blocking, complete pore blocking and cake formation [93]. The effect of ultrasonic irradiation was evaluated by an ultrasonic enhancement factor defined as:

$$U = \frac{M_{c,us}}{M_{c,w/ous}} \quad (3-9)$$

where M_c represents the total mass of permeate collection after certain filtration period.

3.5.2. Resistance in series model in US enhanced/integrated system

The resistance in series model developed from Darcy Law is given as:

$$J_{(t)} = \frac{\Delta P}{\mu_{(t)}(R_m + R_{cc} + R_{pb} + R_{pc})} \quad (3-10)$$

where R_m is the membrane hydraulic resistance, R_{cc} the resistance contributed by cake layer and concentration polarization, R_{pb} the pore blocking and R_{pc} the pore reconstruction; ΔP the transmembrane pressure, and μ the permeate viscosity. The individual components of resistance were calculated according to a well accepted evaluation method. Concentration polarization and cake formation (R_{cc}) resulted in reversible fouling. Particles blocked the pores of membrane (R_{pb}) can be removed with intensive ultrasound irradiation while some other particles may be trapped into the pores and changed the pore structure (R_{pc}) eventually. Both phenomena limited the permeation efficiency by increasing hydraulic resistance to the permeate flow. In all experiments, membrane DI-H₂O flux was initially measured to calculate the membrane resistance R_m . After the filtration with *RAE*, membrane was flushed with

DI-H₂O for 10 min under same feed velocity in the filtration channel without permeate flow. R_{total} was determined from the steady state flux after fouling and $(R_m + R_{pb} + R_{pc})$ was calculated after water flushing. With membrane cleaning process with ultrasound, $(R_m + R_{pc})$ could be decided.

3.6. Modification of crossflow permeate spacer

As the configuration of crossflow module was mentioned in early section, the mesh-like feed spacer Naltex PP90 was donated by Delstar Technologies Inc. And feed spacer defined the fluid path and promoted greater fluid turbulence, which reduced concentration polarization and membrane fouling. With the enhancement effect induced by ultrasound irradiation, focus was switched to the function of permeate spacer in crossflow cell.

3.6.1. US irradiation onto various materials

In order to examine the effect of material type of permeate support on ultrasonic irradiation efficiency, aluminium foil paper was cut into identical size (4 cm × 20 cm) and then mounted onto various support embodiments including porous polypropylene (PP), Naltex spacer, aluminium plate and stainless steel plate. Ultrasonic irradiation was applied with output power of 200 W for 60 sec after the embodied subjects were vertically positioned at 3 cm away from transducer surface in a water bath.

3.6.2. Stainless steel permeate spacers

Six sets of stainless steel (S.S.) permeate spacers were inserted into crossflow module to evaluate the effect of porosity on permeate flux as well as on RAE filtration enhancement when irradiating with ultrasound in a water bath. As displayed in Figure 3-7, from left to right, the porosity of six spacers were 18.5%, 35.9%, 46.2%, 62.0%, 69.3% and 78.0% and the corner images represented two geometric shapes of spacers cultivated by photo chemical milling process. All spacers had equal thickness of 1.2 mm fitting into the permeate channel.

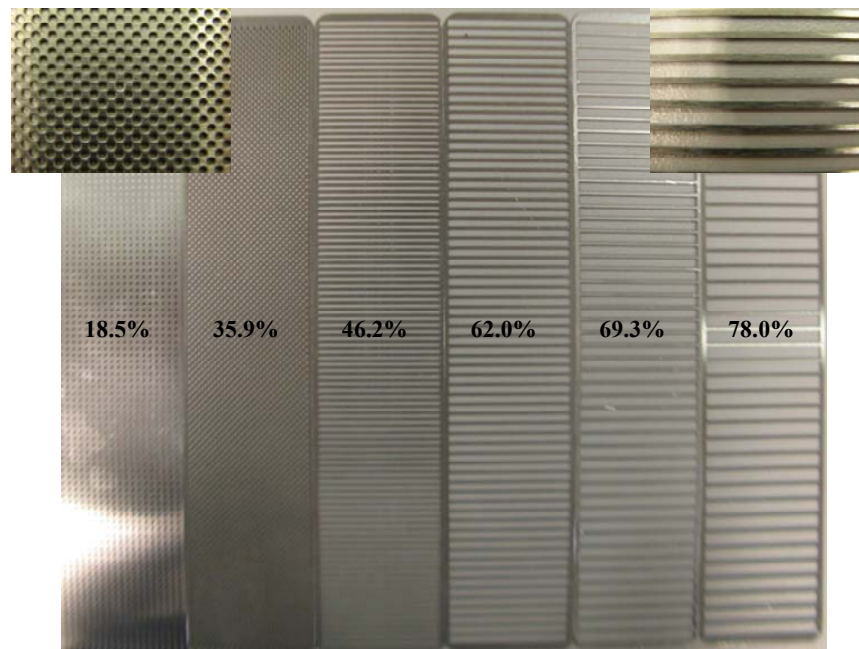


Figure 3-7 Six stainless steel permeate spacer, the porosity of six spacers were 18.5%, 35.9%, 46.2%, 62.0%, 69.3% and 78.0%

Chapter 4. Ultrafiltration Fouling Profile of RAE

4.1. Characterization of US transducers

4.1.1. Intensity in water bath

The intensities, measured at the central point 30 mm away from transducer surface in the water bath, increased linearly with the increasing of generator output power for both 28 kHz and 45 kHz frequency (Figure 4-1). At same output power, intensity measured in 28 kHz water bath was higher than that in 45 kHz. The distribution profile of intensity in the direction perpendicular to the transducer surface along the central line was fairly uniform for both 200 W and 400 W output power with 28 kHz transducer (Figure 4-2). The average intensity was $72 \pm 3 \text{ W/cm}^2$ in the water bath with 200 W, $125 \pm 6 \text{ W/cm}^2$ with 400 W.

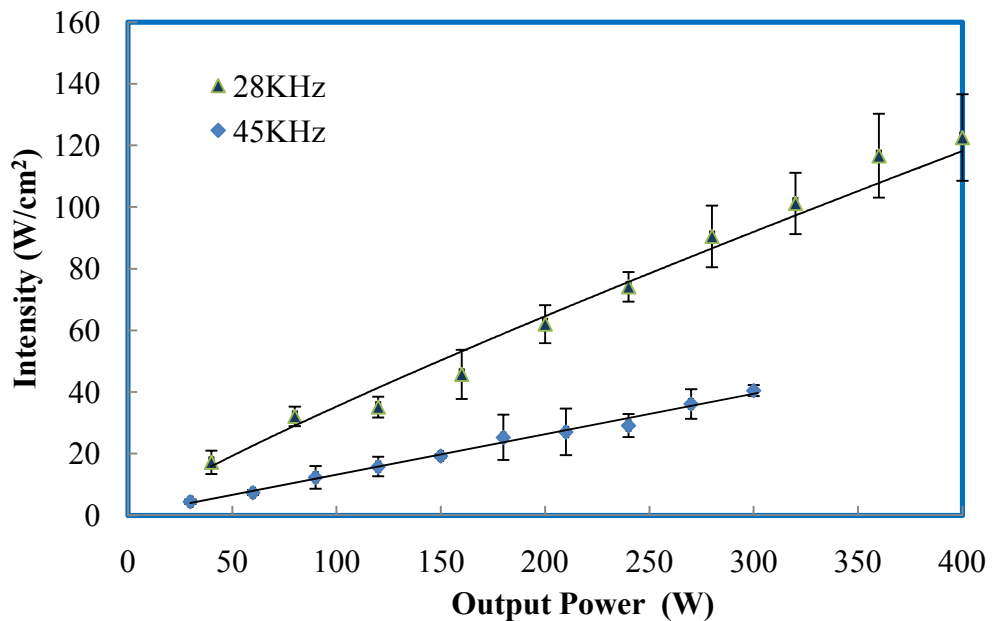


Figure 4-1 Ultrasound intensities measured in water bath at central point and keep 30 mm away from transducer surface for both 28 kHz and 45 kHz

The liability and efficiency of ultrasonic transducer was evaluated using aluminium foil paper test. The experimental data confirmed that ultrasonic cavitation effect increased lineally with the increasing of generator output power. The stronger power could contribute massive collapse of cavitation bubbles. The acoustic pressure is a wave dependent on time, frequency and the maximum pressure amplitude of the wave. The maximum pressure amplitude of the wave is directly proportional to the output power of the transducer.

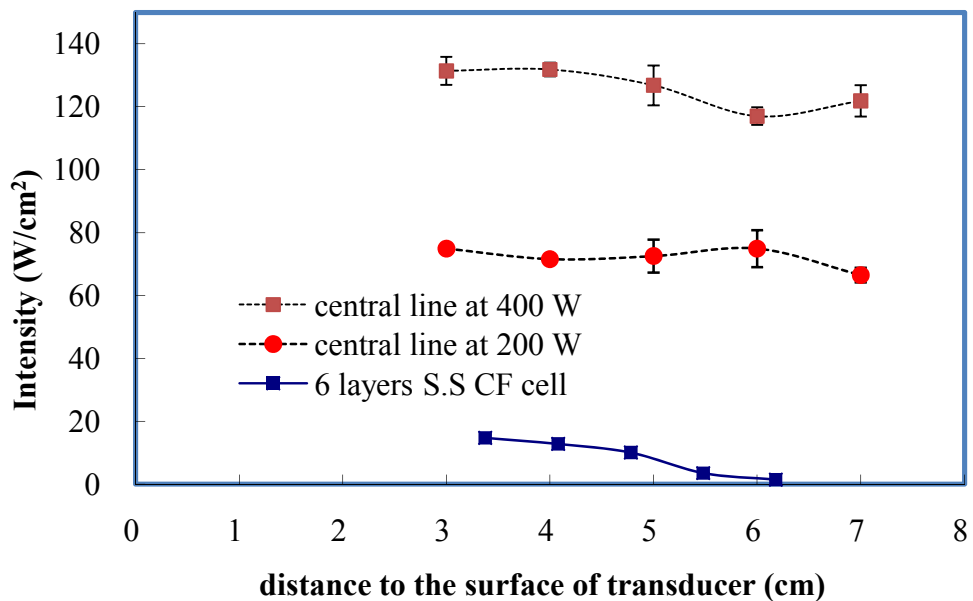


Figure 4-2 US intensity distribution profile along the central line in water bath and CF cell

4.1.2. Intensity in near zone region

According to the description of US 7,161,282 [73], ultrasonic transducer used in fluidic media contains three parts namely a protecting plate, piezoelectric discs and a housing joining together by either welding or mechanical/electrical force. The plate is normally made of stainless steel and the thickness of the plate corresponds to half a wavelength of the sound in the plate. In our setup, the thickness of S.S.

protecting plate was 2 mm. When the hydrophone needle was placed only 1 mm away from transducer surface, the intensity profile distinguished significantly from the measurement at a distance of 3 cm (Figure 4-3). When the output power increased over 200W, the generated acoustic pressure was independent of power. The 28 kHz transducer disc has a diameter of 72 mm, the calculated near field zone length is 2.5 cm. Within the near field zone, since solid-liquid interfaces serve as favourable sites for bubble formation, numerous bubbles and consequent collapse would generate on or near the transducer. In addition, bubble itself absorbing ultrasound energy even further complicated the distribution of pressure amplitude in this region.

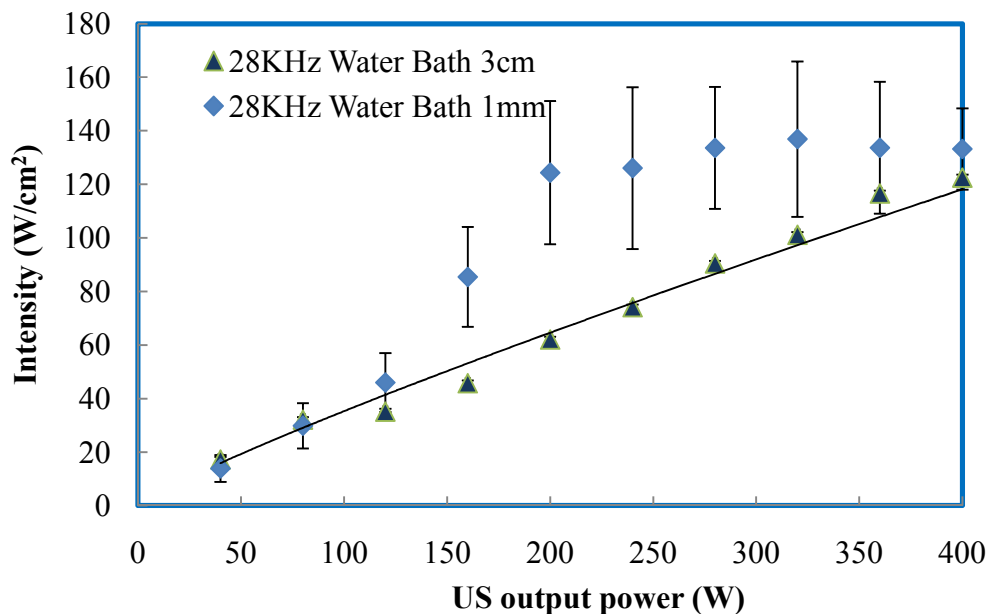


Figure 4-3 28 kHz Ultrasound intensities measured in water bath at 3 cm and 1 mm away from transducer surface

4.1.3. Intensity inside the UF crossflow cell

4.1.3.1. Measured in crossflow cell in water bath

The acoustic impedance of stainless steel was 32 times higher than that of water; therefore, the reflection coefficient of sound travelling at the boundary of the two materials was magnified to 88%. After inserting the hydrophone in the in/outlets of crossflow cells, the recorded amplitude were converted into acoustic intensity. The intensity of sonic power reduces significantly by transmission through the crossflow housing plate even though the thickness was only 3.73 mm. At 400 W output power, intensity detected inside the crossflow channel was 14.6 W/cm^2 , indicating that only 12% of wave intensity could pass through the 3.73 mm crossflow stainless steel housing (14.6 W/cm^2 out of 125 W/cm^2). When 6 pieces of S.S. housing were bound together to form 5 sets of crossflow channels, another 90% attenuation of the ultrasound intensity was detected after propagating through 5 layers of crossflow housings. The measured intensity inside the furthest CF channel was 1.4 W/cm^2 (Figure 4-2). However, in the crossflow filtration setup, a sound intensity of 14.6 W/cm^2 would be sufficient to remove cake layer on the membrane surface according to Kobayashi [15]. The ultrasound waves are affected by the phenomena of reflection, refraction, diffraction and transmission at the boundary, and always accompanied by a change in speed and wavelength of the wave. The amplitude of the pulse was not altered by crossing boundaries but the speed slowed down.

4.1.3.2. Measured in integrated crossflow cell

Due the complicated motions in the near field zone, it was difficult to detect steady ultrasonic signals in this area with hydrophone needle. As shown in Figure 4-4, the steady state pressure amplitude had big variation either at 80 W (left) of output power or 200 W (right) of output power. Johnson [74] applied a computer code to

calculate the linear acoustic wave propagation in the near field. They found that this particular zone had very low steady-state pressure amplitude and had strong numerical noise to distort the wave.

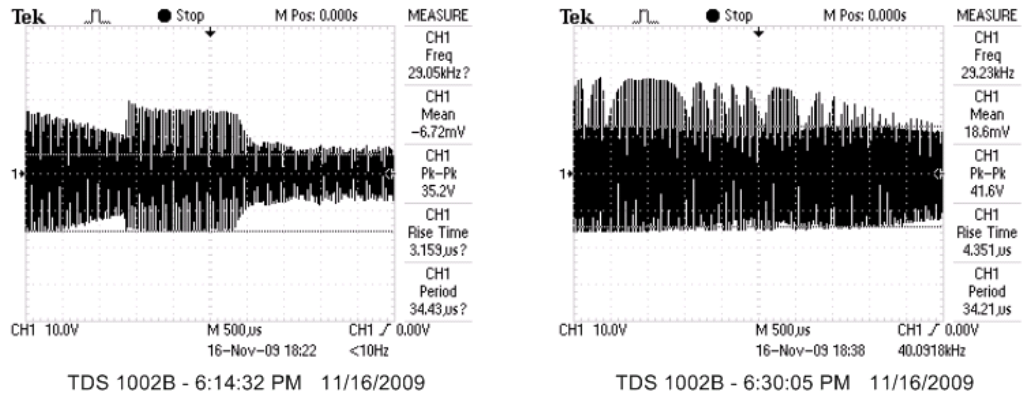


Figure 4-4 Strong noise that distorting the wave in the near field zone

4.2. Characterization of Polysaccharides extract

4.2.1. RAE Viscosity property

Figure 4-5 illustrated the effect of temperature on relative viscosity of RAE extraction at different concentration. The rheological behaviour of virgin extract was almost identical to DI-H₂O with respect to the increase of temperature from 10 to 50° C. In general, the viscosity of the polysaccharide solution increased with the concentration. The higher concentration, the more difference of viscosity between RAE suspensions and DI-H₂O was diagnosed. The viscosity of 8 times concentrated extract almost doubled that of water was 2.33 cp against 1.31 cp.

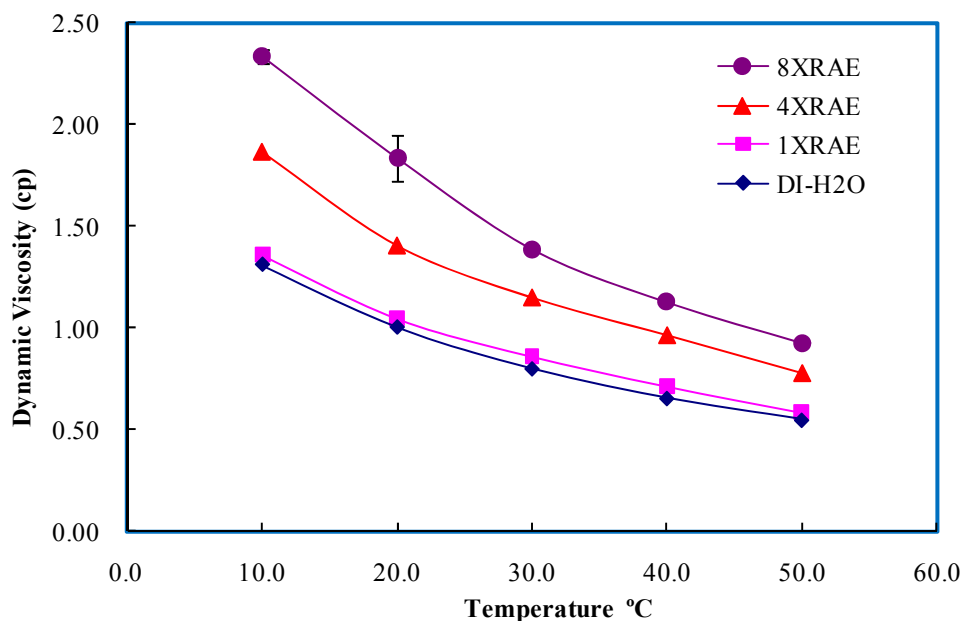


Figure 4-5 Effect of temperature and concentration on rheological properties of RAE

4.2.2. GPC analysis on MW and MW distribution of polysaccharides

4.2.2.1. Original RAE

Five samples were prepared for GPC test, namely, original filtered RAE, retentate and permeate sample from 30 kDa PES membrane separations, retentate and permeate sample from 10 kDa PES membrane separations. In order to eliminate the distortion of organic solvent, investigation was focused on water soluble polysaccharides fractions. All test solutions were derived directly from filtration process without further purification to remove amino acid or protein. As Figure 4-6 displayed, the composition of water soluble polysaccharides in *Astragalus* water extracts were dominated by lower MW polymers with MW of 3 kDa. All five chromatography graphs were nearly identical with autoscale setup.

It was reported [26] that Polysaccharides MW distribution in *Astragalus Radix* extracts have broad range from 3 kDa to 300 kDa. Conducted by ethanol step

precipitation method and separated by serious UF membrane, 38.9% of total polysaccharides had MW smaller than 3 kDa and 43.4% had MW greater than 150 kDa. The majority of MW higher than 150 kDa was branched water insoluble polysaccharides. However, two polysaccharides fractions isolated from *Radix Astragalus* water extract through ethanol precipitation and deproteination were found having molecular weights of 1700 kDa and 1200 kDa [25]. Thus, without deproteination, the interaction between proteins and larger MW polysaccharides [94] which polysaccharides either adsorb onto proteins or form attractions between protein particles can form colloidal suspensions. The suspension became the direct reason that GPC couldn't detect the larger MW composition. Meanwhile, the stability of complex biopolymer mixers may affect the viscosity of process solutions. Moreover, Cho's [95] finding supported the explanation that the protein portion could tightly bind to carbohydrate moiety in *Astragalus* extract to form proteglycans or heteroglycan-protein conjugates.

To further confirm the reliability of GPC results, a new batch of commercial *Astragalus* purchased from Eu Yan Sang was tested following the same protocol as previous samples. GPC graphs validated the composition and components of polysaccharides in *Astragalus* extract. Two larger peaks represented the original extractions from two *Astragalus* recourses, shorter peaks were two sample solutions of 5 mg/ml diluted from polysaccharides dried powders. By this GPC technique, only smaller MW polysaccharides were detected in both *Astragalus* roots.

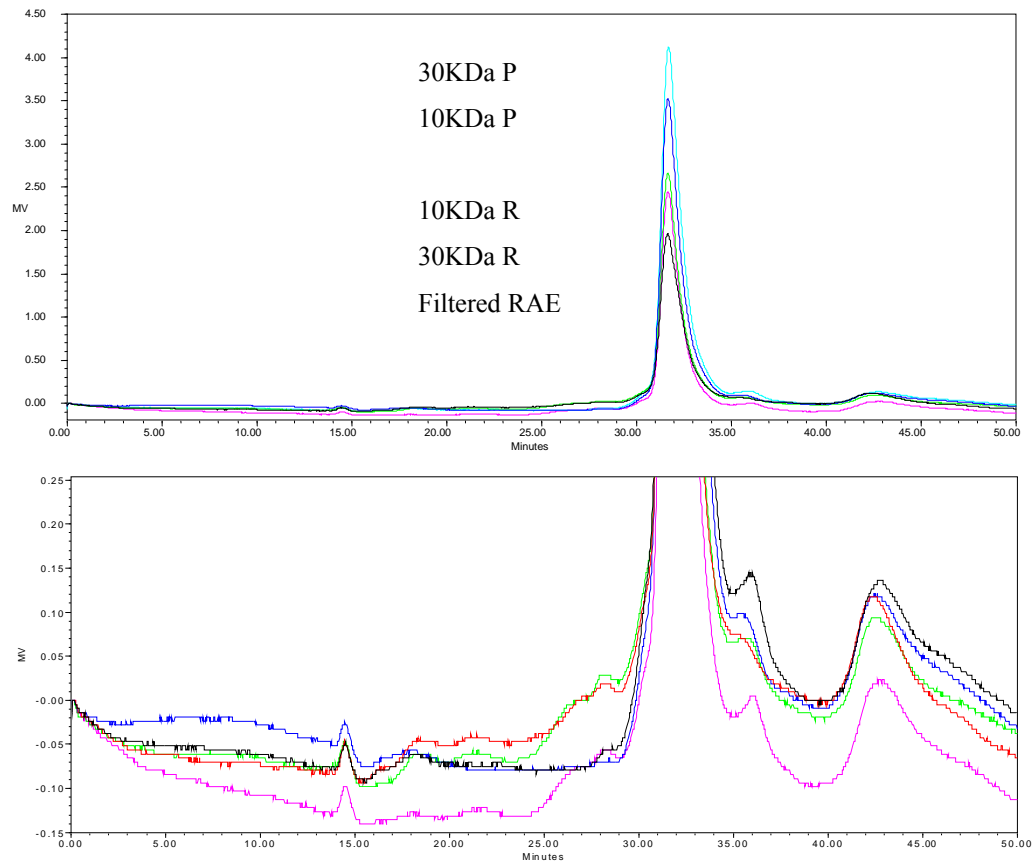


Figure 4-6 GPC results of five original samples

4.2.2.2. US irradiated RAE

Ultrasonic irradiation is one of the most effective mechanical methods to process polysaccharides solution or liquid dispersions in industries in terms of disintegration, intensification as well as depolymerization [96]. Researchers discovered that mechanic destruction of polysaccharides under ultrasonic wave motion was attributed to its cavitation effect. With the consideration of higher intensity measured in integrated crossflow module, the influence of ultrasound irradiation on polysaccharides molecular weight and molecular weight distribution became critical for this application. In order to eliminate the distortion of organic solvent, investigation was focused the effect of US irradiation on water soluble polysaccharides fractions. As Figure 4-6 displayed, the composition of water soluble

polysaccharides in *Astragalus* water extracts was found to be dominated by lower MW polymers with MW of 3 kDa without deproteination process. In order to examine how US could affect the nature of RAE, extreme condition was applied with placing RAE solution in glass beaker and irradiating under 400 W of US output power for continuous 60 min. As shown in Figure 4-7, prolonged high power US irradiation didn't alternative the MW and MW distribution pattern of RAE.

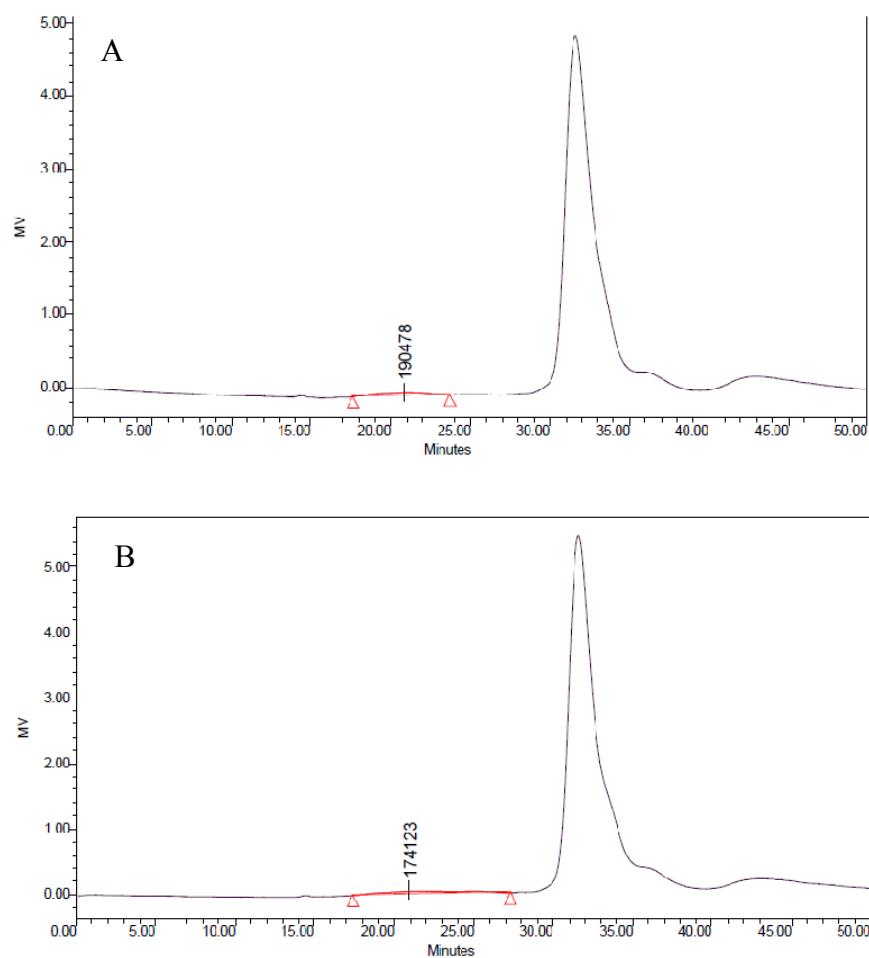


Figure 4-7 GPC chromatography: A: original RAE solution B: ultrasound irradiated RAE solution under 400W 60 min in glass beaker

According to the structures of polysaccharides found in *Astragalus* [25], lower molecular weight amylopectin possessed a near-linear structure similar to liner

amylose. Comparing to linear small MW polysaccharides, branched large MW polysaccharides were more flammable to be affected by irradiation. Szu and co-workers [97] found the destruction of Dextran T2000 under irradiation which resulting a decrease in MW and MW distribution. They also claimed that the repeating-unit structure of polysaccharides could not be destructed by irradiation.

4.3. Ultrafiltration Fouling profile of polysaccharides extracts

4.3.1. ANOVA analysis

Response surface methodology (RSM) is a group of techniques designed to optimize the best value of response. Given this methodology approach, only fewer experimental runs are required comparing to conventional optimization trials. Factor analysis techniques were used to reduce the number of variables as well as to detect relationships between variables. A preliminary fractional factorial design was applied incorporating all major factors that may affect the permeate flux during filtration period: feed velocity, TMP, and feed concentration. All of these parameters could be manipulated as continuous value. The values that represented the highest and lowest levels of each variable were given in Table 4-1, and the corresponding fractional factorial design was displayed in Table 4-2. The independent analysis of variance (ANOVA) (Table 4-3) for each variable confirmed that flow velocity was the most significant variable contributing to higher permeate flux, whereas TMP and feed concentration could be kept constant in the following tests. The ANOVA for each variable confirmed that those variables contributing non-significant to the response could be kept constant.

Table 4-1 The experimental set values for three independent variables

Variables	Range
Feed velocity (ms^{-1})	0.2-0.8
Transmembrane pressure (psi)	15-30
Feed concentration (gml^{-1})	1.3-10.4

Table 4-2 Fractional factorial design and experimental outcomes of total permeate collection

Run	Symbol	TMP(psi)	Velocity (ms^{-1})	Concentration (gml^{-1})	Permeate collection(g)
1	1/15/0.2*	15	0.2	1.3	190.7
2	1/30/0.2	30	0.2	1.3	257.5
3	1/15/0.8	15	0.8	1.3	335.2
4	1/30/0.8	30	0.8	1.3	347.5
5	8/15/0.2	15	0.2	10.4	54.9
6	8/30/0.2	30	0.2	10.4	24.5
7	8/15/0.8	15	0.8	10.4	121.8
8	8/30/0.8	30	0.8	10.4	40.2

*Symbol "1/15/0.2" represents the Ultrafiltration conditions: 1 refers to the original extracts solution without concentration; 15 refers to TMP in crossflow system; 0.2 refers to the feed velocity across the feed channel.

Table 4-3 Regression statistics and analysis of variance (ANOVA) for total permeate collection

Regression Statistics	
Multiple R	0.962491
R Square	0.926390
Adjusted R Square	0.871182
Standard Error	47.092668
Observations	8

	df	SS	MS	F	Significance F
Regression	3	111640.651	37213.5503	16.7801	0.0099
Residual	4	8870.877	2217.7194		
Total	7	120511.528			

	Coefficients	Standard Error	t Stat	P-value	Lower 95%	Upper 95%
Intercept	260.8664	63.2491	4.1244	0.0146	85.2585	436.4743
TMP	-0.5497	2.2200	-0.2476	0.8166	-6.7133	5.6140
Velocity	132.0250	55.4992	2.3789	0.0761	-22.0659	286.1159
Concentration	-31.7764	4.7571	-6.6798	0.0026	-44.9842	-18.5686

4.3.2. Effect of feed velocity

Reynolds number (Re) is a dimensionless parameter used to describe the nature of fluid flowing across the surface of object which can be classified as laminar ($Re < 2300$), transient ($2300 < Re < 4000$) or turbulent ($Re > 4000$). The maximum flow rate of filtration process was operated under 2848 ml/min to sustain a laminar flow condition for all filtration processes. A typical profile of permeate flux as a function of time during crossflow UF of polysaccharides at various flow velocities was presented in Figure 4-8. The symbol of “1/15/0.2” represented that original extracts solution (the weight concentration of total polysaccharides was 1.3% in DI-H₂O) was filtered in crossflow system at TMP of 15 psi and feed velocity of 0.2 m/s as listed in Table 4-2. The rapid flux drops at initial stage of filtration process were observed to be independent of feed velocity. The initial flux drop was caused by pore blocking while the cake formation and the growth of solute concentration gradient in boundary layer were responsible for the afterward gradual flux decline. The thickness and stability of the deposit layer varied depending on the crossflow feed velocity and fluid turbulent patterns [98]. As expected, the steady-state flux increased from 17.4 LMH to 33.9 LMH when feed velocity increased from 0.2 m/s to 0.8 m/s. [99][97] This result corresponded to the conclusion drawn by Lee [20] that higher velocity triggered higher shearing rate and shear-induced hydrodynamic diffusion. In a crossflow filtration channel, particles transportation is regulated by two major forces: the negative force that moving particles towards the membrane surface whereas the positive force shifting them away. The steady flux would be reached as soon as these two forces are equalized. With higher feed velocity, higher steady flux was obtained to compensate for the longer time required to reach this steady value. The permeate

enhancement factor increased from 1.30 to 1.95 as feed velocity increased from 0.3 m/s to 0.8 m/s when comparing to that at velocity of 0.2 m/s.

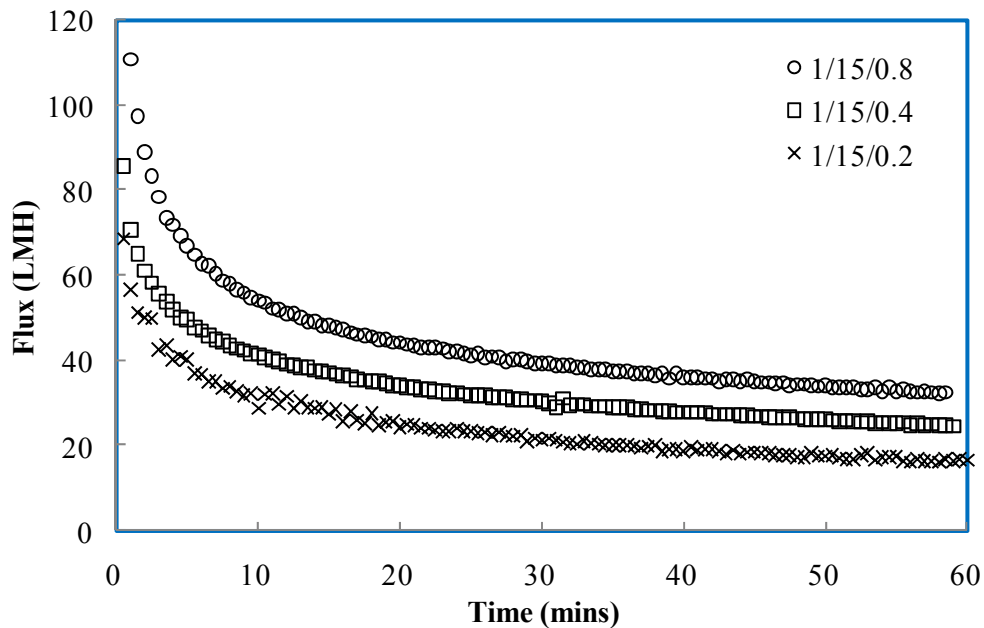


Figure 4-8 Effect of flow velocity on permeation profile of RAE under constant TMP of 15 psi

In order to investigate the influence of feed velocity on fouling characteristics, hydraulic resistances were evaluated with a resistance-in-series model. The total resistances contributed from each fouling mechanism can be manipulated by varying experimental procedure and operating conditions. Microfiltration process adapts the depth filtration mechanism which fouling is dominated by adsorption triggered by inertial capture for larger particles and Brownian diffusion for smaller ones. Rather than that, the screen filtration mechanism in UF is dominated by cake layer formation and concentration polarization. Assumption was made that the cake layer deposited on membrane surface could be moved by circulating water under a moderate flow rate. The value of hydraulic membrane resistance R_m was independent of operation conditions. As the feed velocity was increased from 0.2 m/s to 0.8 m/s, irreversible fouling R_{if} remained relatively constant, while reversible fouling R_{rf}

decreased by threefold (Figure 4-9A). This phenomenon indicated that high feed velocity couldn't retard the rapid collection of particle deposition into the pores but was effective in keeping the particles away from migrating to membrane surface and resulted in a limited thickness of cake layer. A better approach to compare the fouling under various experimental conditions is to plot the total resistance versus total permeate collection as shown in Figure 4-9B. The deposition rate of particle onto membrane surface was highly sensitive to feed velocity under the same operating time. Therefore, increasing the feed velocity under constant TMP favoured both higher steady-state flux and total permeate collection.

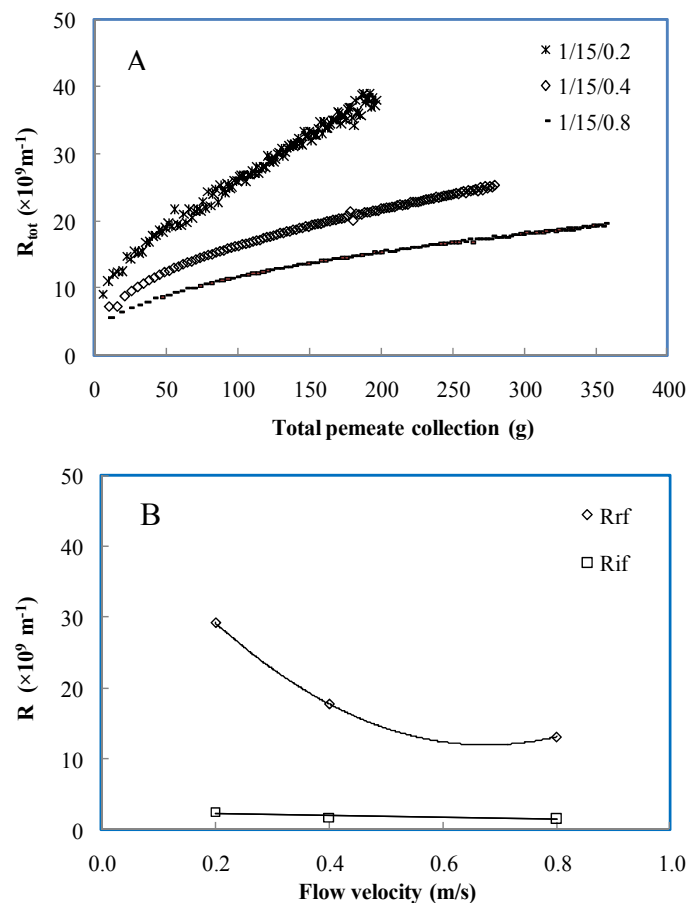


Figure 4-9 Effect of feed velocity on fouling resistance under TMP of 15 psi. **A:** Total resistance as a function of total permeate collection; **B:** Reversible fouling resistance (R_{rf}) and irreversible fouling resistance (R_{if}) as a function of feed velocity

4.3.3. Effect of TMP

In membrane processes, permeate flux generally increased with the increasing of applied TMP. With the operation of original polysaccharides extract under controlled feed velocity of 0.2 m/s, the steady-state flux was discovered to be independent of TMP in the range from 10 psi to 22.5 psi. However, the flux started to decline at when TMP was increased to 25 psi (Figure 4-10). This result correlated with Zhang & Song's research findings [63] and confirmed that the increasing of cake layer thickness compromised the increasing of pressure, which was associated with bulk transport model where the migration of particles toward the membrane was balanced by the back-transport toward the bulk flow. Moreover, as concentration polarization was a result of the building up of concentration gradient of solutes near the membrane surface, the higher TMP was expected to lead to a higher osmotic pressure due to the accumulation and compaction of the fouling layer. The nonlinear relationship between flux and TMP for *RAE* filtration was different from Tansel's [61] discovery on the filtration of bioreactor effluent with RO membrane. As the total permeate collection was plotted against applied TMP by a polynomial function, critical pressure was observed and could be used to screen operational conditions.

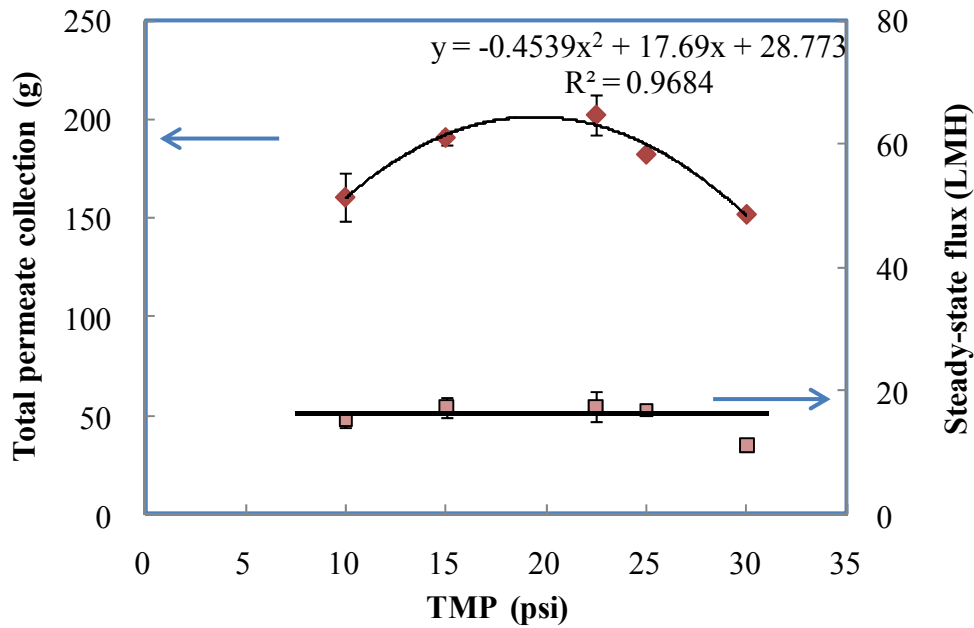


Figure 4-10 Effect of TMP on total permeate collection and steady-state flux at feed velocity of 0.2 m/s

As shown in Figure 4-11A, the reversible fouling R_{if} increased gradually with the increase of TMP while R_{if} remained fairly constant. During the initial stages, membrane fouling could be dominated by pore constriction and pore blocking. Once the foulants had accumulated on the membrane surface to form cake layer, cake formation and concentration polarization became the leading mechanism. However, higher TMP might compress the nascent membrane to result in a higher membrane resistance. The permeate flux data were then converted into total resistance and plotted as resistance versus total permeate collection in Figure 4-11B. Under moderate feed velocity of 0.2 m/s, increasing TMP from 15 psi to 30 psi did not offer any benefit to permeation efficiency in terms of the total permeate collection.

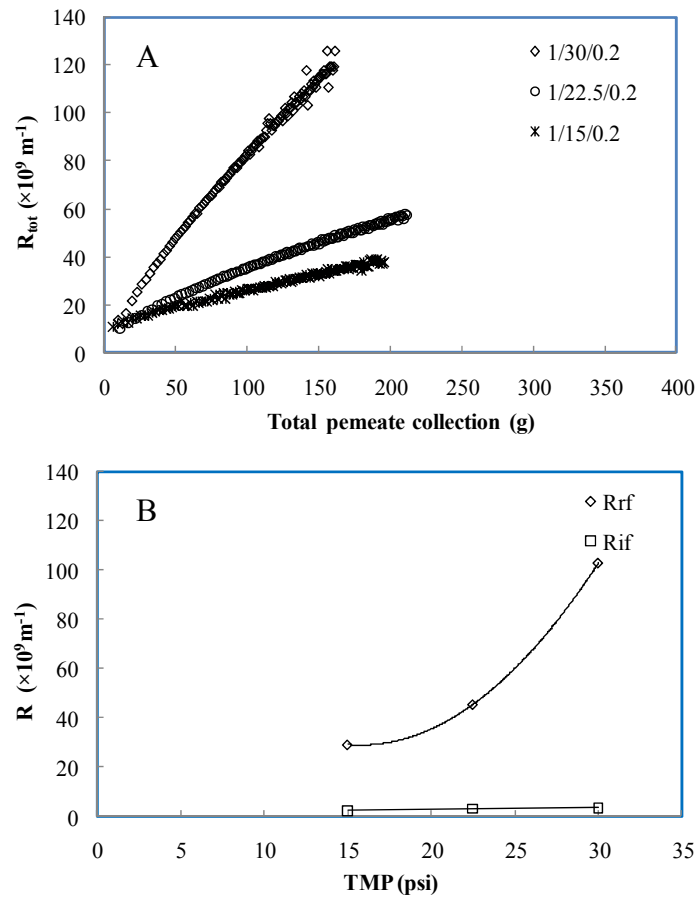


Figure 4-11 Effect of TMP on fouling resistance at feed velocity of 0.2 m/s. A: Total resistance as a function of total permeate collection; B: Reversible fouling resistance (R_{rf}) and irreversible fouling resistance (R_{if}) as a function of TMP

When feed velocity was manipulated up to 0.8 m/s, a deliberate test was conducted to compare 1/30/0.8 with 1/15/0.8 as in Figure 4-12. Predictably, higher TMP not only accelerated the building up of cake layer and resulted in a double reversible fouling resistance, but also aggravated pore blocking behaviour under higher velocity at the initial stage. Corresponding to the results of permeate flux, total resistance mechanism confirmed that the dramatic initial flux decline was dominated by higher irreversible fouling. Conclusion could be made that higher TMP has no influence in boosting up permeation efficiency even with sufficiently high

feed flow. In order to emphasize the ultrasound effect, experimental condition with low velocity as well as low TMP was adopted to generate stronger reversible fouling.

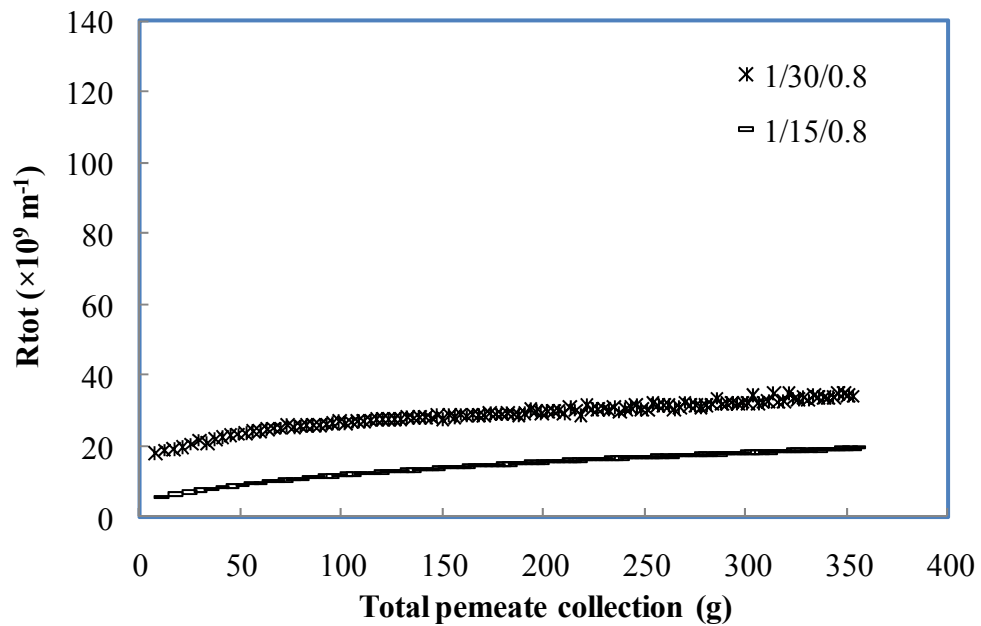


Figure 4-12 Effect of TMP on total resistance at feed velocity of 0.8 m/s

4.3.4. Effect of MWCO

Figure 4-13 demonstrated the permeate flux decline patterns when treating *RAE* with three different PES membranes. Flux decline rate was dramatic at the beginning of operation with MWCO of 30 kDa membrane. This indicated that membrane with larger pore size was more hostile for suspended particles to trap into intramolecular channels of membrane which resulting in severe initial pore blocking. In an extracellular polymeric substances [100] filtration test, the research group claimed that the membrane pore size made great impact on the respective fouling behaviour, the permeate flux couldn't reach at a steady state for mono-dispersed polysaccharides suspensions with 30 kDa membrane. During the UF process of *RAE*

with broader molecular weight distribution, the steady-state flux could be achieved with all three PES membranes. All PES membranes applied in this experimental have same porosity of 5% on skin layer and thickness of 250 μm . According to Hagen-Poiseuille's Law, for those membranes with the same porosity and thickness, the permeate flux would be proportional to the membrane pore size for low solute concentration.

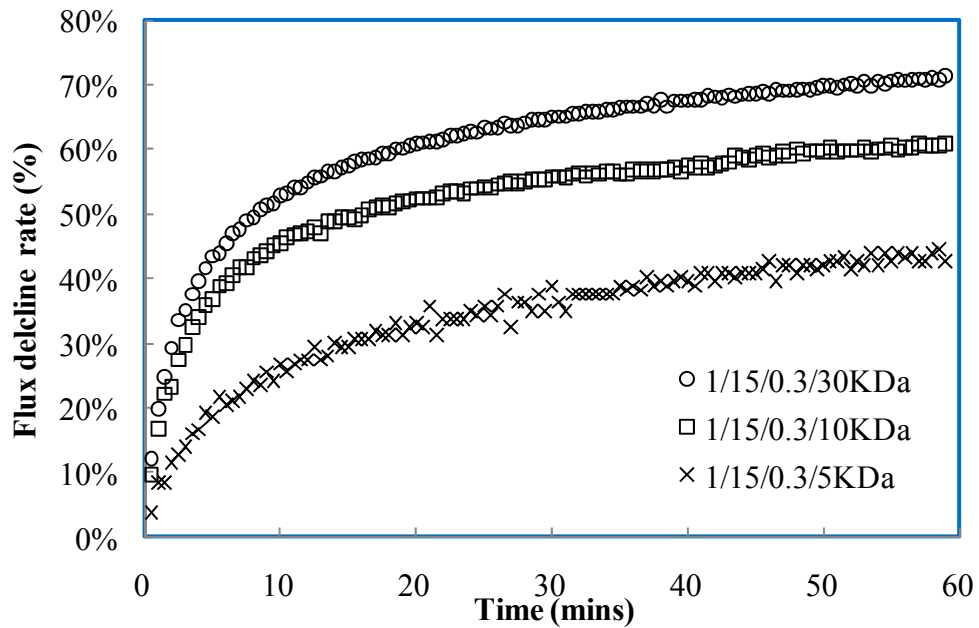


Figure 4-13 Effect of membranes MWCO on flux decline rate at feed velocity of 0.3 m/s and TMP of 15 psi

As total resistance was plotted to the function of MWCO in Figure 4-14, smaller MWCO membrane could generate higher membrane resistance and irreversible fouling resistance. The MW distribution pattern of polysaccharides in *RAE* indicated that high percentage of MW less than 3 kDa led to more severe pore blocking with 5 kDa membrane which having similar pore size.

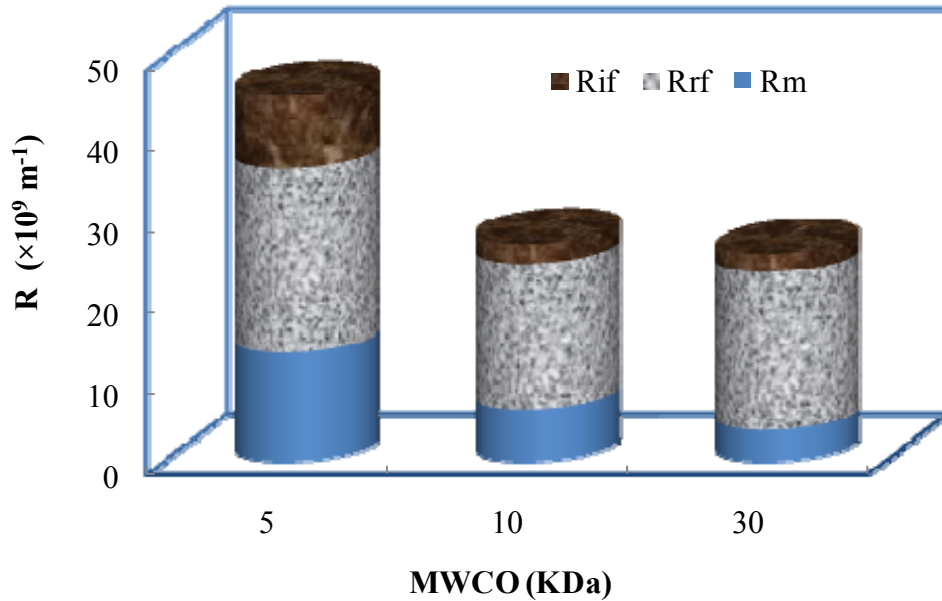


Figure 4-14 Effect of membranes on three resistances (R_{if} , R_{rf} and R_m) at feed velocity of 0.2 m/s and TMP of 15 psi

4.4. Chapter Summary

Two hydrodynamic factors, TMP and feed velocity, played important roles in flux and fouling profiles of *RAE* UF process. Comparing to TMP, velocity was more significant in affecting the polysaccharide fouling behaviour in terms of total permeate collection and steady state flux. The deposition rate of particle onto membrane surface was highly sensitive to feed velocity under the same operating time. Therefore, increasing the feed velocity under constant TMP favoured both higher steady-state flux and total permeate collection. Increasing TMP had no influence in boosting up permeation efficiency even with sufficiently high feed velocity. Membrane with larger pore size (30 kDa comparing to 10 kDa) was more hostile for suspended particles to trap into intramolecular channels of membrane which resulting in severe initial pore blocking.

Chapter 5. Ultrasound enhanced crossflow Ultrafiltration of RAE

5.1. Effect of US frequency

The frequency for high power ultrasound irradiation falls in the range of 16 kHz to 100 kHz. Numerous experiments showed that the use of lower frequency ultrasound reduced pore blockage and initial deposit resistance to result in a higher initial flux [101-103]. In our study, frequencies of 28 kHz, 45 kHz and 100 kHz were applied to assist UF of *RAE* under identical output power of 200 W. The permeate flux profile shown in Figure 5-1 confirmed that 28 kHz was the most effective energy level for membrane cleaning. When the crossflow filtration module was placed into a water bath and kept 30 mm away from the transducer, only 10% of the ultrasonic power could propagate through stainless steel housing. In this setup, ultrasound irradiation acted predominantly through acoustic streaming, microstreaming as well as prompt turbulence rather than cavitation effect. The filtration enhancement factors for all three frequencies were 1.31, 1.16 and 1.07, respectively. Irradiation effect induced by 100 kHz transducer had only a marginal influence compared with the other two frequencies. When investigating the filtration process irradiated with 45 kHz ultrasound, we should bear in mind two distinguished features, steady state flux and the time to reach steady state. In general, the bubble size generated in water bath is inversely proportional to ultrasonic frequency. Furthermore, higher frequency could decrease the production and intensity of cavitation bubbles in liquid. Since the steady state flux and the time it required to reach steady state were strongly affected by the shear rate, the shorter rarefaction cycles caused by 45 kHz irradiation may have positive impact on the shear rate. As frequency increased, the time required to generate bubbles may be longer and more

power would be consumed to make water bubble oscillated [104]. This result associated with the measurement of power intensity inside the UF crossflow channel at opening mode as stated in chapter 4.

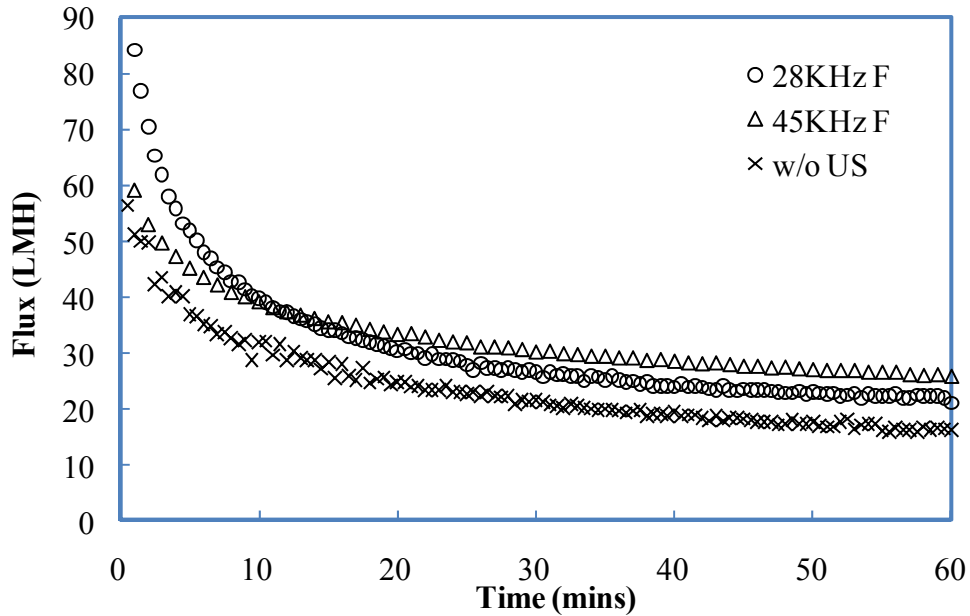


Figure 5-1 Effect of ultrasonic frequency on permeation profile of *RAE* at feed velocity of 0.2 m/s, TMP of 15 psi and MWCO of 30 kDa

5.2. Effect of US irradiation direction

The irradiation direction of ultrasound played an important role in the system design. Kobayashi's group [103] claimed that the highest flux could be obtained when the feed side of the membrane exposed toward the irradiation. The effect of 28 kHz US frequency with 200 W output power on the flux in UF process of *RAE* was examined (Figure 5-2A). The flux decline profile with US irradiating from the permeate side of the membrane was almost identical to that of control process. The trade-off between the increased flow instability induced by US and back diffusion of particles from permeate side against TMP resulted in no effect on flux profile. Moreover, irradiating towards membrane permeate side increased the partial pressure

and resulted as a lower TMP difference across membrane. On the other hand, a significant flux enhancement with US irradiation from the feed side of the membrane was observed, up to 31% higher in productivity than that without US irradiation. It is possible that acoustic streaming induced by ultrasound enhanced the flow turbulence, resulting in a faster transport of polysaccharide particles away from the membrane surface. Moreover, micro-jets towards the feed side of the membrane promoted the convective flow. The transmembrane pressure profile during UF process shown in Figure 5-2B evidenced the effect of US irradiation direction. Irradiated in permeate side of the membrane increased the partial pressure and resulted as a decreased TMP difference across membrane. A slightly increased TMP was monitored when irradiating from the feed side of membrane. Under these circumstances, a perceptible feed velocity variation ranging from 607 ml/min to 745 ml/min presented during the entire filtration.

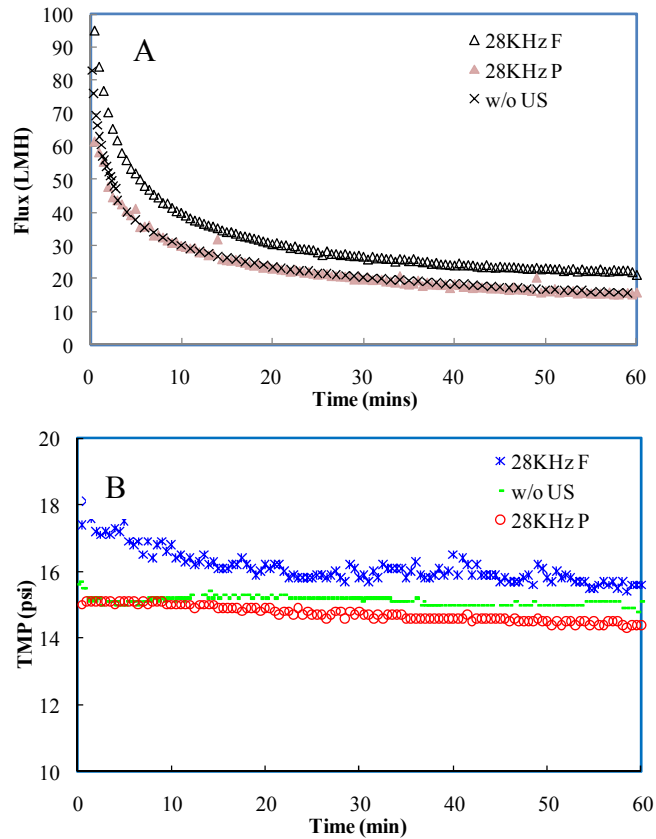


Figure 5-2 Permeate/TMP profile of UF process: without US irradiation versus US irradiation from either feed or permeate side of membrane

Rather than the two conventional parallel positions, alternatively, membrane module can be positioned at any angle to transducer surface. A series experiments were carried out with regarding to varied positions of CF module inside the water bath as shown in Figure 5-3. The angle of 0, 45, 90, 135 and 180 represented the following situations: the feed side of membrane faced directly to the transducer, the feed side of membrane formed an angle of 45 degree with the transducer, the crossflow module was perpendicular to the transducer, the feed side of membrane formed an angle of 135 degree with the transducer and the permeate side of membrane faced the transducer, respectively. The filtration enhancement by US irradiation was maximized to 1.57 at perpendicular position. This result could be explained by the types of wave inside flow channel, besides the common longitudinal

wave, surface wave which generated at the contact area of S.S. feed housing could promote extra motion of particles in feed flow. In a longitudinal wave the particle displacement is parallel to the direction of wave propagation. The particles do not move down the tube with the wave; they simply oscillate back and forth about their individual equilibrium positions.

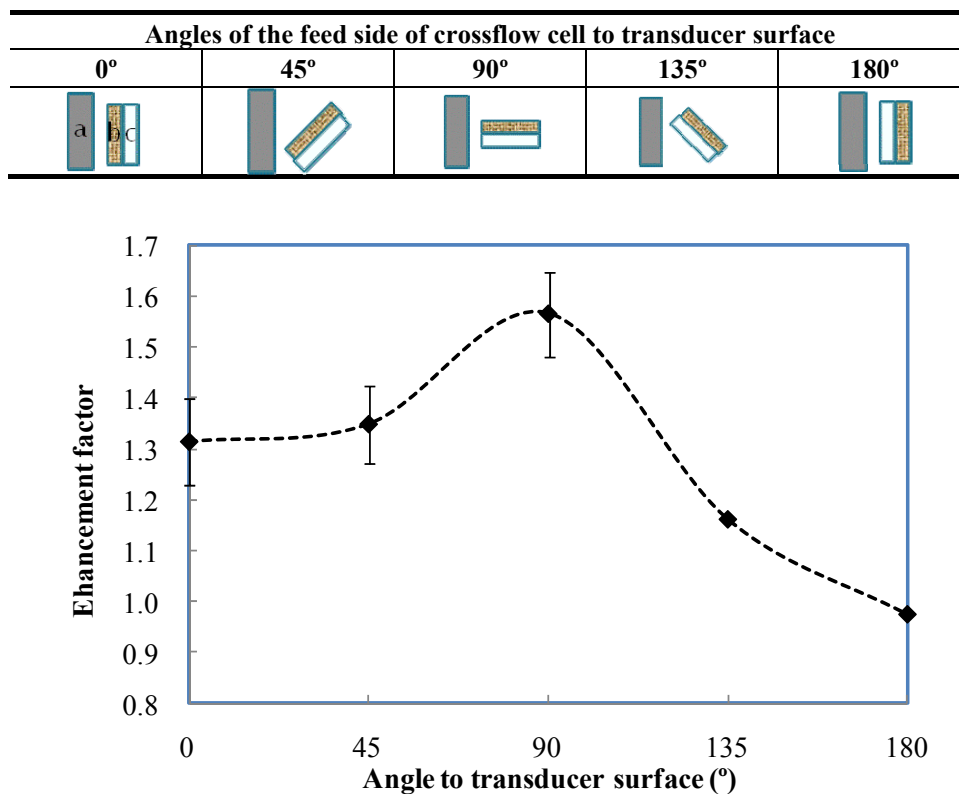


Figure 5-3 Effect of ultrasound irradiation direction on filtration enhancement factor at 15/0.2/30 kDa/200 W. a: ultrasound transducer; b: feed side of crossflow module; c: permeate side of crossflow module

In a transverse wave the particle displacement is perpendicular to the direction of wave propagation. As one-dimensional transverse plane wave propagating from left to right, the particles do not move along with the wave; they simply oscillate up and down about their individual equilibrium positions as the wave passes by. Water waves are an example of waves that involve a combination of both longitudinal and

transverse motions. As a wave travels through the waver, the particles travel in *clockwise circles*. The radius of the circles decreases as the depth into the water increases.

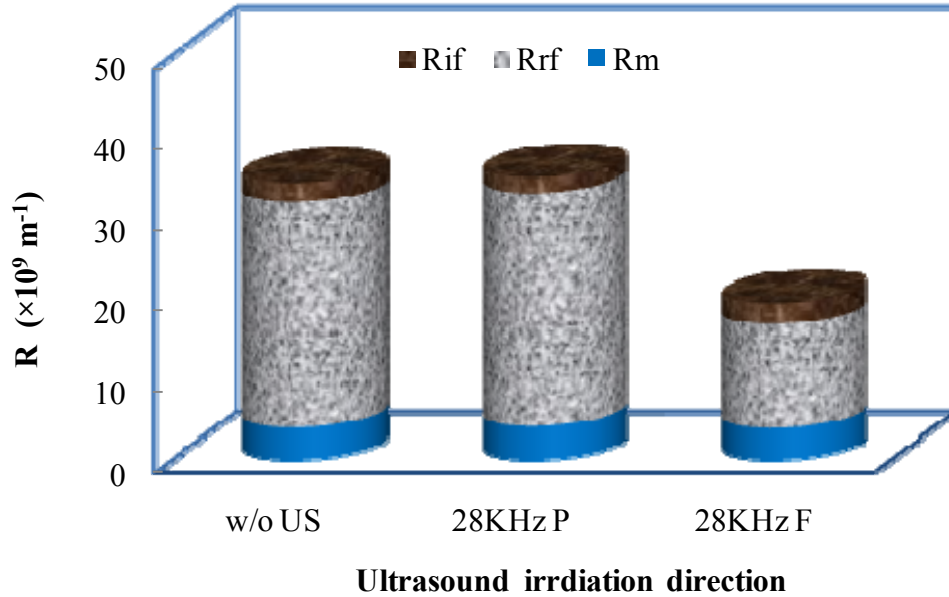


Figure 5-4 Effect of ultrasound irradiation direction on three resistances (R_{if} , R_{rf} and R_m) at feed velocity of 0.2 m/s, TMP of 15 psi, MWCO of 30 kDa, frequency of 28 KHz and output power of 200 W

The effect of ultrasound on reversible and irreversible fouling with respect to total resistance was plotted in Figure 5-4. Reversible fouling was dominant in *RAE* UF process with 30 kDa PES membranes as most components of extracts were able to be retained. The resistance of irreversible fouling R_{if} was 10 times smaller than that of reversible fouling R_{rf} at the end of operation ($2.40 \times 10^9 \text{ m}^{-1}$ comparing to $2.76 \times 10^{10} \text{ m}^{-1}$ at 15 psi). The application of US effectively reduced the total resistance, especially the reversible resistance with nearly 50% reduction when 28 KHz US was applied towards the feed side of membrane. Nevertheless, the irreversible fouling resistance remained the same as that without US irradiation. This phenomenon indicated that the combination of acoustic streaming and liquid jet

generated by lower frequency made strong impact on promoting turbulence near the surface of operating membrane which resulted in reduced cake layer formation.

5.3. Effect of MWCO on US enhancement

As discussed in previous section, membrane with larger pore size was more hostile for suspended particles to trap into intramolecular channels of membrane which resulting in severe initial pore blocking. With 30 KDa membrane under 1/15/0.3 (refer to Table 2) experimental condition, 82% of total resistance contributed by reversible cake formation and concentration polarization. Low intensity US irradiation was more capable to remove cake layer thus generated higher filtration enhancement with 30 kDa membranes comparing to 10 kDa and 5 kDa. As shown in Figure 5-5A, when irradiating with 28KHz transducer at output power of 200 W, total permeate collection increased from 6.4% to 11.3% and 37.1% for membranes with pore size 5 kDa, 10 kDa and 30 kDa, respectively.

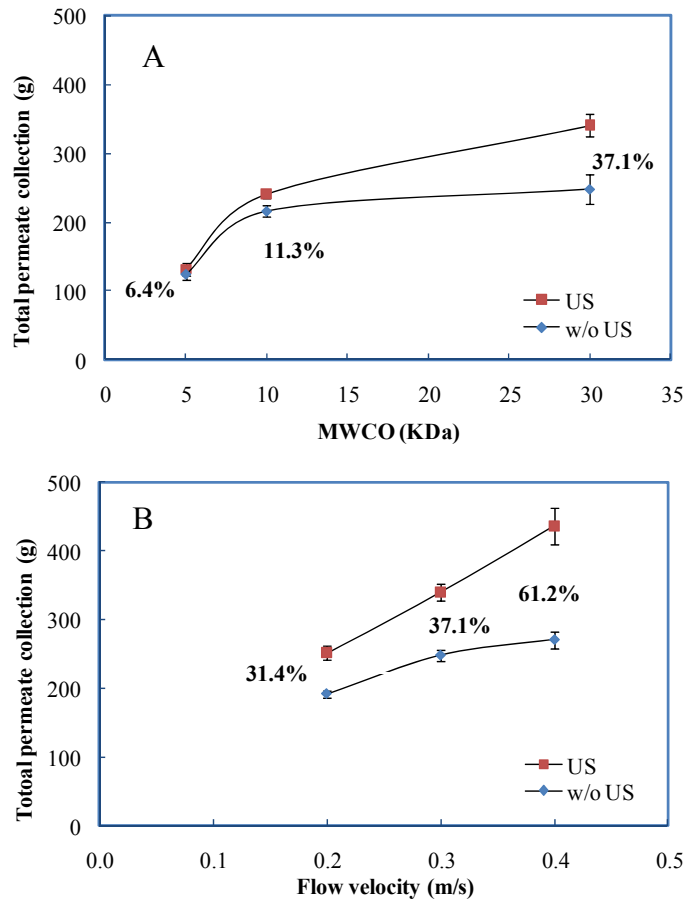


Figure 5-5 Effect of MWCO and feed velocity on ultrasound irradiation enhancement at 15/0.3/28KHz/200W. A: Effect of MWCO; B: Effect of feed velocity

5.4. Effect of feed velocity on US enhancement

The variations of filtration enhancement induced by US irradiation with different flow velocity are displayed in Figure 5-5B. The higher flow velocity, the more significant filtration enhancement occurred. A 60% increase in total permeates collection with 0.4m/s in feed channel was observed. It was not surprising that higher flow velocity could induce dramatic shear force across the membrane surface, at same time decreased viscosity of medium. In turn, less viscous environment favoured the formation of cavitation bubbles and more violent collapse if there was any. The optimal feed velocity is very important for the consideration of energy consumption

in membrane separation. The maximum value of feed flow rate 2848ml/min used in this setup enabled laminar flow inside the crossflow channel with velocity of 0.93m/s. Thus modest feed velocity coupled with the use of US irradiation could control fouling in more efficient system.

5.5. Membrane Morphology

In order to investigate the effect of US irradiation on fouled membrane, the morphology of the prepared membranes was studied with scanning electron microscopy. As can be seen, Figure 5-6A showed a homogeneous cake layer formed on the surface of *RAE* fouled membrane, and Figure 5-6B was the SEM image of membrane after *RAE* filtration assisted with ultrasound for continuous 1 hour duration. Without ultrasonic irradiation, the deposition of polysaccharides particles onto membrane surface formed a dense and compact cake layer. With the treatment of ultrasonic irradiation, different size particles were aggregated to form larger flocs on the membrane surface. This result confirmed that acoustic streaming with its associated shearing stresses could initiate the agglomeration process, which agreed with the finding in Sarabia's [105] work. The application of US could contribute acoustic agglomeration process in which acoustic forces cause particles to interact and eventually to collide.

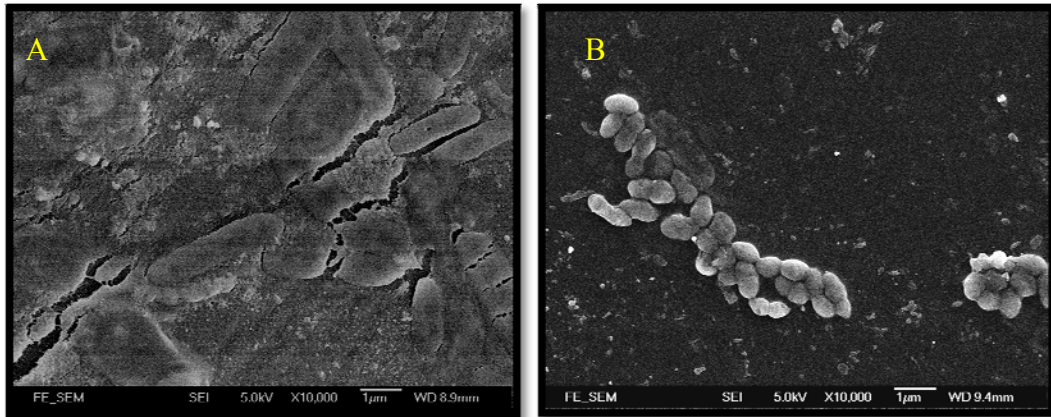


Figure 5-6 Membrane SEM images. A. Fouled membrane generated by RAE Ultrafiltration at 15/0.2/30 kDa; B. treated membrane after 60 min US irradiation during RAE Ultrafiltration at 15/0.2/30 kDa/200W

5.6. Chapter Summary

Ultrasonic irradiation was confirmed to efficiently increase the permeate flux and reduce reversible resistances in UF of RAE. Comparing to 45 KHz and 100 KHz ultrasonic resource, 28 KHz ultrasonic irradiation promoted a 31% increase in permeation efficiency and reduced cake layer thickness when applying from membrane feed side. Other than ultrasonic frequency, feed velocity as well as membrane morphology was all significant factors that can alter the results. Ultrasonic irradiation dramatically increased the total permeate collection for membrane with MWCO of 30 kDa comparing to those of 10 kDa and 5 kDa. Intensity measurement associated with SEM test confirmed that no cavitation ever occurred inside the crossflow channel with dynamic flow even when the output power was scaled up to its maximum value. The major effects induced by ultrasound were due to acoustic streaming, micro-jets as well as the vibration effect.

Chapter 6. Ultrasound integrated crossflow Ultrafiltration of RAE

6.1. Effect of US operation modes

With irradiation of US at 200 W, over 90% more permeation enhancement was observed with this novel integrated design. As significant energy consumption in industry process is concerned, the continuous US irradiation mode to maintain a desired permeate flux has been substituted by the intermittent mode to clean fouled membrane periodically. Systematic experiments confirmed the effects of US on UF of *RAE* and fouled membrane cleaning. Comparing to continuous operation, intermittent US irradiation was more favourable operation mode accounting for its sufficient flux enhancement as well as lower energy consumption. Two comparable filtration processes were initiated, one was operated with US irradiation turning on at the beginning of filtration process and the other setup was only irradiated with US after first 5min running. The durations of US irradiation for both on and off modes were controlled for 5 min accordingly. Experimental data shown in Figure 6-1 suggested that US irradiation at initial stage would minimize both the reversible and irreversible fouling resistance. The overall enhancement factors for these two intermittent filtration processes were 1.91 and 1.92 which were competitive to continue mode (1.88). The permeate flux continued to decrease after US was turned off yet remained higher value than that of without US. Therefore, intermittent US appeared to be as effective as continuous mode, which didn't agree with the results disclosed by Simon et al. [106] and Muthukumaran et al. [11]. They claimed that the ultrasonic energy was inadequate with intermittent mode comparing to continuous mode in a traditional ultrasonic water bath. In contrast, there was no energy lost to the housing barrier in our unique integrate module. Thus under US irradiation of 200

W output power, the two operation modes contributed equal anti-fouling effect in RAE UF process. In continuous irradiation mode, some generated acoustic bubbles might be ineffective and the energy just lost to surrounding comparing to intermittent mode [107]. The second feature worthy of pointing out was that after water flushing, membrane permeability was recovered 100%.

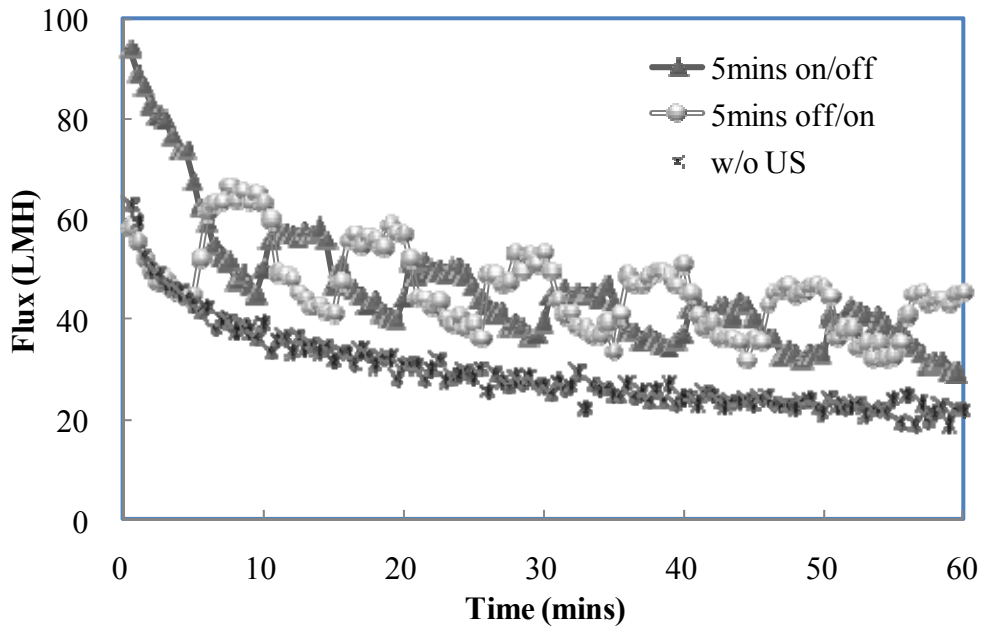


Figure 6-1 Effect of irradiation mode on filtration profile of RAE at 200 W output power, TMP of 15 psi and feed velocity of 0.2 m/s

Moreover, US irradiation was observed to intensify the fouling phenomena when applying on a fouled membrane in UF assisted module. In this case, US might worked as additional force to accelerate the particles blocking into the pores of membrane and condensed the concentration polarization as well as cake layer, thus resulted in a further decline in flux. A patent [108] claimed that ultrasound can be used to free or disperse molecules interspersed or entrapped within membrane. Interestingly, almost 100% DI-H₂O flux recovery was obtained after the US integrated filtration only flushing with DI-H₂O at 0.2 psi. As the energy consumption

and the potential of damaging those active components in extracts are taken into consideration, how and when to apply US in UF process became critical in system design.

6.2. Effect of US output power and characterization of US transducer

Ultrasound is a form of mechanical energy, while piezoelectric transducer is the device to convert electric energy to acoustic energy. The fundamental effect of ultrasound on a continuum fluid is to introduce additional acoustic pressure upon the existing hydrodynamic pressure in the system. The acoustic pressure is the function of time, frequency and the maximum pressure amplitude of the wave [91]. The maximum pressure amplitude of the wave is directly proportional to the output power of the transducer

$$P_{\alpha} = P_{\alpha,max} \sin(2\pi ft) \quad (6-1)$$

Figure 6-2 demonstrated the effect of ultrasound output power on *RAE* filtration profile. In our previous findings, the overall fouling profile of polysaccharides suspension extracted from *RA* was dominated by reversible fouling and the initial flux decline was contributed by pore blocking and pore adsorption. Under the dual functions of acoustic pressure and hydrodynamic pressure, the particles attempted to transport to membrane surface. As US output power increased, the initial permeate flux remained relatively constant while the flux decline rate decreased with time being. This phenomenon indicated that ultrasound irradiation did not alter the migration of suspended particles to the open pores of membrane at beginning but did reduce the migration speed. At sufficiently low amplitude, nucleuses in acoustic field were stabilized. With the increasing of power intensity, nucleuses grow into vapor-

filled bubbles and cavitation bubbles continually increase the number and size. Moreover, near field pressure waves generated acoustic streaming inside the liquid as well as micro-jets at liquid-solid interface. As soon as the field amplitude reaches to sufficient level to surpass cavitation threshold, bubbles collapsed and generate implosive energy. The Results of increased enhancement factor with the increasing of power intensity revealed that the greater number of cavitation bubbles, the more expanded turbulence and the larger zone of cavitation were capable of better cleaning the membranes than lower power intensities.

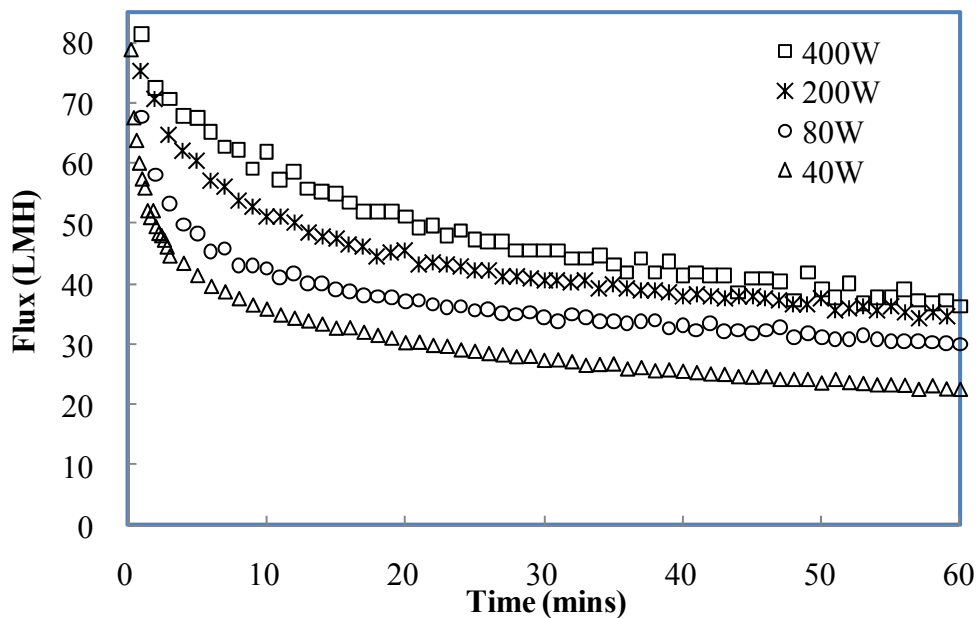


Figure 6-2 Effect of US output power on RAE filtration profile at TMP of 15 psi and feed velocity of 0.2 m/s

The ultrasound intensity was divided into lower intensity and high intensity region by setting 200 W as transit point shown in Figure 6-3. In lower intensity region, filtration enhancement increased dramatically with the increasing of power output. While in higher intensity region, as the power output increased from 200 W to 400 W, the enhancement factor increased only from 1.88 to 2.04. This result

corresponded to the intensity measurement within near zone field and far zone field shown in chapter 4. The measured near field pressure as the function of output power agreed qualitatively with the filtration enhancement outcome. Within the near field zone, since solid-liquid interfaces serve as favourable sites for bubble formation, numerous bubbles and consequent collapse would generate on or near the transducer surface [109]. In addition, bubble itself absorbing ultrasound energy could complicate the distribution of pressure amplitude in this region. Moreover, transit wave generated as wave reflection between the transducer and the tank wall could also blur the energy distribution in ultrasonic field [110]. This indicated that in near field irradiation cavitation induced effect could reach its limitation since additional ultrasonic power might be converted to heat [83]. As consequence, because the huge variations of waves in the near field, it was difficult to measure the intensity accurately. And the increasing output power did not necessarily benefit *RAE* filtration process in this integrated crossflow module.

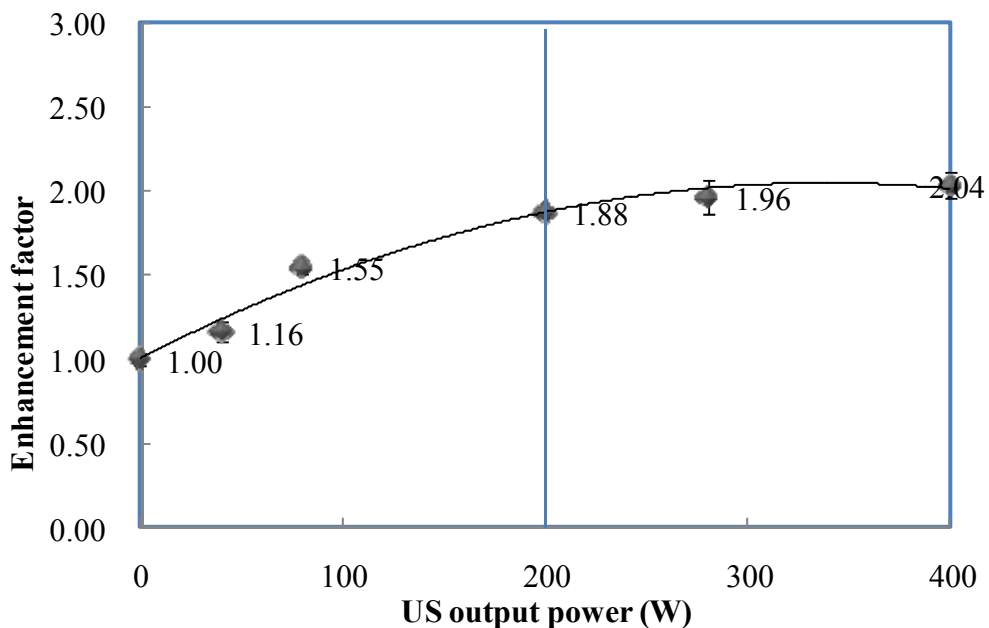


Figure 6-3 Effect of US power output on filtration enhancement factor

6.3. Effect of feed spacer

The spacers in industrial UF applications have dual function of keeping adjacent membrane apart and of promoting turbulence in the feed channel. Inside the crossflow module, the spacer was used to induce unsteady flows and increase local shear force so as to reduce the boundary layer of solutes [5]. As shown in Figure 6-4, without US irradiation, the total permeate collection without feed spacer under the condition of TMP of 15 psi and feed velocity of 0.2 m/s was 133 g in 60 min filtration comparing to 196 g with spacer inserted. The result evidenced the function of feed spacer as reducing the cake layer and concentration polarization. When applying 200 W of US irradiation in crossflow without feed spacer, the building up speed as well as the thickness of cake layer were significantly reduced. The US enhancement factor without feed spacer reached to 2.02. Correlating this data with the US enhancement factor for regular setup 1.91, it appeared that the insert spacer did not interfere US defouling effect.

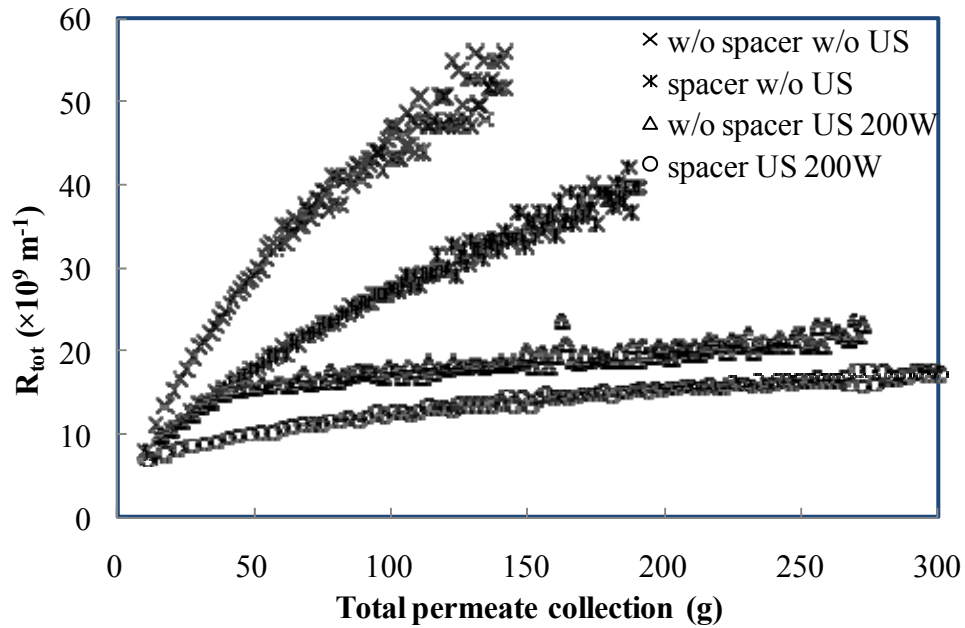


Figure 6-4 Effect of feed spacer on fouling resistance at TMP of 15 psi and feed velocity of 0.2 m/s

6.4. Effect of pre-filtration of feed solution

RAE suspension was originally filtered with 6 μm filter paper to remove large size undissolved residues. In order to picture the overall effect of nascent polysaccharides extraction, non-filtered (NF) extracts was running through the crossflow channel under standard experimental condition (1/15/0.2). Calculated with resistance in series model, NF extracts dedicated almost threefold of resistance by cake layer and concentration polarization comparing to filtered extracts ($7.20 \times 10^{10} m^{-1}$ vs. $2.69 \times 10^{10} m^{-1}$) as displayed in Figure 6-5.

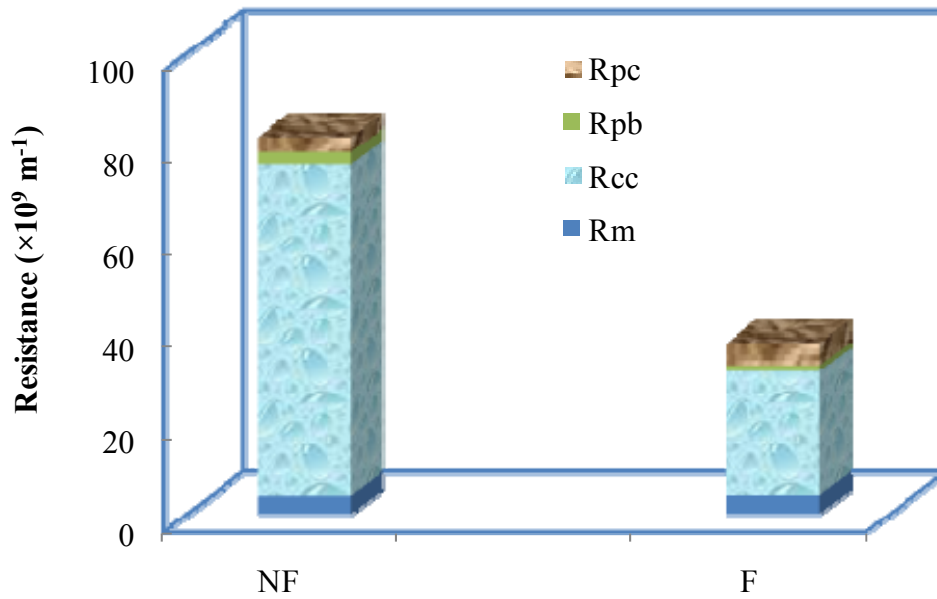


Figure 6-5 Effect of pre-filtration of RAE on total resistance

Given the assumption that US is more effective in reducing reversible fouling caused by cake formation, under this circumstance, integrated US irradiation should be able to engage promising effect on NF feed solution. Unfortunately, with continuous US irradiation at 200 W output power, the filtration enhancement factor was 1.52 and DI-H₂O flux after water flushing was only recovered to 44.6% as shown in Figure 9. Unlike water flux was 100% recovered with filtered *RAE* solution, the introduction of US irradiation on NF *RAE* filtration profile had limited on flux enhancement and the steady-state flux was 27% less than US free process for filtered *RAE*. As we expected, particles with different size in a polydisperse suspension would compete to each other when depositing onto membrane surface, which smaller particles would deposit first and then larger particles would accumulate onto the existing layer formed by smaller ones [111]. Most precipitated residues in *RAE* extracts were polysaccharides with molecular weight larger than 150

kDa and other macropolymers. Thus US irradiation had little effect on removing this top layer.

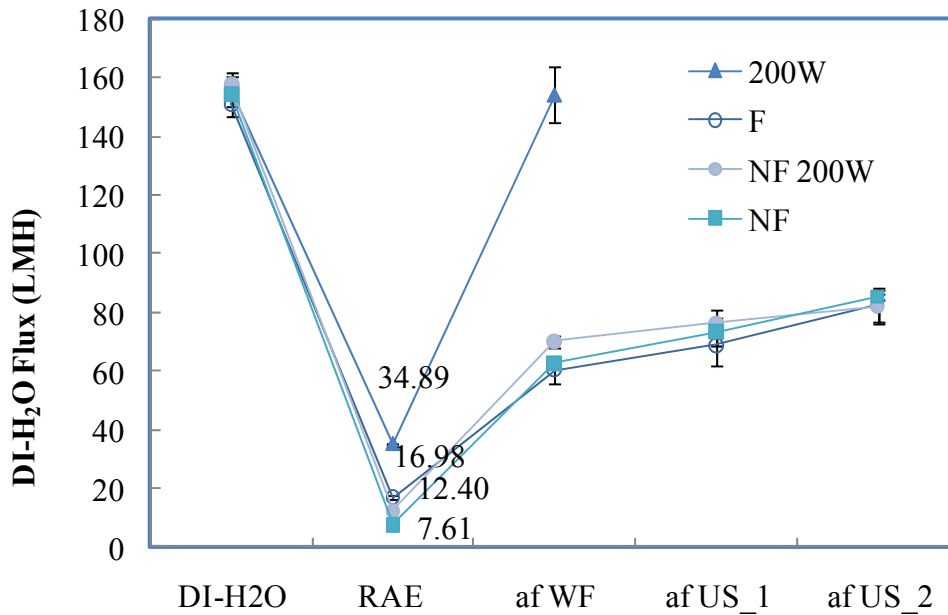


Figure 6-6 Effect of US on filtered and non-filtered RAE suspensions

6.5. External Ultrasonic Cleaning

After PES membranes were fouled in crossflow filtration, they were cleaned by placing the membrane directly into ultrasonic bath. The morphology of four membranes was studied through scanning electron microscopy as shown in Figure 11. The fouled membrane was uniformly covered with dense cake layer (Figure 6-8A). After water flushing for 10 min, only larger and loose particles were removed (Figure 6-8B). With the irradiation of 400W output power ultrasound for 10min, the dense cake layer was break down and formed a few larger aggregations remaining on the membrane surface (Figure 6-8C). After continuous irradiation under 400W for one hour, the membrane was completely clean (Figure 6-8D). No visible damage to the membrane was observed and the membrane was put back to crossflow cell for

DI-H₂O flux measurement. 100% flux recovery was obtained. This result confirmed that cavitation effect under high power ultrasound caused no damage to applied membranes.

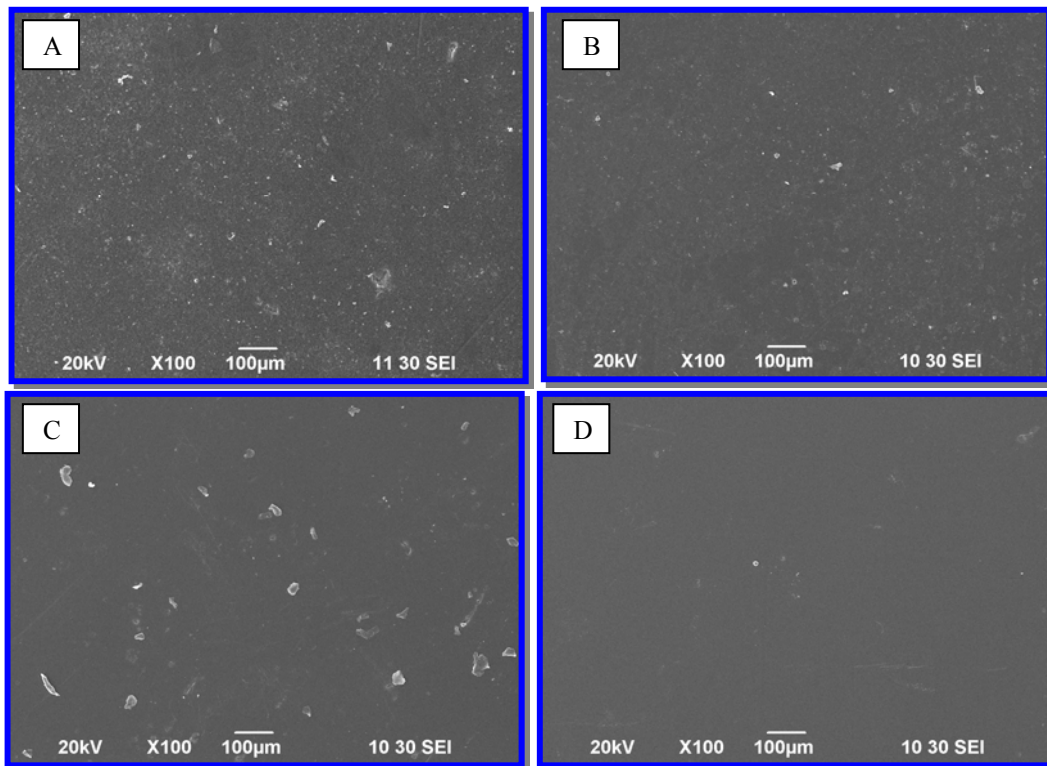


Figure 6-7 SEM of the surface of membrane. A: RAE fouled membrane; B: after 10 min water flushing; C: after 10 min US irradiation under 400 W of output power; D: after 60 min US irradiation under 400 W of output power

6.6. Chapter Summary

The sound energy must be intense enough to penetrate the housing and generate cavitation in the designed site. In most laboratories, US cleaning baths are not sufficiently powerful to achieve the requirement for cavitation bubble collapse after energy transference through housing material. To overcome this problem and to provide high power acoustic energy in crossflow system, a more effective approach

where sound energy could impinge directly on medium was then developed. Rather than immersing crossflow module into ultrasonic bath, in our study, a customized crossflow module integrated with ultrasonic transducers was fabricated and operated in stainless steel water bath. A resistance-in-series approach was adapted to evaluate the fouling profile of polysaccharides extracts. The filtration enhancement factor increased significantly from 1.15 to 1.95 with 28 KHz at 200W output comparing to previous conventional setup. With either continuous or intermitted mode of ultrasonic irradiation, DI-H₂O flux of 30 kDa PES membrane recovered to 100% after 60 min filtration with polysaccharides extract. The fouling profile of polysaccharides extract was dominated by reversible fouling taking up to 80% of total resistance. US irradiation dramatically decreased not only the reversible fouling contributed by cake layer and concentration polarization but also the irreversible fouling caused by pore blocking. The distinguished energy distribution in near field and far field in a water bath obtained by Ultrasound intensity measurements strongly supported the filtration enhancement output with integrated module. Membrane morphology characterized with SEM confirmed that no damage occurred to membrane surface after direct irradiation for one hour. Furthermore, GPC results validated that prolonged 60 min US direct irradiation didn't alternative the MW and MW distribution pattern of polysaccharides suspension.

Chapter 7. Effect of permeate spacer in US enhanced/integrated CF module

The objective of this research is to optimize the performance of US enhanced crossflow Ultrafiltration by modifying the porosity of the permeate spacers inside the CF module. Toward this purpose, a group of permeate spacer made from stainless steel was customized, validated and tested to screen the effect of porosity of permeate spacer on the US enhancement factor of CF filtration. This approach is a pioneer work in terms of developing an efficient CF filtration process enhanced by the ultrasonic irradiation combined with customized spacer.

7.1. Effect of US irradiation on support materials in water bath

In order to examine the effect of material type of permeate support on ultrasonic irradiation efficiency, aluminium foil paper was cut into identical size (4 cm × 20 cm) and then mounted onto various support embodiments including porous polypropylene (PP), Naltex spacer, aluminium plate and stainless steel plate. Ultrasonic irradiation was applied with output power of 200 W for 60 sec after the embodied subjects were vertically positioned at 3 cm away from transducer surface in a water bath. The erosions generated by ultrasonic cavitation effect on aluminium paper mounted onto different supports were demonstrated at Figure 7-1. From left to right, PP support was the least affected by cavitation while stainless steel support showed serious erosion under the same conditions. With Naltex mesh support, tiny pinpoint dots appeared on the void channel of each mesh. It was worthy pointing out that the moderate erosion occurred without any support behind the aluminium paper. This observation could be interpreted by the fundamental mechanism of acoustic

cavitation.

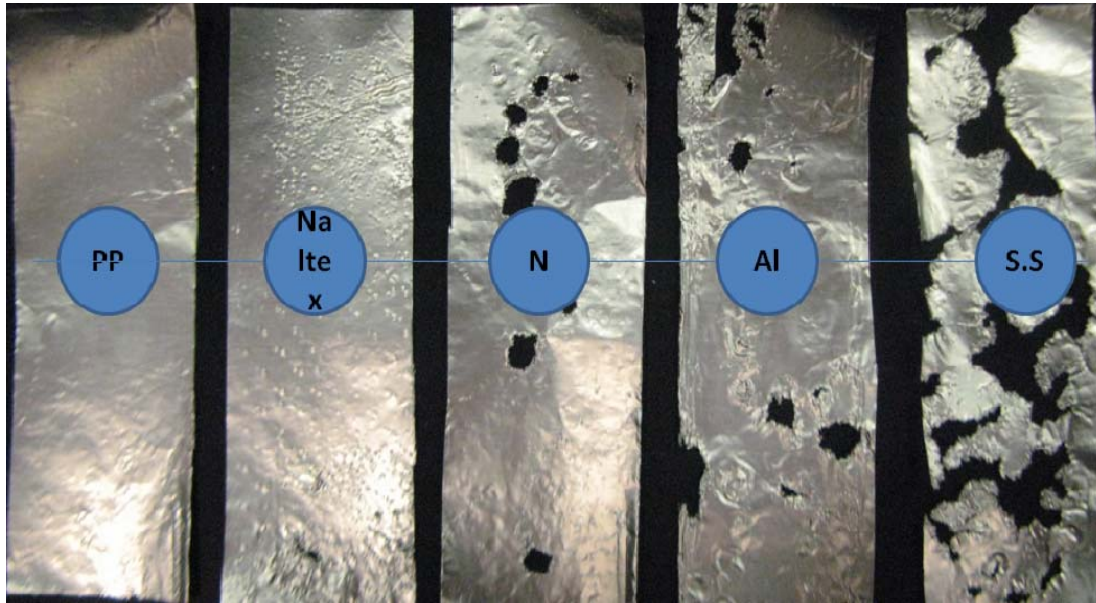


Figure 7-1 Ultrasonic cavitation effect on aluminium paper with varied support under 200 W output power for 60 sec irradiation

As acoustic pressure was proposed onto conductive fluid, the growth and oscillation of bubbles can eventually end as collapse or implosion as soon as they reach critical sizes. Extreme conditions occurred at the collapse phase, which was the surface of aluminium in this case. The propagation of waves normally involves four possible behaviours when exhibiting at the boundary of two mediums, namely reflection, diffraction, transmission and refraction [80]. Ultrasonic waves are reflected at the interface of two mediums wherever there is a difference in acoustic impedances (Z). The more difference in Z , the greater percentage of energy will be reflected at the boundary [68, 69]. The reflection coefficient of wave transmitting at the boundary of water and the support material of stainless steel is 88% and is 80% for aluminium. As for polypropylene, the density of amorphous PP is 0.855 g/cm^3 and the PP support in crossflow module has the average porosity of 75%. Thus most of the incident wave amplitude will be absorbed by the porous material, the

reflection of wave intensity dramatically decreased. Based on the finding of this test, properties of the supporting materials had strong impact on US irradiation effect. Stainless steel support exhibited dynamic advantages in reflecting and intensifying the US energy. Upon this observation, stainless steel permeate spacer would replace PP spacer for further investigation.

7.2. Effect of S.S. permeate spacer on US enhanced *RAE* Ultrafiltration

7.2.1. Effect of US irradiation on DI-H₂O flux without permeate spacer

The conventional PP permeate support was first removed from the module for both enhanced and integrated systems. Parallel filtration processes were monitored for *RAE* UF under identical experimental conditions for each setup. In order to validate how permeate flux could be compensated and how US could manipulate the flux when fluid running through without permeate support, DI-H₂O flux was recorded for 10 min interval under varied US irradiation conditions as shown in Figure 7-2. With previous PP support in permeate channel, DI-H₂O flux was comparable and consistent under TMP of 15 psi and feed velocity of 0.2 m/s comparing to manufacture standard. DI-H₂O flux was independent to the applied US output power (150±5.0 LMH) and had linear relationship with applied TMP. In the absence of permeate support, there was a channel height of 1.27 mm and PES membrane was compressed when subjecting to applied pressure. With 80 W output power of US irradiation, the water flux increased from 41.7 LMH to 51.8 LMH. As soon as the power was turned off, water flux was dropped to 40.3 LMH. With the increasing of US output power from 80 W to 400 W, the fluctuation degree of water flux induced by irradiation was relatively stable. However the deviation of DI-H₂O

flux under US condition increased dramatically. However, with original PP support, US irradiation had no impact on DI-H₂O flux regardless of the US output power.

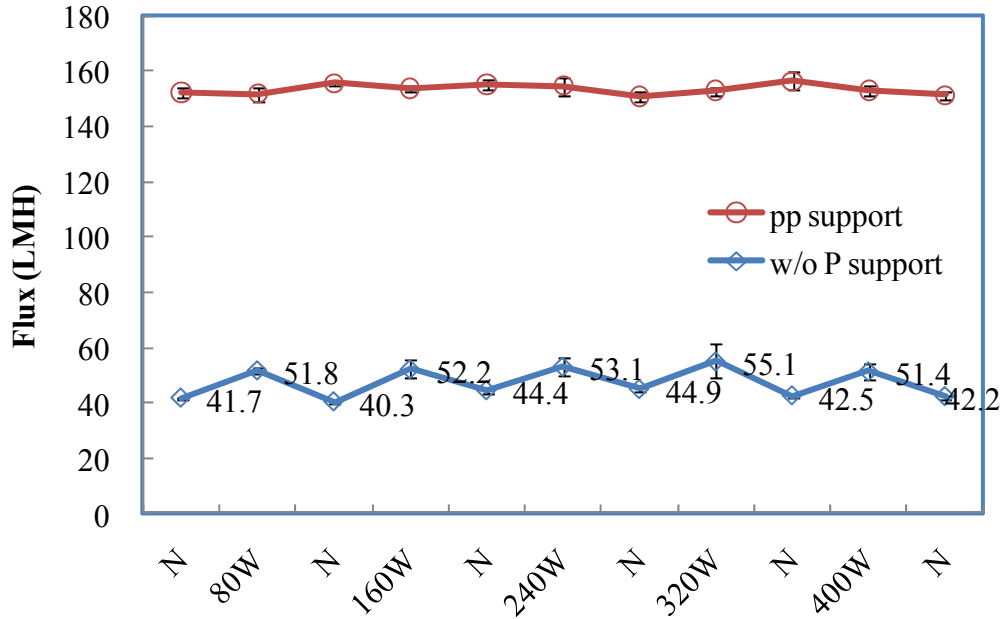


Figure 7-2 DI-H₂O flux recorded in CF system under varied US irradiation

There were two reasons to interpret the US induced DI-H₂O flux without permeate spacer. First, the function of permeate spacer in a crossflow module is to provide sufficient support to membrane from condensing or constricting when subjected to high TMP and ensure effective membrane filtration area. The pore flow model applied in Ultrafiltration adapts Hugen-Poiseuille equation to describe the flux through membrane. The model assumes that membrane has cylindered pores. In equation $J_v = \frac{\epsilon_m d_p^2 \Delta P}{32 \mu l_p}$ both membrane porosity and average pore diameter were sacrificed under constant TMP without the presence of permeate spacer. Thus the permeate flux of DI-H₂O was recorded only 30% of original value. Second, cavitation collapse in feed channel produces a number of phenomena that result in high velocity fluid movement [87]. Due to the strong reflection by stainless steel wall,

fluid travelling in the crossflow channel was subject to magnified intensity in folds. Intensified US induced effect resulted in higher velocity fluid movement. Filtration with RAE in this setup confirmed the hypotheses that almost no flux decline for the entire process.

7.2.2. Effect of permeate spacer on US enhanced RAE filtration

The function of permeate spacer in crossflow module as well as in spiral wound module is to keep adjacent membranes separate and sustain the compression when subjecting to pressure. The fact that DI-H₂O flux dropped significantly after removing PP support confirmed the durability of permeate spacer. In order to investigate the effect of permeate spacer on the permeate flux during RAE fouling. The experiments were carried out at TMP of 15 psi and feed velocity of 0.2 m/s with or without US irradiation. As displayed in Figure 7-3A, a rapid decline in RAE permeates flux from 23.6 LMH to 5.6 LMH was observed at the initial 5 min filtration, and then the flux remained relatively constant for the next following 55 min. When transducer power was turned on at the beginning of filtration, permeates flux showed vigorous variation at the first 5 min and were averaged at 20 LMH over the entire time period of operating phase. The flow instability induced by ultrasonic oscillations and mechanism induced by acoustic streaming/micro-jets had great impact on keeping the suspension particles away from membrane surface and resulting in higher permeates flux with enhancement factor of 3.35 [8]. However, when a stainless steel support with porosity of 18.5% was inserted into CF permeate channel, RAE filtration profile demonstrated different patterns comparing to those without spacers shown in Figure 7-3B. DI-H₂O flux under this condition was 97.2 LMH yet US enhancement factor decreased to 1.83 even though the absolute

permeate collection reached to 226.6 g versus 141.2 g after 60 min filtration process. In order to eliminate the calorimetrical effect generated by US output power, the temperature in water bath was controlled at 25 °C. Thus only mechanical wave energy of US could be accounted for under this circumstance. With 18.5% porosity of S.S. spacer, the total permeates collection increased to 277.9 g under 400W output power irradiation. It was interesting to compare the two intermittent operation modes, 400 W 10 min on/off and 400 W 30 min on/off, with 200 W 60 min continuous mode. Given the fact that equal US energy had been consumed for three processes, yet the enhancement factors of RAE UF were distinguished as 2.09, 1.39 and 1.83, respectively.

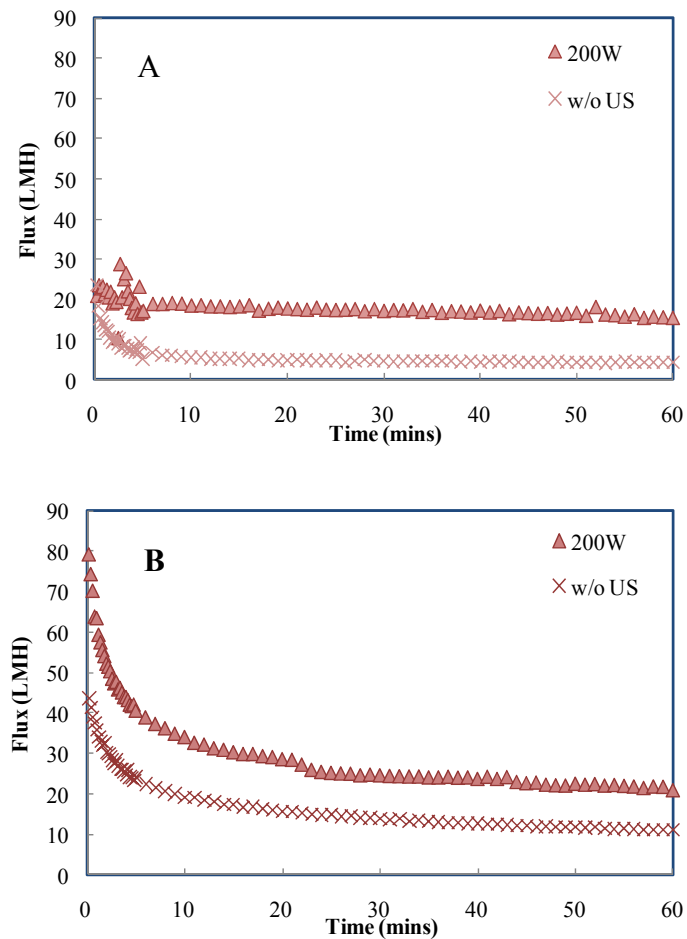


Figure 7-3 RAE filtration profile at TMP of 15 psi and Velocity of 0.2 m/s: A: Without permeate spacer; B: With S.S. permeate spacer of porosity of 18.5%

To further investigating the effect of permeate spacer on US enhanced filtration, three permeates flux, namely, DI-H₂O flux, RAE steady state flux, after flushing DI-H₂O flux, were compared under three controlled conditions including no spacer, PP spacer as well as 18.5% porosity S.S. spacer (Figure 7-4). Results showed that compensation of DI-H₂O flux due to insufficient support occurred to both no spacer case and S.S. spacer. The TMP is defined as the pressure gradient across the membrane, which normally described by the average feed pressure minus the permeate pressure. The feed pressure in our setup was only measured at the feed inlet of CF module. However, hydraulic pressure drop occurred in flowing pipes due to friction, vertical pipe difference as well as change of kinetic energy. Pressure loss along the membrane surface inside the feed channel was the function of friction coefficient, Reynolds number, and feed velocity [112]. Without the proper support of permeate spacer, the instability of flow induced higher friction coefficient as well as localized turbulent flow might be the reasons for significant pressure loss. In the contrast, under the irradiation of US, these reasons turned into positive driving forces for enhanced permeate flux. Even though, the DI-H₂O flux was only 65% of original value, the US enhanced RAE flux with S.S. spacer with porosity of 18.5% was comparable to those with PP support (22.4 LMH vs. 22.3 LMH).

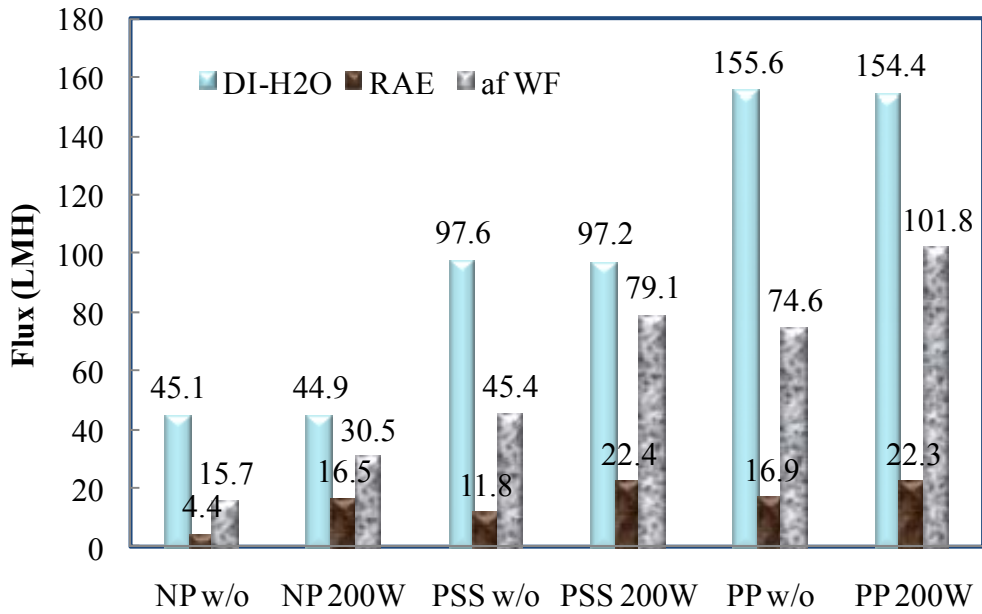


Figure 7-4 The effect of permeate spacer on US enhanced filtration, comparison of DI-H₂O flux, RAE steady state flux and after flushing DI-H₂O flux

7.2.3. Effect of the porosity of S.S. permeate spacer on DI-H₂O flux compensation and permeate support resistance

Six sets of stainless steel (S.S.) permeate spacers were inserted into crossflow module to evaluate the effect of porosity on DI-H₂O flux. As displayed in Figure 7-5, from left to right, the porosity of six spacers were 18.5%, 35.9%, 46.2%, 62.0%, 69.3% and 78.0% and the corner images represented two geometric shapes of spacers cultivated by photo chemical milling process. All spacers had equal thickness of 1.2 mm fitting into the permeate channel.

For the first step of the experiments, the retentate valve was closed to establish a dead end system for calculating the membrane resistance for each setup. TMP were set to be starting from 5 psi and ending at 22.5 psi to study the relationship between TMP and DI-H₂O flux with varied permeate spacers. During 10 min period, the weight of permeate was measured every 30 s. After applying the resistance in series

model, R_m (membrane intrinsic resistance) and R_s (resistance generated by support) were calculated and showed in Table 7-1. The S.S. permeate spacer with porosity of 62% exhibited the similar DI-H₂O flux at TMP of 15 psi as well as the lowest resistance generated by this support.

Table 7-1 The resistance generated by the S.S permeate support as the function of support porosity

Porosity of permeate support	Jw@ $\Delta P=15$ psi (LMH)	Resistance R_m+R_s	R_s	Jw vs. ΔP
PP support	155.2	4.00E+09		$y = 10.333x$ $R^2 = 0.9962$
18.5%	97.6	6.36E+09	2.39E+09	
35.9%	127.0	4.88E+09	8.28E+08	$y = 7.0338x + 19.209$ $R^2 = 0.9972$
46.2%	150.5	4.12E+09	1.20E+08	$y = 9.5615x + 6.2519$ $R^2 = 0.999$
62.0%	154.2	4.02E+09	2.08E+07	$y = 10.773x$ $R^2 = 0.9934$
69.3%	135.3	4.59E+09	5.83E+08	$y = 9.2595x + 0.305$ $R^2 = 0.9922$
78.0%	120.6	5.15E+09	1.14E+09	$y = 8.1792x + 1.3692$ $R^2 = 0.9905$

Even though all permeate support demonstrated the linear relationship between the permeate flux with TMP, the various slope as well as intersection value revealed that degree of dependency of permeate flux on TMP was significantly affected by the porosity of permeate support. As DI-H₂O flux at various TMP was plotted against support porosity, shown in Figure 7-6, the figure of flux corresponded perfectly with a second degree polynomial equation ($y = -952.08x^2 + 1031.3x - 121.17$) at particular TMP of 15 psi. The contact area between membrane and the S.S. spacer in CF module played important role in determining the maximum permeate flux under certain TMP. A recent study developed a finite element model to describe the how pressure drop varied along crossflow channel for different spacer configurations [51]. Although computational fluid dynamic (CFD) method was adopted to precisely

simulate the pressure, flow and concentration profile in crossflow channel regarding the feed spacer, it was of particular interest to predict that pressure drop and flow distortion could occur when the permeate spacer was untenable to provide sufficient support. Moreover, the permeate spacer constructs a draining system for fluid to pass by. Due to the barrier between the spacer and fluid, a counter pressure may be generated to limit the flux through the membrane [113].

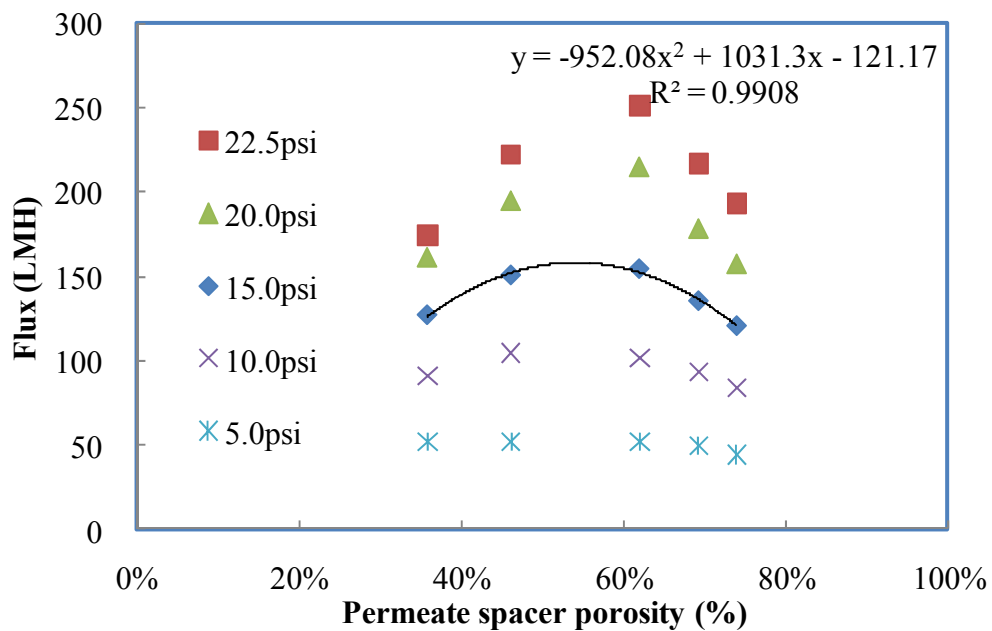


Figure 7-5 DI-H₂O flux vs porosity of S.S. permeate support at various TMP

7.2.4. Effect of the porosity of S.S. permeate spacer on flux enhancement in US enhanced CF filtration process

Six sets of stainless steel (S.S.) permeate spacers were inserted into crossflow module to evaluate the effect of porosity on RAE filtration enhancement when irradiating with ultrasound in a water bath. After each DI-H₂O test, RAE was running through the crossflow module to evaluate the effect of porosity on US enhanced RAE filtration in a water bath. Common simulation conditions used were feed velocity of 0.2 m/s and TMP of 15 psi, and US output power of 200 W. For each permeate

spacer, control experiment was conducted under same conditions without US irradiation. The effects of permeate spacer on US enhanced filtration were given in Figure 7-7. As it can be seen, the dotted line presented the degree of DI-H₂O flux loss decreased with the increasing of spacer porosity in the range from 18.5% to 62.0%. It was expected that total permeate collection of RAE filtration without US treatment increased from 125.92 g to 198.04 g as the DI-H₂O flux with spacer porosity of 62% tended to close to membrane's original value. However, total permeate collection with US treatment showed no clear tendency as spacer porosity increased. Comparing to PP spacer, the absolute permeate collections improvement contributed by US effect were insignificant for all S.S spacers. The reason for this kind of behaviour can be found in chapter 5 that there was no cavitation bubble collapse inside the crossflow channel due to the limitation of US intensity transporting through stainless steel housing. The associated effect induced by acoustic streaming and micro-jets were apparently compensated by extra resistance generated by the interaction between membrane and S.S. spacer. It was worthy pointing out that relative filtration enhancement factors EF decreased with the increase of spacer porosity. To rephrase this statement, the larger contact area between membrane the S.S. plate under US field could generate greater acoustic streaming effect. The motion of acoustic streaming can continuously migrate those suspended particles away from membrane surface [86], thus resulted in improved filtration efficiency regardless of the extra resistance. To summarize, by simply replacing the PP spacer with S.S spacer in permeate channel, the RAE filtration enhancement factor increased 28% more in US enhanced system.

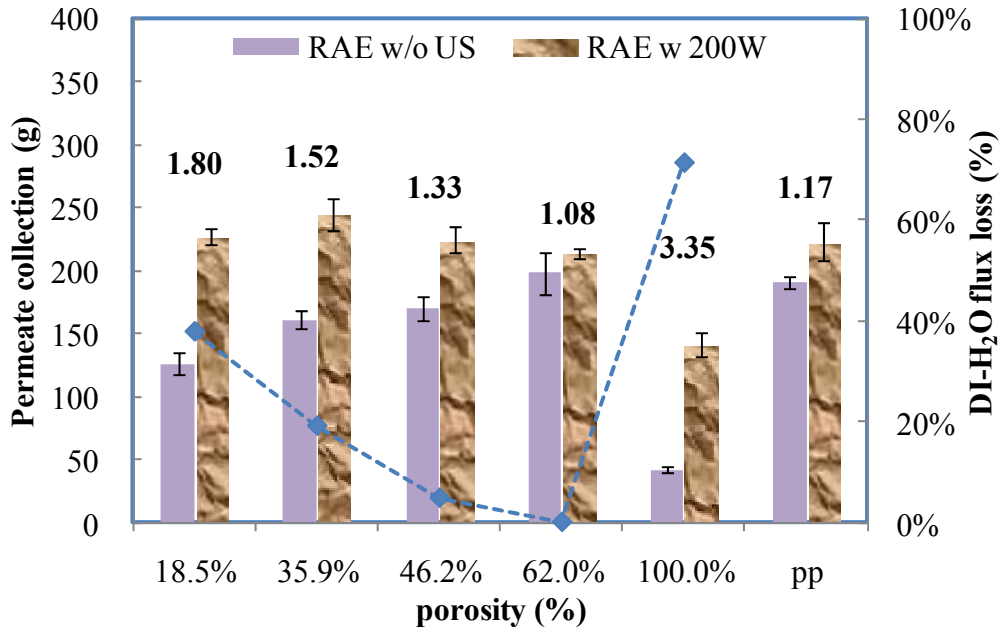


Figure 7-6 Effect of spacer porosity on US enhanced system

7.3. Effect of the porosity of S.S. permeate spacer on flux enhancement in US Integrated CF filtration process

Same experimental protocol was applied in US integrated CF filtration process to evaluate the effect of spacer porosity on US enhanced RAE filtration improvement. After each DI-H₂O test, RAE was running through the crossflow under the experimental conditions of feed velocity of 0.2 m/s, TMP of 15 psi, and US output power of 80 W. For each permeate spacer, control experiment was conducted under same conditions without US irradiation. The effects of permeate spacer on US integrated filtration plotted against total permeate collection were presented in Figure 7-8. In contrast to previous module, the results exhibited completely different tendency for both absolute permeate collection and relative enhancement factor as spacer porosity increased from 18.5% to 78.0%. Absolute permeate collection with new spacer was increasing when spacer porosity increased from 18.5% to 69.3% then started to decline. The spacer with porosity of 46.2% in CF permeate channel

gave equivalent DI-H₂O flux and permeate collection in compare to PP spacer. As we stated in chapter 6, the mechanisms of ultrasound effect in integrated CF was distinguished and more complex than those in enhanced system. Within the near field zone of US transducer, numerous bubbles and consequent collapse would generate on or near the solid-liquid interfaces. Rather than only acoustic streaming inside the liquid as well as micro-jets at liquid-solid interface, the sudden collapse of cavitation bubbles promoted flow instability in filtration channel and accelerated mass transport though membrane. With S.S. spacer, the amplitude wave can transmit and reflect between the transducer surface and S.S. plate. Thus the overall US effect could be magnified dramatically to overcome the interaction resistance between membrane and S.S. plate. However, with the continue increasing of porosity, the support function of permeate spacer was insufficient. Consequently, phenomena of the distortion of membrane surface and the agitation in flow might deteriorate the filtration process under higher spacer porosity, such as 78.0%. With proper choice of porosity of S.S spacer, the maximum improvement of filtration efficiency can reach 45% more in compare to PP spacer in US integrated system.

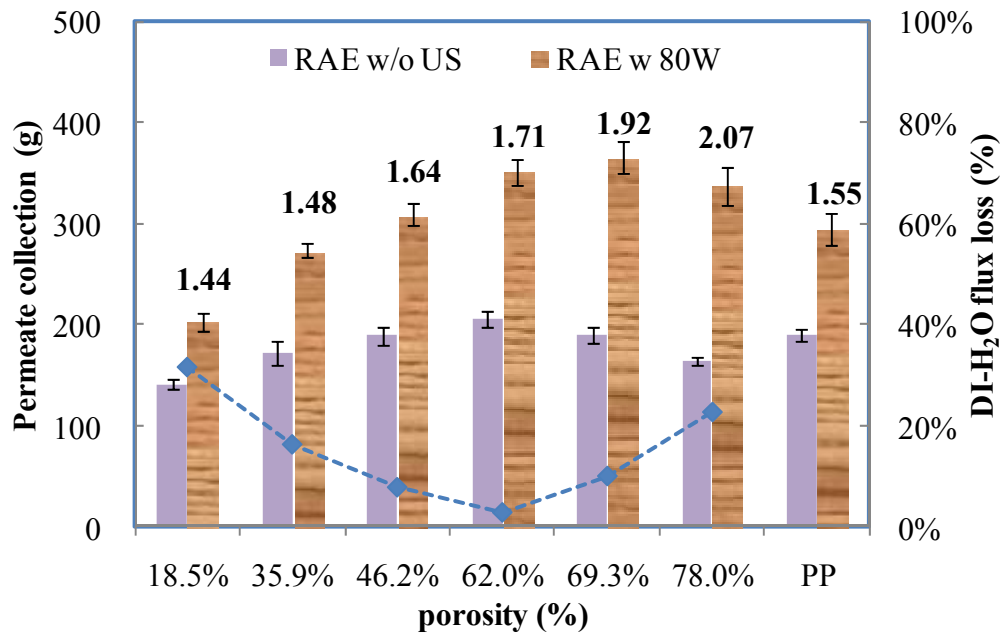


Figure 7-7 Effect of spacer porosity on US integrated system

Moreover, when the two groups of relative enhancement factors were plotted against spacer porosity as shown in Figure 7-9, two crosscurrent trendlines were formed. In contrast to the situation in US enhanced system, relative EF in US integrated system showed a steady increase with the increase of spacer porosity. In this case, the void area between the membrane and S.S. spacer became critical. The observation could be interpreted by the feature bubble motion near the radiating surface. It is believed that [89] the migration of the bubbles is driven by the Bjerkness force existing between pulsating bubbles in a pressure field [89]. With proper sonotrode diameter, dramatic fluid turbulence could form when microstreamers detaching from radiating surface [109]. Higher support resistance generated by lower porosity S.S. spacer tended to be repulsive to this force. Thus, the overall US induced effect in transducer near zone could be altered indirectly by the feature of membrane supports.

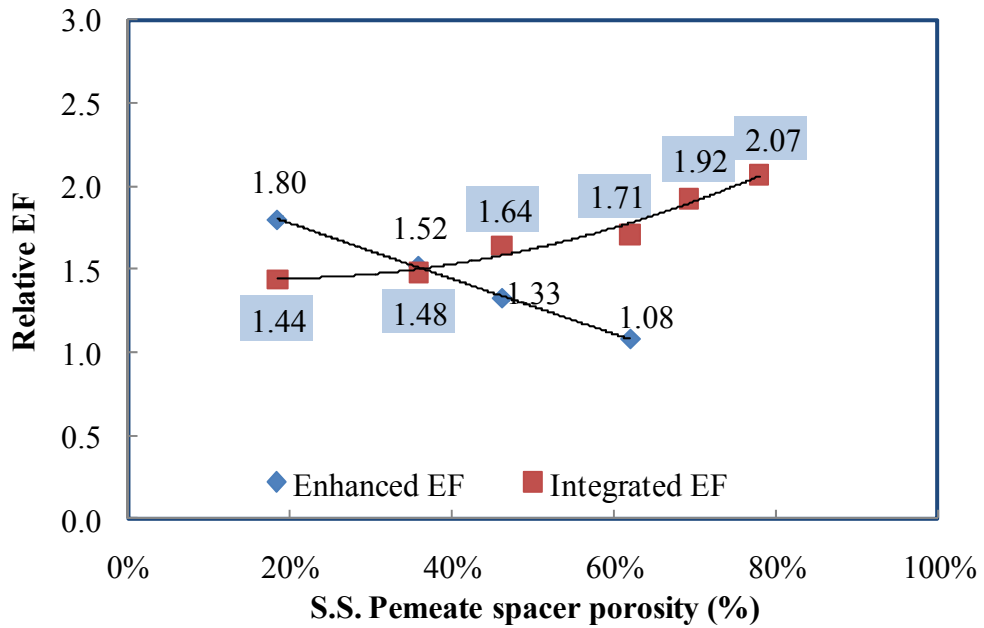


Figure 7-8 Effect of spacer porosity on relative filtration enhancement factors in two systems.

7.4. Chapter Summary

Dramatic loss of ultrasound intensity when propagating through the membrane housing materials represents the main obstacle to more extensive practical application of US in crossflow membrane filtration processes. To overcome this problem and to provide sufficient acoustic energy in crossflow system, a more effective US integrated CF system where sound energy could impinge directly on medium was then developed. In order to further increase the filtration efficiency, six sets of stainless steel (S.S.) permeate spacers were inserted into crossflow module to evaluate the effect of porosity on permeate flux as well as on RAE filtration enhancement when irradiating with ultrasound in both US enhanced and US integrated system.

An extreme condition of taking spacer out of the module was first analyzed. DI-H₂O flux dropped to 45.1 LMH comparing to manufacture value of 150 LMH

under same conditions. While the RAE filtration enhancement factor improved by 3.5 folds. Without proper support to membrane, the flow induced higher friction coefficient as well as localized turbulent became reasons for significant DI-H₂O flux loss. In the contrast, under the irradiation of US, these reasons turned into positive driving forces for enhanced permeate. The S.S. permeate spacer with porosity of 62% exhibited the similar DI-H₂O flux at TMP of 15 psi as well as the lowest resistance generated by this support.

The trade off between the water flux and filtration enhancement urged us to further modify permeate spacer for application. The relative RAE filtration enhancement factors presented completely contrary tendencies for two CF systems when plotting as the function of spacer porosity. The different US induced mechanisms could be the answers. In enhanced module, the smaller porosity, the larger contact area between membrane and the S.S., the greater filtration enhancement. That means the stronger wave reflection could intensify those associated effect induced by acoustic streaming and microstreaming. On the other hand, in integrated module, the intensified acoustic cavitation and micro-jet required large the free tension area between the membrane and S.S. spacer for solute passing through and the mass transfer could be accelerated with cavitation and micro-jets effect.

The replacement of original propylene spacer with S.S. spacer dramatically magnified the ultrasound irradiation intensity and improved US induced effect. The porosity of S.S spacer as well as the corresponding contact area between membrane the S.S. spacer can tailor the US effect to achieve significant permeate collection. It was reasonable to predicate that there was a range of moderate spacer porosity for which the flux enhancement will be maximized in US integrated system.

Chapter 8. RSM & optimization of permeate spacer porosity in US integrated system

Response surface methodology (RSM) has been applied successfully in various scientific and technical fields such as applied chemistry and physics, biochemistry and biology, chemical engineering, environmental protection. Particularly In membrane science and technology, the significant value of experimental design and optimization methodology has been reviewed from the angels of theoretical concepts as well as process control applications [114-120]. RSM applies mathematical and statistical techniques for developing, improving, and optimizing processes and can be used to evaluate the relative significance of affecting factors [121]. Normally three topics will be combined into RSM: design of experiment, regression modelling techniques and optimization methods. Design of experiment involves incorporating all controllable factors that can alter the results and identifying the most significant ones. Thus the number of experiments can be reduced to lower the material and energy consumption. Furthermore, proper experimental design can develop mathematical models and evaluate the influence of individual factors as well as interaction effects between the factors [122].

Box-Behnken design are a class of rotatable or nearly rotatable second-order designs and construct by combining two-level factorial designs with incomplete block designs, and have complex confounding of interaction [122]. The advantages of Box-Behnken design (BBD) comparing to other response surface designs such as central composite (CCD), Doehler matrix (DMD) and three level full factorial design (TLFFD) are summarized in Ferreira's work. BBD requires fewer number of experiments than CCD and process higher experimental efficiency as the number of factors are bigger than 3. By avoiding the corners of the design space, BBD allow

experimenters to work around extreme factor combinations. Jokic et al. [123] studied the influence of static mixer as turbulence promoter on the microfiltration of baker's yeast and applied Box–Behnken design method to evaluate the most significant factor. Malaisamy et al. [124] adopted the Box–Behnken design method and the analysis of variance to the purification of vitamin B₂ with Polysulfone membranes. The experimental separation factors were in good correlation with the predicted values generated by second order polynomial regression model.

In the present work, Box–Behnken design of experiments coupled with response surface methodology were employed to investigate the effects of control variables (ultrasound output power, porosity of permeate spacer and transmembrane pressure) on the absolute permeate collection for RAE Ultrafiltration in US integrated CF system.

8.1. Experimental protocol

The statistical design of experiments is a structural and systematized approach to incorporating most important factors into the process. After screening all controllable factors that may influence the experiment, three factors namely, the ultrasound output power (X_1), the porosity of permeate spacer (X_2) and transmembrane pressure (X_3) were selected. The DI-H₂O flux was obtained with fresh membrane after conditioning it for 30 min under same hydrodynamic condition. The absolute RAE permeate collection was measured exactly from the moment as feed fluid stream entered the crossflow module and US power was turned on. All measurements in this study were carried out in triplicate and the results averaged. The deviation between parallel experimental runs fell in the range of $\pm 5\%$.

Box-Behnken design was applied. The number of experiments (n) required generating quadratic equation which can correlate the factors and response was

$$n = 2\kappa(\kappa - 1) + C \quad (8-1)$$

where κ is the total number of independent variables and C is the number of replicates at the centre point. For the design with three factors and three replicates at the centre point, 15 experiments were performed. Table 8-1 summarized the independent variables and their actual values and the two responses: DI-H₂O flux compensation ratio (Y₁) and absolute permeate collection (Y₂). DI-H₂O flux compensation ratio (CR_w) was calculated as

$$CR_w = \frac{J_{wpp} - J_{wss}}{J_{wpp}} 100 \quad (8-2)$$

Where J_{wpp} and J_{wss} represented DI-H₂O flux obtained in crossflow unit with nascent propylene spacer and stainless steel spacer under identical applied TMP and feed velocity, respectively.

Table 8-1 Box-Behnken design (BBD) for modified S.S. permeate spacer in US integrated filtration system

Standard Run	Factors			Responses	
	X ₁ US output power (W)	X ₂ Porosity of permeate spacer (%)	X ₃ TMP (psi)	Y ₁ DI-H ₂ O compensation (%)	Y ₂ Absolute permeate collection (g)
1	40	46.2%	15	9.88%	243.64
2	120	46.2%	15	10.23%	338.82
3	40	78.0%	15	25.38%	291.55
4	120	78.0%	15	24.69%	370.39
5	40	62.0%	10	5.98%	240.91
6	120	62.0%	10	6.12%	325.82
7	40	62.0%	20	0.21%	328.06
8	120	62.0%	20	3.87%	407.38
9	80	46.2%	10	7.23%	252.56
10	80	78.0%	10	29.88%	269.44
11	80	46.2%	20	9.50%	326.41
12	80	78.0%	20	21.99%	356.30
13	80	62.0%	15	3.96%	363.24
14	80	62.0%	15	4.58%	351.45
15	80	62.0%	15	3.55%	344.98

Based on the responses obtained from designed experiments, a second degree polynomial model was established to characterize and quantify the effects of each factor and the interaction effects between factors:

$$Y = b_0 + \sum_{i=1}^n b_i \chi_i + \sum_{i=1}^n b_{ii} \chi_i^2 + \sum_{i < j}^n b_{ij} \chi_i \chi_j \quad (8-3)$$

Where Y represented the predicted response of the process, χ_i was the studied factors, b_0 the intercept (constant), b_i the linear, b_{ii} the quadratic and b_{ij} the interaction effect of the factors.

8.2. Analysis

According to the experimental design the full quadratic models were established by response surface regression models with Statistica 10 software. In our case (n=3 input variables), the empirical model in terms of coded factors can be depicted as

$$Y = b_0 + b_1 \chi_1 + b_2 \chi_2 + b_3 \chi_3 + b_{11} \chi_1^2 + b_{22} \chi_2^2 + b_{33} \chi_3^2 + b_{12} \chi_1 \chi_2 + b_{13} \chi_1 \chi_3 + b_{23} \chi_2 \chi_3 \quad (8-4)$$

Based on the experimental design results shown in Table 8-1, the RSM has been applied to develop the polynomial regression equations to interpret the relation between independent variables and output responses. The results of the statistical analysis through general multiple regression based on experimental design were presented in Table 8-2. The coefficients were related to actual variables.

Table 8-2 Regression equation coefficients for responses and model validation

Effects	Y ₁		Y ₂	
	Coefficient	p-value	Coefficient	p-value
Intercept				
b ₀	1.49696	0.00019***	-631.98915	0.01430***
Linear				
b ₁	0.00034	0.74943	2.44755	0.01341***
b ₂	-5.67522	0.00016***	1727.44469	0.00062***
b ₃	0.02189	0.07070**	28.82287	0.00553***
Quadratic				
b ₁₁	-0.00022	0.98039	-0.00555	0.08813**
b ₂₂	5.39313	0.00005***	1318.96439	0.00051***
b ₃₃	-0.00023	0.42403	-0.75207	0.00654***
interaction				
b ₁₂	-0.00041	0.69316	-0.64107	0.35860
b ₁₃	0.00001	0.84315	-0.00699	0.74316
b ₂₃	-0.03190	0.09696**	4.08320	0.45760

Y₁, DI-H₂O flux compensation; Y₂, absolute permeate collection; 1-US output power; 2-Porosity of permeate spacer; 3-TMP

* Effects are statistically significant, p≤0.15

** Effects are statistically significant, p≤0.10

***Effects are statistically significant, p≤0.05

The ANOVA results were displayed in Table 8-3 for modelled responses. Relatively high values of R² obtained for the two responses indicated good fit of experimental data to Eq. All polynomial models were significant at 95% confidence level (p-value; 0.05).

The goodness of model fit was evaluated by the determination coefficient, which for the response of DI-H₂O flux compensation was 0.9833. The value indicated that less than 2% of the variations could not be interpreted by the model. As for significance of the coefficients, p-values indicated that the most influential factor was the porosity of permeate spacer, both linear and quadratic effects. Among linear factors TMP was significant at the level 0.10, while US output power was insignificant for the response of DI-H₂O compensation (Table 8-2). The mutual interaction between porosity and TMP was also significant at the level 0.10. It was desirable only in the case that increase in permeate collection was high enough to compensate for the loss of DI-H₂O flux.

The ANOVA of the quadratic regression for absolute permeate collection model indicated the model to be significant (Table 8-3). R^2 was 0.997 which implied that less than 1% of the variations could not be explained by the model. Regression equation coefficients for responses and model validation results (Table 8-2) confirmed the significance of the coefficients. The p-values revealed that the all linear and quadratic effects of three independent variables were influential factors for response of absolute permeates collection. While neither interaction of any two of three variables was significant.

Table 8-3 Analysis of variance (ANOVA) of the modelled responses

Dependant Variable	Residual			Model				
	DF	SS	MS	DF	SS	MS	F-value	p-value
Y ₁	5	0.0008	0.00216	9	0.13	0.014	95.5127	0.000511
Y ₂	5	325.5713	65.11426	9	35135.41	3903.934	59.9551	0.000147
	Multiple R	Multiple R ²	Adjusted R ²					
Y ₁	0.9970	0.9940	0.9833					
Y ₂	0.9953	0.9908	0.9743					

The response values determined by empirical models were compared to the experimental data in Table 8-1. Figure 8-1 demonstrated the parity plot of the observed and predicted values for modelled response. As can be seen, the response models show good fits to the experimental data. Therefore, the models can be considered adequate for the predication and optimization.

Therefore, the regression equations in terms of coded factors extracted from Eq. 8-4 for DI-H₂O compensation (Y₁) and permeate collection (Y₂) were:

$$Y = 1.497 - 5.675\chi_2 + 0.022\chi_3 + 5.393\chi_2^2 - 0.032\chi_2\chi_3$$

$$Y = -631.989 + 2.448\chi_1 + 1727.445\chi_2 + 28.823\chi_3 - 0.006\chi_1^2 + 1318.964\chi_2^2 - 0.752\chi_3^2$$

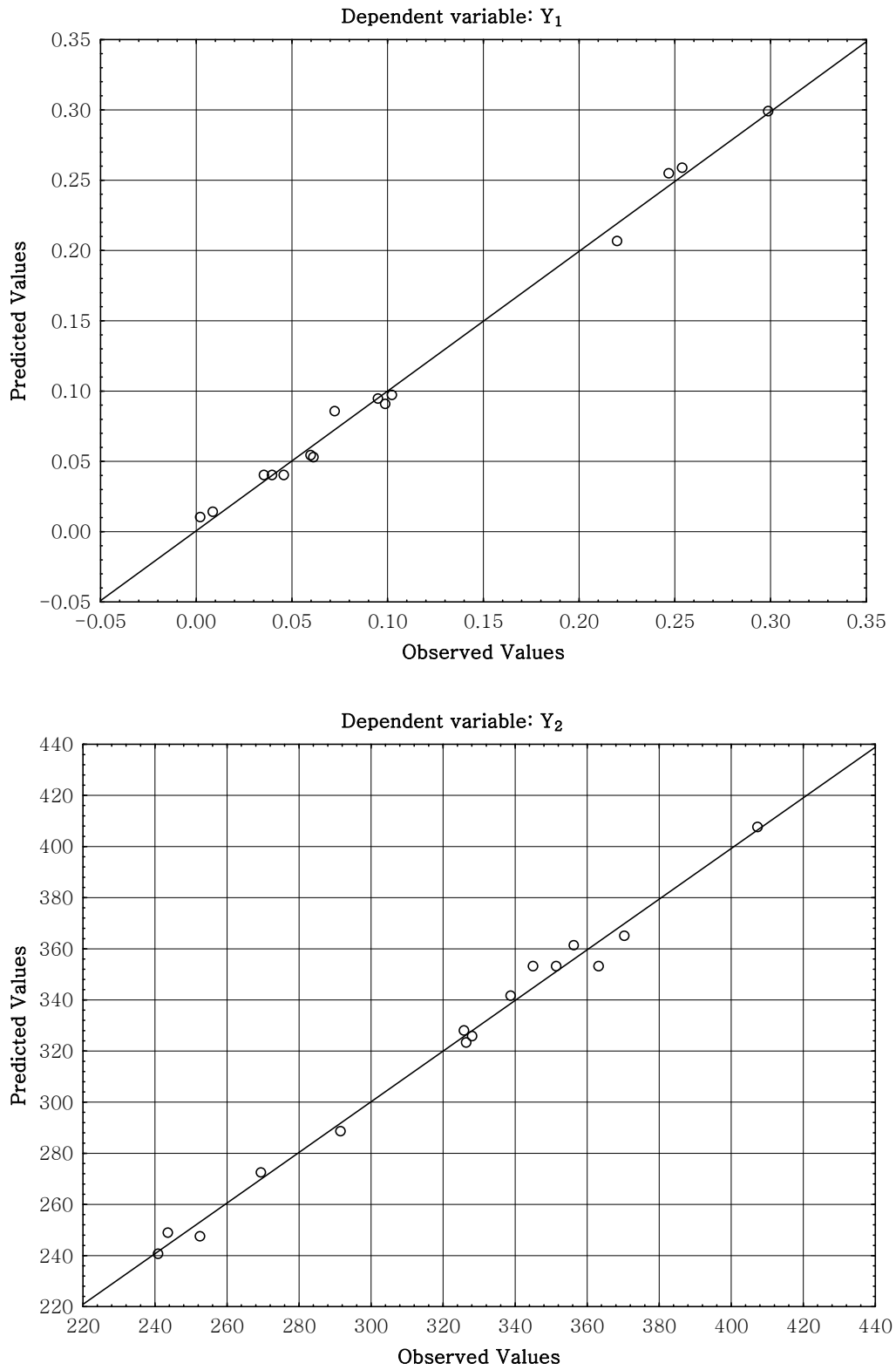


Figure 8-1 Observed values compared to the predicted values given by the two response surface models

8.3. Pareto chart

The linear, quadratic and cross-effects of each independent variable displayed in Pareto chart were given in Figure 8-2. Variances were shown in their descending order to identify which variable had the greatest cumulative effect on responses. The lengths of the bars on the chart were proportional to absolute values of the estimated effects and clearly represented the importance of defined variables. The effect would be significant as long as its corresponding bar extended beyond the boundary line at $p=0.05$ level. It could be interpreted that the quadratic term of porosity of permeate spacer (X_2^2) was the most important variables on DI-H₂O compensation (Y_1), followed by the linear term of X_2 and TMP (X_3) as well as the cross term of X_2X_3 on Y_1 . On the other hand, for response of permeate collection (Y_2), the most valuable effect was contributed by the linear term of US output power (X_1), followed by X_3 , X_2^2 and X_2 .

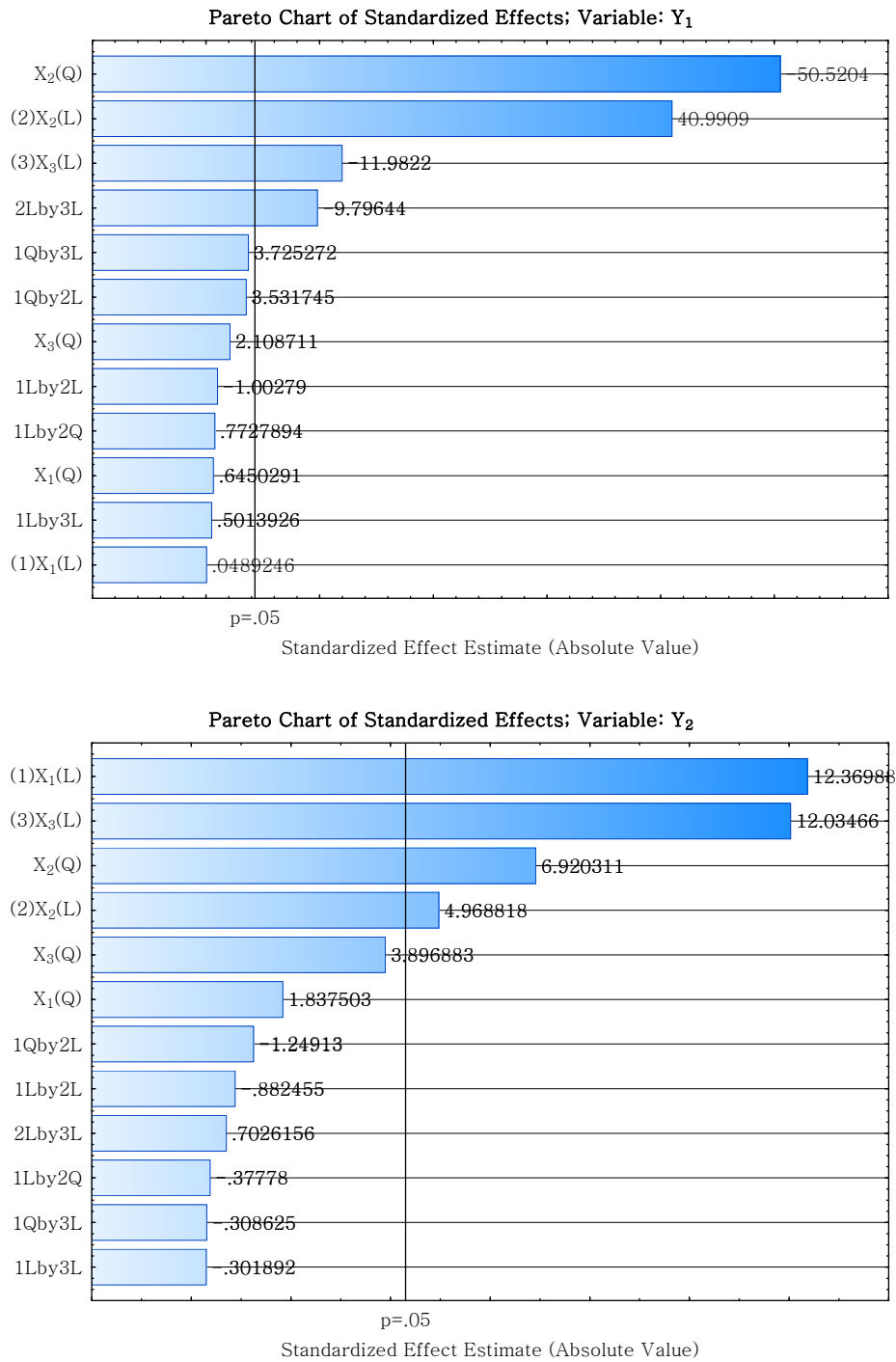


Figure 8-2 The linear, quadratic and cross-effects of each independent variable displayed in Pareto chart

8.4. Response surface and contour plots of effects on responses

8.4.1. Response surface and contour plots of three variables on DI-H₂O compensation

The effects of independent variables and their mutual interaction on the responses can be illustrated by response surface and contour plots. The effects of US output power and porosity of permeate spacer on DI-H₂O compensation were given in Figure 8-3A. The value of response was independent of the increase of US output power, yet strongly affected by the porosity of permeate spacer. The average porosity of the original polypropylene (PP) spacer was 75% which provided sufficient support to the membrane to sustain nascent permeability. Initial increase in permeate porosity resulted in the decrease of DI-H₂O flux compensation up to 62% of porosity; further increase of permeate porosity led to increased compensation in DI-H₂O flux at all applied TMP.

The effects of TMP and porosity of permeate spacer on DI-H₂O flux compensation were given in Figure 8-3B. At lower porosity the increase of DI-H₂O flux compensation was moderate when TMP increased. The reason behind this phenomenon could be explained by Hugen-Poiseuille equation that at very lower porosity both membrane porosity and average pore diameter were diminished, thus the flux compensation could be higher. By applying TMP of 15 psi with permeate spacer porosity of 18.5%, the flux loss was 31.7% and then declined to 16.3% when spacer porosity increased to 35.9%. Extensively, the flux loss continued to decline to minimum value until the porosity reached to 62%. Afterwards, the flux loss started to climb up with the increasing of spacer porosity. The interaction between the membrane and the S.S. spacer generated more resistance against the TMP and resulted in lower permeate flux. On the other hand, the effect of TMP on flux loss became significant at relatively higher porosity of permeate spacer.

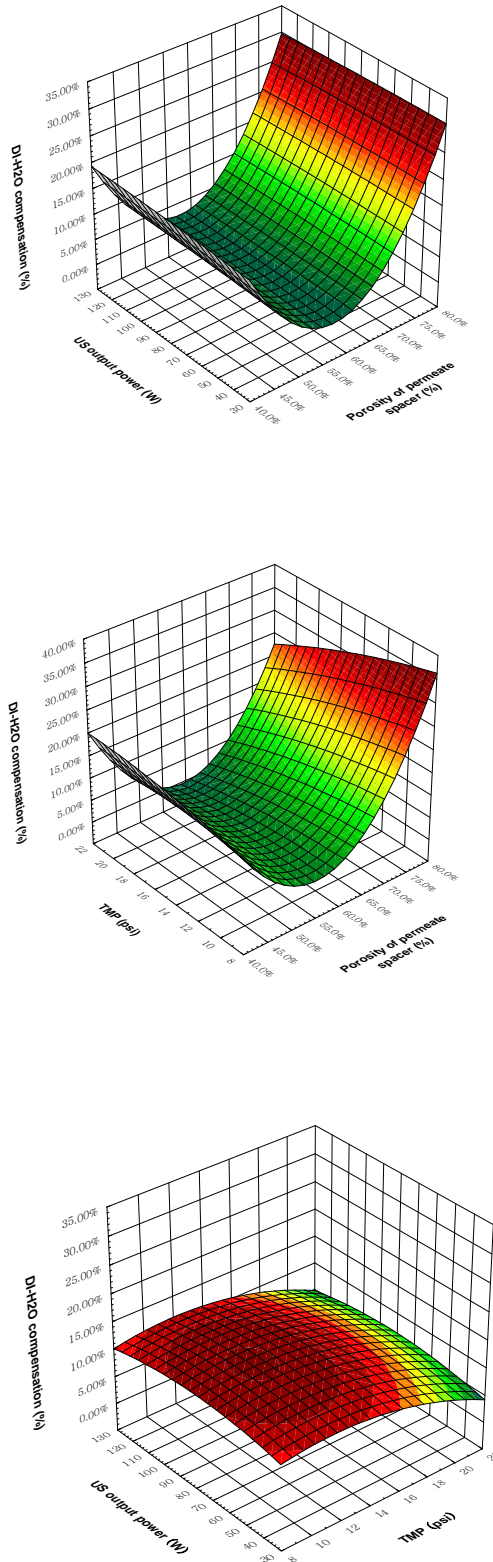


Figure 8-3 Response surface and contour plots of three variables on DI-H₂O compensation

The effects of TMP and US output power on DI-H₂O flux compensation were given in Figure 8-3C. As it could be expected that the increase of US output had no effect on DI-H₂O flux, while the increase of TMP did cause slightly more DI-H₂O flux loss until TMP was reached to 15 psi. With continuing increase of TMP, DI-H₂O flux loss started to decline. Under the support of nascent PP spacer, DI-H₂O flux was linearly proportional to applied TMP. The complex reasons behind the effect of TMP on flux loss with variable porosity of S.S. spacer might be attributed to unstable turbulence along the channel.

8.4.2. Response surface and contour plots of three variables on permeate collection

The effects of TMP and US output power on absolute permeate collection were given in Figure 8-4A. In contrast to the effects of these two factors to DI-H₂O compensation in which US output power had no effect and TMP had very moderate influence, increase of permeate collection was more vigorous with the increase of both TMP and US power. The result was consistent with our previous finding for either US enhanced system or US integrated system. In US enhanced system the increasing of cake layer thickness compromised the increasing of TMP, which was associated with bulk transport model where the migration of particles toward the membrane was balanced by the back-transport toward the bulk flow. Moreover, as concentration polarization was a result of the building up of concentration gradient of solutes near the membrane surface, the higher TMP was expected to lead to a higher osmotic pressure due to the accumulation and compaction of the fouling layer. Therefore, there was a critical pressure exist in this polynomial relationship between total permeate collection and TMP. Beyond the critical point, the collection would start to decline with the increasing of TMP.

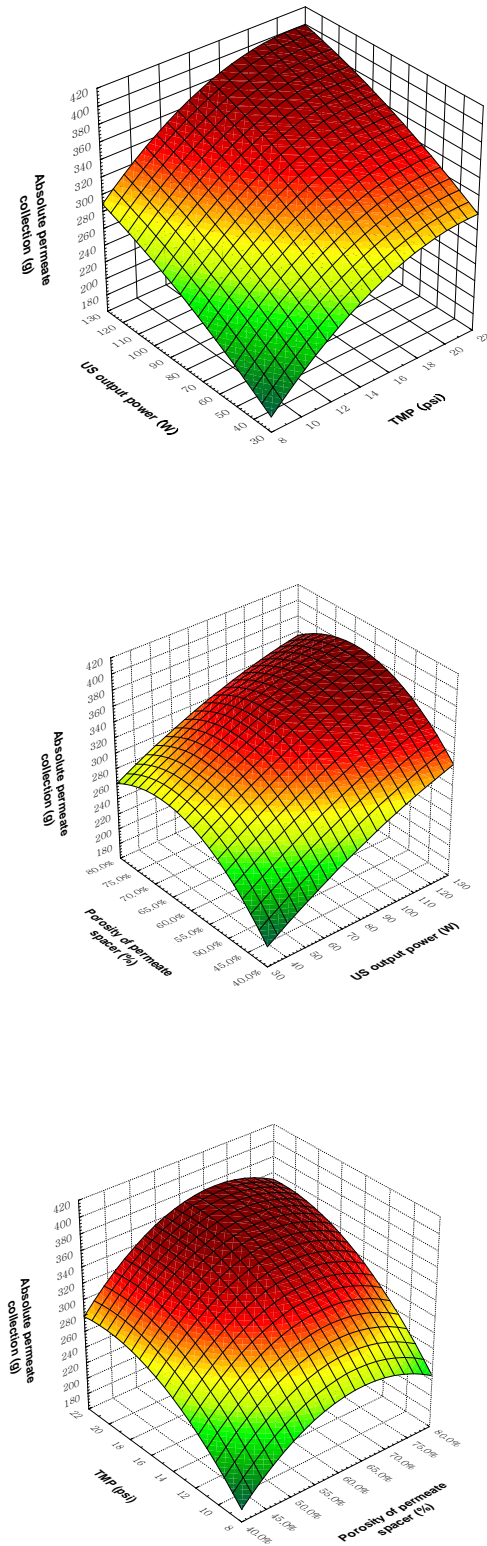


Figure 8-4 Response surface and contour plots of three variables on permeate collection

The effects of porosity and US output power on absolute permeate collection were given in Figure 8-4B. The increase of US output power would eventually generate more turbulence and increase the shear rate at the membrane surface, thus reduced the cake layer build-up for more efficient filtration process

The effects of porosity and TMP on absolute permeate collection were given in Figure 8-4C. As we stated in chapter 6, it could be expected that the increase of spacer porosity initially resulted in the increase of permeate collection until the appropriate porosity of permeate spacer was reached. Beyond the critical point of spacer porosity, permeate collection in US integrated system would decrease due to insufficient membrane support.

8.5. Optimization: desirability function approach

The objective of experiment design and analysis was the process optimization. Thus, the developed models can be used for simulation and optimization. In a process with two or more output responses, desirability function is one of most widely used approaches for the optimization procedures in versatile fields of applied science and engineering [121, 123, 125, 126]. Desirability function-based approach is the process to convert the predicated response second order models into individual desirability functions, and then combine multiple responses into one composite function [127]. This approach involves assigning the individual desirability function for each response to the predicted values ranging from 0 (very undesirable) to 1 (very desirable). A review [127] categorized current desirability function-based methods into two groups of different statistical sophistication levels, the less sophisticated ones and the more sophisticated ones. Derringer and Suich [128] proposed one less

sophisticated method which had been proved to be more flexible and easily implemented. Therefore, it is our goal to apply Derringer and Suich desirability function approach to discover the optimal point desirable for both higher permeate collection and lower flux compensation.

According to this approach, each estimated response Y_i is initially transformed to an individual desirability function (d_i) falling in the range $0 \leq d_i \leq 1$. The value of individual desirability will be increasing with the increase of desirability of the corresponding responses. The individual desirability are then combined based on a geometric mean and expressed by a multiplicative model.

$$D = (d_1 d_2 d_3 \dots d_n)^{1/n} \quad (8-5)$$

Three types of individual desirability function have been proposed based on response's characteristic [128]:

- A. NTB: Nominal-The-Best type: a predicted response is expected to achieve a particular target value
- B. LTB: Large-The-Best type: for the value of a predicated response to be maximized
- C. STB: Smaller-The-Best type: for the value of a predicated response to be minimized

In our specific case, response Y_1 (DI-H₂O compensation) should be minimized while response Y_2 (permeate collection) need to be maximized. Therefore, the corresponding individual desirability function of Y_1 is the SBT type that could be defined as:

$$d_1 = \begin{cases} 0 & \text{if } \hat{Y}_1 \geq Y_1^{\max} \\ \left(\frac{Y_1^{\max} - \hat{Y}_1}{Y_1^{\max} - Y_1^{\min}} \right)^r & \text{if } Y_1^{\min} < \hat{Y}_1 < Y_1^{\max} \\ 1 & \text{if } \hat{Y}_1 \leq Y_1^{\min} \end{cases} \quad (8-6)$$

Accordingly, the corresponding individual desirability function of Y_2 is the LBT type that could be written as:

$$d_2 = \begin{cases} 0 & \text{if } \hat{Y}_2 \leq Y_2^{\min} \\ \left(\frac{\hat{Y}_2 - Y_2^{\min}}{Y_2^{\max} - Y_2^{\min}} \right)^r & \text{if } Y_2^{\min} < \hat{Y}_2 < Y_2^{\max} \\ 1 & \text{if } \hat{Y}_2 \geq Y_2^{\max} \end{cases} \quad (8-7)$$

Where r is a user-specified weight factor ($r > 0$), Y_i^{\min} is the minimum and Y_i^{\max} is the maximum specification limit value of response \hat{Y}_i . In the case of STB responses, a lower value of the response maximizes desirability, $Y_1 = Y_1^{\min}$ such that $d_1 = 1$. Whereas, in the case of an LTB response, a higher value of the response maximizes desirability, $Y_2 = Y_2^{\max}$ such that $d_2 = 1$. The overall desirability, D , is made up of a geometric combination of individual desirability d_i . The value of d_i increases as Y_i moves closer to its desired value. The value assigned to r determines the shape of desirability curve. Underlying transformations experience varied risk preference with different parameter for mixed response type: $r=1$ transformation is risk neutral or linear function; $r<1$ transformation is risk averse or concave function; $r>1$ transformation is risk prone or convex [129]. For the Derringer and Suich method, the risk neutral (linear) and risk averse (concave) transformations tend to approach the original optimal response setting. In our case, r was weighted 1.

Optimization calculation was performed by setting all process variables in experimental range. For two types mixed response, the minimization of DI-H₂O flux compensation with individual desirability equal to 1 can be achieved under the experimental conditions: US output power of 40 W, porosity of permeate spacer of 62.0% and TMP of 20 psi. On the other hand, the maximization of permeate collection with individual desirability equal to 1 can be achieved at: US output power of 120 W, porosity of permeates spacer of 62.0% and TMP of 20 psi. Response desirability profile was computed using Statistica software with spline fit option for desirability surface to get optimum value. As soon as the equation is constructed, predicted values for the dependent variables can be computed at any combination of independent variables.

The prediction profile for desirability consists of a series of graphs as shown in Figure 8-5, one for each independent variable, while holding the levels of the other independent variables constant at specified values. If appropriate specified values for the independent variables have been selected, the prediction profile can show which levels of the predictor variables produce the most desirable predicted response on the dependent variable. Desirability value and predicted responses at various levels of each factor holding all other factors constant at most desirable settings were presented in Table 8-4. The confident interval level was 95% for the estimated range of values. For example, when X_1 was set up at 5 different levels: 40 W, 60 W, 80 W, 100 W and 120 W, the predicted Y_1 , Y_2 and desirability value were produced by setting X_2 and X_3 at their most desirable values, which was 61.0% for X_2 and 20 psi for X_3 .

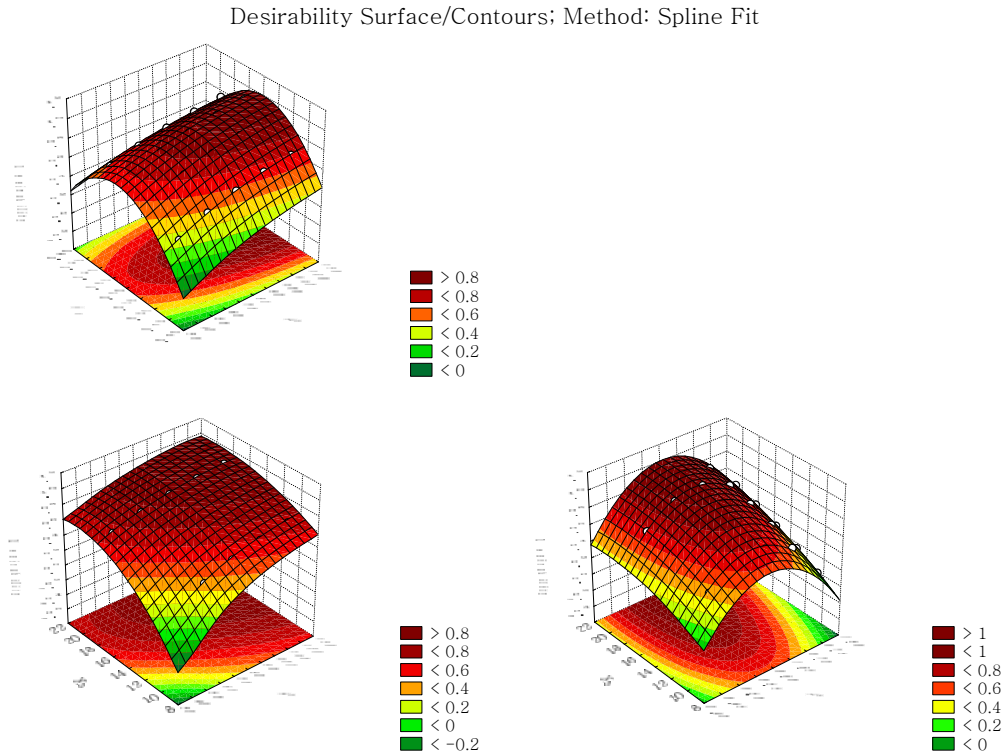


Figure 8-5 Desirability profile

Table 8-4 Desirability value and predicted responses

Factors	Factor level	Predicted Y ₁	Predicted Y ₂	Desirability Value	-95%CI Y ₁	+95%CI Y ₁	-95%CI Y ₂	+95%CI Y ₂
X1	40.	0.007219	324.1356	0.700940	-0.020583	0.035022	306.1551	342.1160
X1	60.	0.009521	351.3764	0.804353	-0.011609	0.030651	337.7109	365.0418
X1	80.	0.010973	374.1776	0.881255	-0.009209	0.031155	361.1254	387.2298
X1	100.	0.011574	392.5392	0.939023	-0.009556	0.032705	378.8738	406.2047
X1	120.	0.011326	406.4613	0.981610	-0.016477	0.039128	388.4808	424.4417
X2	46.2%	0.097379	359.4047	0.695145	0.059534	0.135223	334.9299	383.8795
X2	54.1%	0.021828	391.8882	0.920128	-0.007884	0.051540	372.6727	411.1037
X2	62.1%	0.014449	407.6994	0.978968	-0.013322	0.042220	389.7392	425.6595
X2	70.1%	0.075242	406.8381	0.866619	0.045455	0.105029	387.5743	426.1020
X2	78.0%	0.204207	389.3046	0.533105	0.166277	0.242136	364.7745	413.8346
X3	10.0	0.046853	327.3434	0.664002	0.019048	0.074657	309.3615	345.3253
X3	12.5	0.042207	361.2237	0.790593	0.021075	0.063339	347.5570	374.8904
X3	15.0	0.034737	385.7032	0.879835	0.014553	0.054920	372.6499	398.7565
X3	17.5	0.024441	400.7818	0.942364	0.003309	0.045573	387.1151	414.4485
X3	20.0	0.011321	406.4596	0.981614	-0.016484	0.039125	388.4778	424.4415

The profiles for predicted values and desirability can be plotted with codes and show in Figure 8-6. The results of the developed optimization and overall desirability were presented in Table 8-5. Under the obtained optimal condition: a US output power of 120 W, a spacer porosity of 60.8% and a TMP of 20 psi, the values of the responses were 1.10% and 406.29 g for DI-H₂O compensation and permeate collection. This combination gave the highest overall desirability value 0.9816. The predicted value was very close experimental run no. 8 in Table 8-1, where the output results for two responses were 3.87% and 407.38 g under the condition of US output power of 120 W, spacer porosity of 62% and a TMP of 20 psi.

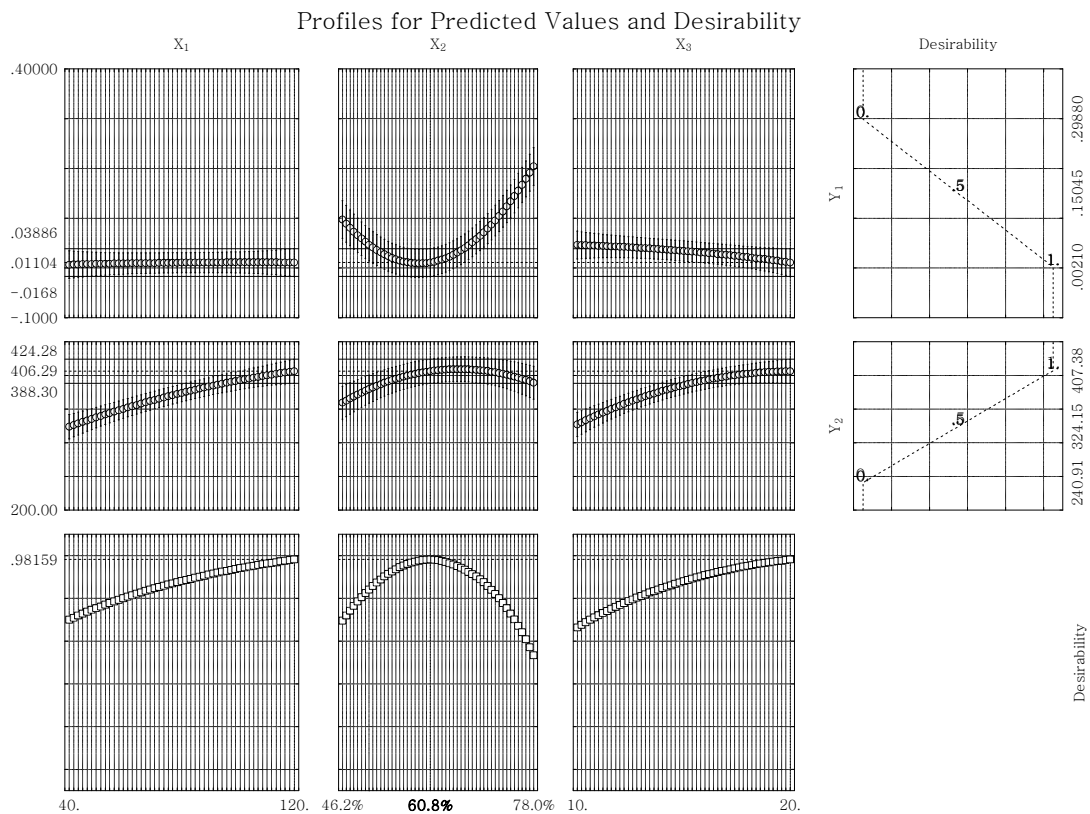


Figure 8-6 Profiles for predicted values and desirability

Table 8-5 Developed optimization condition and overall desirability

Level of X ₁	Level of X ₂	Level of X ₃	Predicted Y ₁	Predicted Y ₂	Desirability Value	-95%CI Y ₁	+95%CI Y ₁	-95%CI Y ₂	+95%CI Y ₂
120.	60.8%	20	0.011043	406.2923	0.981591	-0.016771	0.038858	388.3038	424.2807

8.6. Chapter Summary

The response surface methodology proved to be effective modelling tool for optimization of engineering process. The application of stainless steel permeate spacer with varied porosity in US integrated crossflow system had positive effect on improving the filtration efficiency. The replacement of original propylene spacer with S.S. spacer dramatically magnified the ultrasound irradiation intensity and resulted in a decreased cake layer thickness when dealing with RAE filtration. The optimal operational conditions established by RSM and desirability function approach were as follow: a US output power of 120W, a spacer porosity of 60.8% and a TMP of 20 psi. By applying these process parameter values, maximal responses have been predicted. Under these conditions, the permeation efficiency can be improved up to 211%.

Chapter 9. Conclusions & Recommendation for Future work

9.1. Conclusions

The objectives of this research are to fill the gap in current available ultrasound assisted membrane filtration by developing a novel crossflow filtration module integrated with ultrasound transducers for enhanced membrane fouling resistance.

Astragalus polysaccharides have drawn a great deal of attention in pharmacological research because of their immunomodulatory functions. Polysaccharides extracted from *Astragalus Radix* have a wide MW distribution ranging from 3 kDa to 360 kDa, among which over 40% of polysaccharides has MW greater than 150 kDa. Membrane separation technology has been recognized as a well-developed approach for the concentration and separation of different components from mixtures. A customized Ultrafiltration crossflow module was fabricated to evaluate the permeation profile of *Radix Astragalus* extracts (*RAE*). Two hydrodynamic factors, transmembrane pressure (TMP) and feed velocity, played important roles in flux and fouling profiles of *RAE* UF process. A resistance in series model was applied to characterize the individual fouling resistance, namely, membrane hydraulic resistance, reversible resistance and irreversible resistance. 82% of total resistance followed reversible fouling mechanism and dominated the *RAE* UF process. Comparing to TMP, velocity were more significant in affecting the polysaccharide fouling behaviour.

Ultrasonic irradiation is proved to be an effective approach employed in membrane filtration process. Principle mechanisms involved in ultrasonic membrane cleaning includes acoustic cavitation, acoustic streaming, microstreaming and micro-jets. Ultrasound enhanced UF process for the separation of *RAE* with customized

crossflow filtration module was systematically investigated. Under the effect of mechanical agitation and increased shear forces induced by US irradiation, resistances contributed from concentration polarization and cake layer were significantly reduced. The construction of a looser, more porous fouling cake layer and fine particles agglomeration were confirmed with SEM. Factors including US frequency, US irradiation direction, feed velocity and membrane configurations all had significant impact on the filtration enhancement factors. SEM on membrane morphology as well as ultrasonic power intensity measurements evidenced that no cavitation ever occurred inside the crossflow channel with dynamic flow even when the output power was scaled up to its maximum value. The major effects induced by US in this system were due to acoustic streaming, micro-jets as well as the vibration effect.

Many strategies aiming at enhancing membrane performance involve extra energy input and facilities. Therefore, the requirement of distinguishing the trade-off between productivity and capital cost urges expertise to come across more optimized system design. The sound energy must be intense enough to penetrate the housing and generate cavitation in the designed site. Most laboratory cleaning baths are not sufficiently powerful to achieve the requirement for cavitation bubble collapse after energy transference through housing material. To overcome this problem and to provide high power acoustic energy in crossflow system, a more effective approach where sound energy could impinge directly on medium was then developed. Rather than immersing crossflow module into ultrasonic bath, in our study, a customized crossflow module integrated with ultrasonic transducers was fabricated and operated in stainless steel water bath. A resistance-in-series approach was adapted to evaluate the fouling profile of polysaccharides extracts. The filtration enhancement

factor increased significantly from 1.31 to 2.95 with 28 KHz at 200W input comparing to previous conventional setup. With either continuous or intermitted mode of ultrasonic irradiation, DI-H₂O flux of 30 kDa PES membrane recovered to 100% after 60 minutes filtration with polysaccharides extract. US irradiation dramatically decreased not only the reversible fouling contributed by cake layer and concentration polarization but also the irreversible fouling caused by pore blocking. The distinguished energy distribution in near field and far field in a water bath obtained by Ultrasound intensity measurements strongly supported the filtration enhancement output with integrated module. Membrane morphology characterized with SEM confirmed that no damage occurred to membrane surface after direct irradiation for one hour. Furthermore, GPC results validated that prolonged 60 min US direct irradiation didn't alternative the MW and MW distribution pattern of polysaccharides suspension.

In order to further increase the filtration efficiency, six sets of stainless steel (S.S.) permeate spacers were inserted into crossflow module to evaluate the effect of porosity on permeate flux as well as on RAE filtration enhancement when irradiating with ultrasound in both US enhanced and US integrated system. An extreme condition of taking spacer out of the module was first analyzed. DI-H₂O flux dropped to 45.1 LMH comparing to manufacture value of 150 LMH under same conditions. While the RAE filtration enhancement factor improved by 3.5 folds. Without proper support to membrane, the flow induced higher friction coefficient as well as localized turbulent became reasons for significant DI-H₂O flux loss. In the contrast, under the irradiation of US, these reasons turned into positive driving forces for enhanced permeate. The S.S. permeate spacer with porosity of 62% exhibited the similar DI-H₂O flux at TMP of 15 psi as well as the lowest resistance generated by

this support. The relative RAE filtration enhancement factors presented completely contrary tendencies for two CF systems when plotting as the function of spacer porosity. The different mechanisms of US effect in these two CF systems played important role. The porosity of S.S. spacer as well as the corresponding contact area between membrane the S.S. spacer can tailor the US effect to achieve significant permeate collection. It was reasonable to predicate that there was a range of moderate spacer porosity for which the flux enhancement will be maximized in US integrated system.

The response surface methodology proved to be effective modelling tool for optimization of engineering process. The application of stainless steel permeate spacer with varied porosity in US integrated crossflow system had positive effect on improving the filtration efficiency. The replacement of original propylene spacer with S.S. spacer dramatically magnified the ultrasound irradiation intensity and resulted in a decreased cake layer thickness when dealing with RAE filtration. The optimal operational conditions established by RSM and desirability function approach were as follow: a US output power of 120 W, a spacer porosity of 60.8% and a TMP of 20 psi. By applying these process parameter values, maximal responses have been predicted. Under these conditions, the permeation efficiency can be improved up to 211%.

9.2. Recommendation for Future work

9.2.1. Specific energy consumption in US integrated CF module

Many strategies aiming at improving membrane filtration performance involve extra energy input and additional facilities. As we discussed in previous chapter 4,

simply increasing the feed velocity driven by feed pump could increase the filtration efficiency. The heating effect generated by US in liquid should be utilized. Preliminary test was carried out with S.S permeate spacer porosity of 46.2%, the filtration performance increased 10% with 80 W US power and 20% with 200 W US power without temperature control in the system. The essential target of advanced technology is to reduce the amount of energy required and obtain the same level of improvement. Specific energy consumption in US integrated CF module will be systematically studied associated with pump energy consumption. The capital cost associated with transducers and maintenance expenses must be considered in an industrial application.

Energy consumption was associated with almost all engineering process. Hydraulic pump energy can be calculated by:

$$P_h = q\rho gh \quad (9-1)$$

Where P_h is the power (kW), q is flow capacity (m^3/h), ρ the density of fluid (kg/m^3), g the gravity ($9.81 \text{ m}/\text{s}^2$) and h the differential head (m). Pressure to head conversion:

$$h = \frac{P \cdot 2.31}{\text{specific gravity}} \quad (9-2)$$

Where h the differential head, P the hydraulic pressure and specific gravity is 1.0 for water.

It would be difficult to compare the energy consumption with other researchers since the experimental conditions and methods are varied. By comparing the two hydrodynamic approaches adopted in this work, simply increasing feed flow velocity and introducing US irradiation, at same enhancement level around 90%, energy

consumption was 4.22kW/h as the feed velocity was increased from 0.2 m/s to 0.8 m/s as shown in Figure 9-1. While only 1.26kW/h energy was consumed with 200 W US continuous irradiation under TMP of 15 psi and velocity of 0.2 m/s to achieve equivalent filtration enhancement. After the modification with stainless steel spacer, with optimal condition obtained from chapter 8 by RSM and desirability function approach, namely, a US output power of 120 W, a spacer porosity of 60.8% and a TMP of 20 psi, the energy consumption was 1.53kW/h to be able to maximize the filtration enhancement.

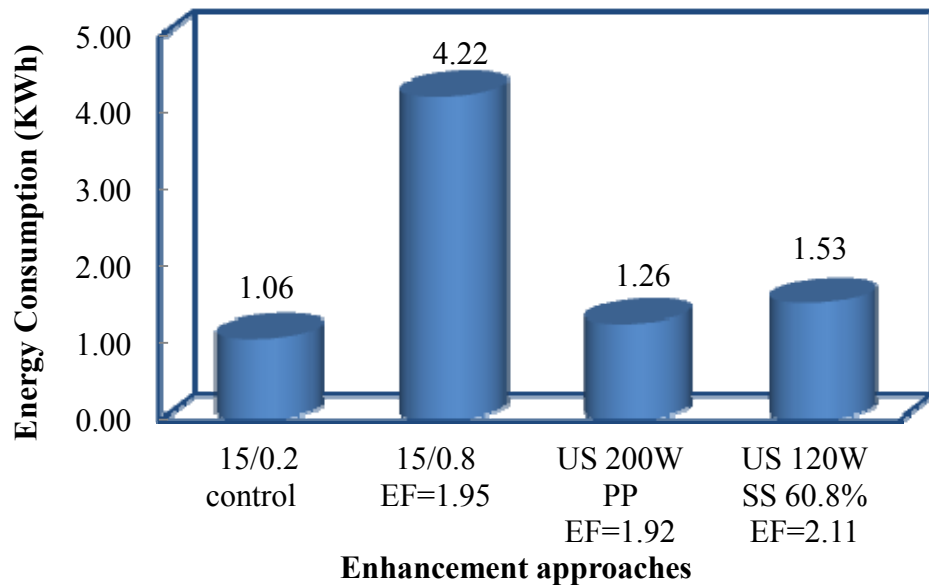


Figure 9-1 Energy consumption in varied filtration processes

9.2.2. Fabrication and optimization of a pilot scale US integrated module

Membrane separation honours intrinsic characteristics of efficiency and operational simplicity, high selectivity and permeability, lower energy consumption and environmental compatibility. In order to apply membrane in industrial scale, a

customized module is required to maximum the membrane surface area and advance the separation efficiency. The choice of module configuration and positioning the module in a system is simply governed by the economic issues and the accurate engineering parameters [53]. According to the properties of target solute and requirements of end product, individual designs have to be properly customized in terms of dead-volume, shear rate, cleaning methods, transmembrane pressure conditions, energy inputs, and flow patterns. Among all configurations, Spiral wound has been proven to be most suitable for Ultrafiltration with higher fouling tendency for its good control process and easy cleaning. The module is constructed with flat sheet membranes layering between feed spacer and permeate carrier materials and rolling into a cylinder, and attached to a permeate tube. Superior structural support inside the module extends the lifetime of membrane in daily operation. Ultrasonic transducer could be attached directly to the spiral wound module instead of immersing in a water bath [130]. In addition to the advantages of high pressure design and low fouling, the spiral wound module requires the lowest capital and operating cost compared with other configurations [131]. Moreover, integrating various membrane filtration techniques into one industrial process may eventually produce each of single purified fractions as shown in Figure 9-2. Therefore, how to incorporate ultrasound transducers in a scale-up spiral wound device and optimize the process design will be our next challenge.

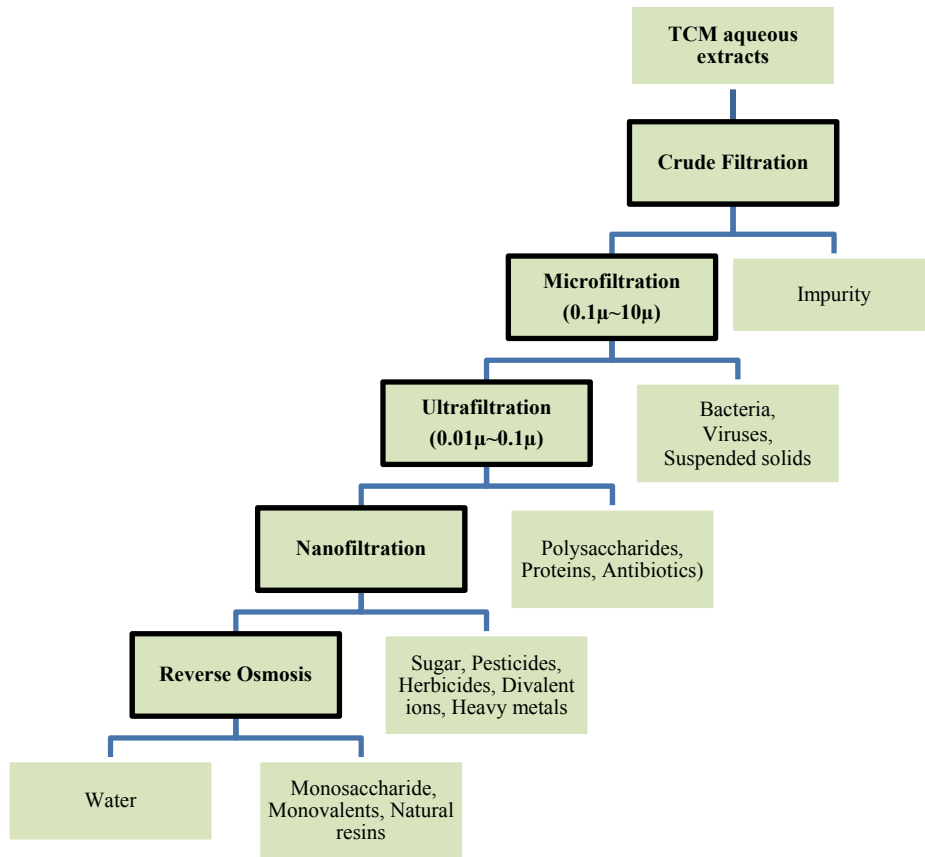


Figure 9-2 Multi-stage recirculation process

REFERENCES

- [1] D. Bensky, S. Clavey and E. Stöger, *Chinese Herbal Medicine :Materia Medica*. Seattle, Wash.: Eastland Press, 2004.
- [2] Y. Jiang, B. David, P. Tu and Y. Barbin, "Recent analytical approaches in quality control of traditional Chinese medicines—A review," *Anal. Chim. Acta*, vol. 657, pp. 9-18, 1/4, 2010.
- [3] S. H. Rizvi, "Membrane applications in biotechnology, food processing, life science, and energy conversion: Introduction," in *Handbook of Membrane Separations*, A. K. Pabby, S. H. Rizvi and A. M. Sastre, Eds. Taylor & Francis Group, 2009, pp. 495.
- [4] R. W. Baker, *Membrane Technology and Applications*. NJ 07030 USA: John Wiley & Sons, Ltd, 2004.
- [5] A. G. Fane and S. Chang. (2009, "Techniques to enhance performance of membrane processes," in *Handbook of Membrane Separations*, A. K. Pabby, S. H. Rizvi and A. M. Sastre, Eds.
- [6] S. Muthukumar, K. Yang, A. Seuren, S. Kentish, M. Ashokkumar, G. W. Stevens and F. Grieser, "The use of ultrasonic cleaning for Ultrafiltration membranes in the dairy industry," *Separation and Purification Technology*, vol. 39, pp. 99-107, 10, 2004.
- [7] S. Kentish and M. Ashokkumar, "Ultrasonic membrane processing," in *Ultrasound Technologies for Food and Bioprocessing*. Food Engineering Series., H. Feng, G. V. Barbosa-Cánovas and J. Weiss, Eds. New York: Springer, 2011, pp. 583-598.
- [8] M. O. Lamminen, H. W. Walker and L. K. Weavers, "Mechanisms and factors influencing the ultrasonic cleaning of particle-fouled ceramic membranes," *J. Membr. Sci.*, vol. 237, pp. 213-223, 7/1, 2004.
- [9] R. Juang and K. Lin, "Flux recovery in the Ultrafiltration of suspended solutions with ultrasound," *J. Membr. Sci.*, vol. 243, pp. 115-124, 11/1, 2004.
- [10] J. Li, D. K. Hallbauer and R. D. Sanderson, "Direct monitoring of membrane fouling and cleaning during Ultrafiltration using a non-invasive ultrasonic technique," *J. Membr. Sci.*, vol. 215, pp. 33-52, 4/15, 2003.
- [11] S. Muthukumar, S. E. Kentish, G. W. Stevens, M. Ashokkumar and R. Mawson, "The application of ultrasound to dairy Ultrafiltration: The influence of operating conditions," *J. Food Eng.*, vol. 81, pp. 364-373, 7, 2007.

- [12] S. Muthukumar, S. Kentish, S. Lalchandani, M. Ashokkumar, R. Mawson, G. W. Stevens and F. Grieser, "The optimisation of ultrasonic cleaning procedures for dairy fouled Ultrafiltration membranes," *Ultrason. Sonochem.*, vol. 12, pp. 29-35, 1, 2005.
- [13] M. Cai, S. Wang, Y. Zheng and H. Liang, "Effects of ultrasound on Ultrafiltration of Radix astragalus extract and cleaning of fouled membrane," *Sep. Purif. Technol.*, vol. 68, pp. 351-356, 8/25, 2009.
- [14] S. Muthukumar, S. E. Kentish, M. Ashokkumar and G. W. Stevens, "Mechanisms for the ultrasonic enhancement of dairy whey Ultrafiltration," *J. Membr. Sci.*, vol. 258, pp. 106-114, 8/1, 2005.
- [15] T. Kobayashi, X. Chai and N. Fujii, "Ultrasound enhanced cross-flow membrane filtration," *Sep. Purif. Technol.*, vol. 17, pp. 31-40, 9/12, 1999.
- [16] H. M. Kyllönen, P. Pirkonen and M. Nyström, "Membrane filtration enhanced by ultrasound: a review," *Desalination*, vol. 181, pp. 319-335, 9/5, 2005.
- [17] M. O. Lamminen, H. W. Walker and L. K. Weavers, "Cleaning of particle-fouled membranes during cross-flow filtration using an embedded ultrasonic transducer system," *Journal of Membrane Science*, vol. 283, pp. 225-232, 10/20, 2006.
- [18] Filtermat Oy. (2004, Solid-free filtrate with ceramic membrane http://www.filtermat.fi/presentation_tiedostot/frame.htm.
- [19] L. Carman, "Filtration Apparatus and Methods," US 5,919,376, Jul 6, 1999.
- [20] Ultrasonically Cleaned Membrane Filtration System, L. K. Weavers. (2006, Mar.7). US 7,008,540 B1 .
- [21] R. V. Crandall, K. Strong and R. Meyer, "Integrated dural cross flow filtration and ultrasonic transducer assembly," US 7,229,562 B2, Jun.12, 2007.
- [22] Q. T. Yu, L. W. Qi and P. Li. (2007, Determination of seventeen main flavonoids and saponins in the medicinal plant huang-qi (radix astragali) by HPLC-DAD-ELSD. *J Sep Sci* 30pp. 1292-1299.
- [23] H. Xiao, X. Liang and P. Lu, "Total analytical method for Radix astragali extract using two-binary multi-segment gradient elution liquid chromatography," *Journal of Separation Science*, vol. 24, pp. 186-196, 2001.
- [24] J. Guan and S. P. Li, "Discrimination of polysaccharides from traditional Chinese medicines using saccharide mapping—Enzymatic digestion followed by chromatographic analysis," *J. Pharm. Biomed. Anal.*, vol. 51, pp. 590-598, 2/5, 2010.

- [25] D. J. Xu, Q. Xia, J. J. Wang and P. P. Wang, "Molecular Weight and Monosaccharide Composition of Astragalus Polysaccharides," *Molecules*, vol. 13, pp. 2408-2415, 2008.
- [26] Q. J. Yan, L. J. Han and Z. Q. Jiang. (2004, Molecular mass distribution of astragalus polysaccharides. *Food Science* 25(8), pp. 27-28.
- [27] G. E. Zaikov, *Chemistry of Polysaccharides*. V.S.P. Intl Science, 2005.
- [28] P. Albersheim. (1976, "The plant cell wall," in *Plant Biochemistry* (3rd ed.), J. Bonner and J. E. Varner, Eds.
- [29] T. Heinze and H. Barseff, *Polysaccharides I :Structure, Characterization and use*. Berlin: Springer, 2005.
- [30] H. Ueno, M. Tanaka, M. Hosino, M. Sasaki and M. Goto, "Extraction of valuable compounds from the flavedo of Citrus junos using subcritical water," *Separation and Purification Technology*, vol. 62, pp. 513-516, 9/22, 2008.
- [31] J. A. Cleary, G. E. Kelly and A. J. Husband. (1999, The effect of molecular weight and b-1,6-linkages on priming of macrophage function in mice by (1,3)-b-D-glucan. *Immu. Cell Bio.* 77pp. 395-403.
- [32] L. E. Craker and J. Giblette. (2002, "Chinese medicinal herbs: Opportunities for domestic production," in *Trends in New Crops and New Uses*, J. Janick and A. Whipkey, Eds.
- [33] K. C. Huang, *The Pharmacology of Chinese Herbs*. Boca Raton: CRC Press, 1993.
- [34] W. J. Zhang, J. Wojta and B. R. Binder, "Regulation of the fibrinolytic potential of cultured human umbilical vein endothelial cells: astragaloside IV downregulates plasminogen activator inhibitor-1 and upregulates tissue-type plasminogen activator expression," *J. Vasc. Res.*, vol. 34, pp. 273-280, 1997.
- [35] H. M. Chang and P. H. But, Eds., *Pharmacology and Applications of Chinese Materia Medica*. Singapore: World Scientific, 2000.
- [36] Y. Yoshida, M. Q. Wang, J. N. Liu, B. E. Shan and U. Yamashita, "Immunomodulating activity of Chinese medicinal herbs and *Oldenlandia diffusa* in particular," *Int. J. Immunopharmacol.*, vol. 19, pp. 359-370, 7, 1997.
- [37] Y. Jiao, J. Wen, X. Yu and D. Zhang, "Influence of flavonoid of astragalus membranaceus's stem and leaf on the function of cell mediated immunity in mice," *Chinese Journal of Integrative Medicine*, vol. 7, pp. 117-120, 2001.
- [38] R. Chang, "Bioactive polysaccharides from traditional Chinese medicine herbs as anticancer adjuvants," *Journal of Alternative and Complementary Medicine* (New York, N. Y.), vol. 8, pp. 559-565, Oct, 2002.

- [39] M. Tomoda, N. Shimizu, N. O⁻hara, R. Gonda, S. Ishii and H. O⁻tsuki, "A reticuloendothelial system-activating glycan from the roots of *Astragalus membranaceus*," *Phytochemistry*, vol. 31, pp. 63-66, 1, 1992.
- [40] K. Kajimura, Y. Takagi and K. Miyano, "Polysaccharide of *Astragali Radix* Enhances IgM Antibody Production in Aged Mice," *Biol. Pharm. Bull.*, vol. 20, pp. 1178-1182, 1997.
- [41] R. A. Bertelsen and D. L. Olsen, "Cross-flow filtration membrane test unit," US 4,846,970, Jul. 11, 1989.
- [42] V. Chen, R. Chan, H. Li and M. P. Bucknall, "Spatial distribution of foulants on membranes during Ultrafiltration of protein mixtures and the influence of spacers in the feed channel," *J. Membr. Sci.*, vol. 287, pp. 79-87, 1/5, 2007.
- [43] S. Geissler, H. Heits and U. Werner, "Description of fluid flow through spacers in flat-channel filtration systems," *Filtration Sep.*, vol. 32, pp. 538-544, 6, 1995.
- [44] S. Geissler and U. Werner, "Dynamic model of crossflow microfiltration in flat-channel systems under laminar flow conditions," *Filtration Sep.*, vol. 32, pp. 533-537, 6, 1995.
- [45] P. F. Levy and R. S. Earle, "The effect of channel height and channel spacers on flux and energy requirements in crossflow filtration," *J. Membr. Sci.*, vol. 91, pp. 135-143, 5/20, 1994.
- [46] J. Lipnizki and G. Jonsson, "Flow dynamics and concentration polarisation in spacer-filled channels," *Desalination*, vol. 146, pp. 213-217, 9/10, 2002.
- [47] S. Ma and L. Song, "Numerical study on permeate flux enhancement by spacers in a crossflow reverse osmosis channel," *J. Membr. Sci.*, vol. 284, pp. 102-109, 11/1, 2006.
- [48] J. Schwinge, P. R. Neal, D. E. Wiley, D. F. Fletcher and A. G. Fane, "Spiral wound modules and spacers: Review and analysis," *J. Membr. Sci.*, vol. 242, pp. 129-153, 10/15, 2004.
- [49] L. N. Sim, Y. Ye, V. Chen and A. G. Fane, "Comparison of MFI-UF constant pressure, MFI-UF constant flux and Crossflow Sampler-Modified Fouling Index Ultrafiltration (CFS-MFIUF)," *Water Res.*, vol. 45, pp. 1639-1650, 2, 2011.
- [50] L. N. Sim, Y. Ye, V. Chen and A. G. Fane, "Crossflow Sampler Modified Fouling Index Ultrafiltration (CFS-MFIUF)—An alternative Fouling Index," *J. Membr. Sci.*, vol. 360, pp. 174-184, 9/15, 2010.
- [51] A. Subramani, S. Kim and E. M. V. Hoek, "Pressure, flow, and concentration profiles in open and spacer-filled membrane channels," *J. Membr. Sci.*, vol. 277, pp. 7-17, 6/1, 2006.

- [52] S. K. Karode and A. Kumar, "Feed Spacer for filtration membrane modules," US 6,989,097 B2, Jan 24, 2006.
- [53] M. Mulder. (1996, Basic Principles of Membrane Technology (2nd ed.) .
- [54] Q. Zhang, L. Li, L. Liu, Y. Li, L. Yuan, L. Song and Z. Wu, "Effects of the polysaccharide fraction of *Urtica fissa* on castrated rat prostate hyperplasia induced by testosterone propionate," *Phytomedicine*, vol. 15, pp. 722-727, 9/3, 2008.
- [55] A. U. Buranov and G. Mazza, "Extraction and purification of ferulic acid from flax shives, wheat and corn bran by alkaline hydrolysis and pressurised solvents," *Food Chem.*, vol. In Press, Corrected Proof, .
- [56] S. Yongxu and L. Jicheng, "Structural characterization of a water-soluble polysaccharide from the Roots of *Codonopsis pilosula* and its immunity activity," *Int. J. Biol. Macromol.*, vol. 43, pp. 279-282, 10/1, 2008.
- [57] R. Cozzolino, P. Malvagna, E. Spina, A. Giori, N. Fuzzati, A. Anelli, D. Garozzo and G. Impallomeni, "Structural analysis of the polysaccharides from *Echinacea angustifolia radix*," *Carbohydr. Polym.*, vol. 65, pp. 263-272, 8/15, 2006.
- [58] F. Dourado, P. Madureira, V. Carvalho, R. Coelho, M. A. Coimbra, M. Vilanova, M. Mota and F. M. Gama, "Purification, structure and immunobiological activity of an arabinan-rich pectic polysaccharide from the cell walls of *Prunus dulcis* seeds," *Carbohydr. Res.*, vol. 339, pp. 2555-2566, 10/20, 2004.
- [59] P. Rai, C. Rai, G. C. Majumdar, S. DasGupta and S. De, "Resistance in series model for Ultrafiltration of mosambi (*Citrus sinensis* (L.) Osbeck) juice in a stirred continuous mode," *J. Membr. Sci.*, vol. 283, pp. 116-122, 10/20, 2006.
- [60] G. Belfort, R. H. Davis and A. L. Zydney, "The behavior of suspensions and macromolecular solutions in crossflow microfiltration," *J. Membr. Sci.*, vol. 96, pp. 1-58, 11/28, 1994.
- [61] B. Tansel, J. Sager, J. Garland and S. Xu, "Effect of transmembrane pressure on overall membrane resistance during cross-flow filtration of solutions with high-ionic content," *J. Membr. Sci.*, vol. 328, pp. 205-210, 2/20, 2009.
- [62] J. G. Wijmans, S. Nakao and C. A. Smolders, "Flux limitation in Ultrafiltration: Osmotic pressure model and gel layer model," *J. Membr. Sci.*, vol. 20, pp. 115-124, 8, 1984.
- [63] M. Zhang and L. Song, "Mechanisms and Parameters Affecting Flux Decline in Cross-Flow Microfiltration and Ultrafiltration of Colloids," *Environ. Sci. Technol.*, vol. 34, pp. 3767-3773, 09/01, 2000.
- [64] L. Song, "Flux decline in crossflow microfiltration and Ultrafiltration: mechanisms and modeling of membrane fouling," *Journal of Membrane Science*, vol. 139, pp. 183-200, 2/18, 1998.

- [65] S. Nataraj, R. Schomäcker, M. Kraume, I. M. Mishra and A. Drews, "Analyses of polysaccharide fouling mechanisms during crossflow membrane filtration," *J. Membr. Sci.*, vol. 308, pp. 152-161, 2/1, 2008.
- [66] G. P. Baruah, G. Belfort and A. Venkiteswaran. (2005, Global model for optimizing crossflow microfiltration and Ultrafiltration processes: A new predictive and design tool. *Biotechnol. Prog.* 21pp. 1013-1025.
- [67] T. Huang, H. B. Zhou and Y. Q. Lai, "Filtration study on aqueous extractives of *Ficus Microcarpa* L.f. with vibratory shear enhanced membrane filtration ," *Food and Drug*, vol. 9, pp. 11-14, 2007.
- [68] B. A. Auld, *Acoustic Fields and Waves in Solids*. Krieger Publishing Company, 1990.
- [69] C. V. Subramanian, *Practical Ultrasonics*. Narosa, 2006.
- [70] Inficon, "Density and Acoustic Impedance Values <http://www.inficonthinfilmdesposition.com/en/densityandacousticvalues.html>, " 2011.
- [71] P. P. Delsanto, N. K. Batra, R. B. Mignogna and M. Scalerandi, "Parallel processing simulations of the propagation of ultrasonic waves through material interfaces," *Ultrasonics Symposium, 1998. Proceedings.* , 1998 IEEE, vol. 2, pp. 1129-1138 vol.2, 1998.
- [72] A. Arnau, *Piezoelectric Transducers and Applications*. Berlin, Heidelberg: Springer Berlin Heidelberg, 2008.
- [73] E. G. Brun, "Ultrasonic transducer and method of joining an ultrasonic," US 7,161,280 B2, Jan 9, 2007.
- [74] J. A. Johnson, "Numerical calculations of ultrasonic field I: Transducer near fields," *Journal of Nondestructive Evaluation*, vol. 3, pp. 25-35, 1982.
- [75] Lord Rayleigh, "On the pressure developed in a liquid during the collapse of a spherical cavity," *Phil. Mag.*, vol. 34, pp. 94-98, 1917.
- [76] M. Kornfeld and L. Suvorov, "On the destructive action of cavitation," *J. Appl. Phys.*, vol. 15, pp. 495-506, 1944.
- [77] T. B. Benjamin and A. T. Ellis, "The collapse of cavitation bubbles and the pressures thereby produced against solid boundaries," *Phil. Trans. Roy. Soc.*, vol. A, pp. 221-240, 1966.
- [78] N. D. Shutler and R. B. Mesler, "A photographic study of the dynamics and damage capabilities of bubbles collapsing near solid boundaries," *Trans. ASME J. Basic Engr.*, vol. D, pp. 116-124, 1965.
- [79] J. R. Blake, N. H. Thomas and J. M. Boulton-Stone, *Bubble Dynamics and Interface Phenomena :Proceedings of an IUTAM Symposium Held in*

- Birmingham, U.K., 6-9 September, 1993. Dordrecht; Boston: Kluwer Academic Publishers, 1994.
- [80] K. S. Suslick, Ed., *Ultrasound its Chemical, Physical, and Biological Effects*. 1988.
- [81] F. J. Fuchs, "Ultrasonic Cleaning: Fundamental Theory and Application," pp. 14, 2002.
- [82] P. D. Edmonds, Ed., *Ultrasonics (Methods in Experimental Physics)*. Academic Press, 1981.
- [83] E. A. Brujan, T. Ikeda and Y. Matsumoto, "On the pressure of cavitation bubbles," *Exp. Therm. Fluid Sci.*, vol. 32, pp. 1188-1191, 4, 2008.
- [84] M. Arora, C. D. Ohl and D. Lohse, "Effect of Nuclei Concentration on Cavitation Cluster Dynamics," *The Journal of the Acoustical Society of America*, vol. 121, pp. 3432-3436, 2007.
- [85] L. A. Crum, "Comments on the evolving field of sonochemistry by a cavitation physicist," *Ultrason. Sonochem.*, vol. 2, pp. S147-S152, 1995.
- [86] M. Beck. (2010, Precision cleaning megasonic cleaning charts a course to the big time. 2011(Jun.), Available:
http://www.prosystmeg.com/technology/articles/precision_cleaning2.php.
- [87] T. G. Leighton, *The Acoustic Bubble*. London: Academic Press, 1994.
- [88] T. G. Leighton, A. J. Walton and M. J. W. Pickworth, "Primary Bjerknes forces," *Eur. J. Phys.*, vol. 11, pp. 47, 1990.
- [89] J. Laborde, C. Bouyer, J. -. Caltagirone and A. Gérard, "Acoustic bubble cavitation at low frequencies," *Ultrasonics*, vol. 36, pp. 589-594, 2, 1998.
- [90] S. Luther, R. Mettin, P. Koch and W. Lauterborn, "Observation of acoustic cavitation bubbles at 2250 frames per second," *Ultrason. Sonochem.*, vol. 8, pp. 159-162, 7, 2001.
- [91] S. Muthukumar, S. E. Kentish, G. W. Stevens and M. Ashokkumar, "Application of Ultrasound in Membrane Separation Processes: A Review," *Reviews in Chemical Engineering*, vol. 22, pp. 155-194, 2006.
- [92] L. Thompson and L. Doraiswamy. (1999, Sonochemistry: Science and engineering. *Ind. Eng. Chem. Res.* 38pp. 1215-1249.
- [93] J. Hermia, "Constant pressure blocking filtration laws-application to power-law non-newtonian fluids," *Trans. IChemE*, vol. 60, pp. 183-187, 1982.
- [94] C. G. de Kruif and R. Tuinier, "Polysaccharide protein interactions," *Food Hydrocoll.*, vol. 15, pp. 555-563, 7/11, 2001.

- [95] W. C. S. Cho and K. N. Leung, "In vitro and in vivo immunomodulating and immunorestorative effects of *Astragalus membranaceus*," *J. Ethnopharmacol.*, vol. 113, pp. 132-141, 8/15, 2007.
- [96] I. M. Lipatova and A. P. Moryganov, "Mechanoinitiated structural and chemical transformations in solutions and liquid dispersions of polysaccharides," in *Chemistry of Polysaccharides*, G. E. Zaikov, Ed. 2005, pp. 294-343.
- [97] S. C. Szu, G. Zon, R. Schneerson and J. B. Robbins, "Ultrasonic irradiation of bacterial polysaccharides. Characterization of the depolymerized products and some applications of the process," *Carbohydrate Research*, vol. 152, pp. 7-20, 9/1, 1986.
- [98] Q. Gan, J. A. Howell, R. W. Field, R. England, M. R. Bird and M. T. McKechnie, "Synergetic cleaning procedure for a ceramic membrane fouled by beer microfiltration," *J. Membr. Sci.*, vol. 155, pp. 277-289, 4/12, 1999.
- [99] Y. Lee and M. M. Clark, "Modelling of flux decline during crossflow Ultrafiltration of colloidal suspensions," *J. Membr. Sci.*, vol. 149, pp. 181-202, 10/28, 1998.
- [100] Y. Ye, P. L. Clech, V. Chen and A. G. Fane, "Evolution of fouling during crossflow filtration of model EPS solutions," *J. Membr. Sci.*, vol. 264, pp. 190-199, 11/1, 2005.
- [101] A. Maskooki, T. Kobayashi, S. A. Mortazavi and A. Maskooki, "Effect of low frequencies and mixed wave of ultrasound and EDTA on flux recovery and cleaning of microfiltration membranes," *Sep. Purif. Technol.*, vol. 59, pp. 67-73, 2/1, 2008.
- [102] K. K. Latt and T. Kobayashi, "Ultrasound-membrane hybrid processes for enhancement of filtration properties," *Ultrason. Sonochem.*, vol. 13, pp. 321-328, 5, 2006.
- [103] T. Kobayashi, T. Kobayashi, Y. Hosaka and N. Fujii, "Ultrasound-enhanced membrane-cleaning processes applied water treatments: influence of sonic frequency on filtration treatments," *Ultrasonics*, vol. 41, pp. 185-190, 5, 2003.
- [104] T. J. Mason and J. P. Lorimer, *Applied Sonochemistry: Uses of Power Ultrasound in Chemistry and Processing*. Wiley-VCH Verlag GmbH & Co. KGaA, 2002.
- [105] E. Riera-Franco de Sarabia, J. A. Gallego-Juárez, G. Rodríguez-Corral, L. Elvira-Segura and I. González-Gómez, "Application of high-power ultrasound to enhance fluid/solid particle separation processes," *Ultrasonics*, vol. 38, pp. 642-646, 3, 2000.
- [106] A. Simon, L. Penpenic, N. Gondrexon, S. Taha and G. Dorange, "A comparative study between classical stirred and ultrasonically-assisted dead-end Ultrafiltration," *Ultrason. Sonochem.*, vol. 7, pp. 183-186, 10, 2000.

- [107] D. Veerasamy, A. Supurmaniam and Z. M. Nor, "Evaluating the use of in-situ ultrasonication to reduce fouling during natural rubber skim latex (waste latex) recovery by Ultrafiltration," *Desalination*, vol. 236, pp. 202-207, 1/31, 2009.
- [108] J. L. Kost R.S., "Ultrasound enhancement of membrane permeability," *4,780,212*, Oct. 25, 1988.
- [109] A. Moussatov, C. Granger and B. Dubus, "Cone-like bubble formation in ultrasonic cavitation field," *Ultrason. Sonochem.*, vol. 10, pp. 191-195, 7, 2003.
- [110] I. P. Marangopoulos, C. J. Martin and J. M. S. Hutchison. (1995, Measurement of field distributions in ultrasonic cleaning baths: Implications for cleaning efficiency. *Phys. Med. Biol.* 40pp. 1897-1908.
- [111] Y. P. Zhang, A. G. Fane and A. W. K. Law, "Critical flux and particle deposition of fractal flocs during crossflow microfiltration," *J. Membr. Sci.*, vol. 353, pp. 28-35, 5/1, 2010.
- [112] G. Belfort, "Membrane modules: comparison of different configurations using fluid mechanics," *J. Membr. Sci.*, vol. 35, pp. 245-270, 2, 1988.
- [113] N. Heinen, "Permeate spacer module," US 2006/0191837 A1, Aug 31, 2006.
- [114] L. Rui, C. Wei-chang, W. Wei-peng, T. Wen-yan and Z. Xue-guang, "Optimization of extraction technology of Astragalus polysaccharides by response surface methodology and its effect on CD40," *Carbohydr. Polym.*, vol. 78, pp. 784-788, 11/17, 2009.
- [115] N. K. Singh, A. Parmar and D. Madamwar, "Optimization of medium components for increased production of C-phycoerythrin from *Phormidium ceylanicum* and its purification by single step process," *Bioresource Technology*, vol. 100, pp. 1663-1669, 2, 2009.
- [116] Z. Liao, G. Wang, X. Liang, G. Zhao and Q. Jiang, "Optimization of microwave-assisted extraction of active components from Yuanhu Zhitong prescription," *Separation and Purification Technology*, vol. 63, pp. 424-433, 10/22, 2008.
- [117] I. Xiarchos, A. Jaworska and G. Zakrzewska-Trznadel, "Response surface methodology for the modelling of copper removal from aqueous solutions using micellar-enhanced Ultrafiltration," *Journal of Membrane Science*, vol. 321, pp. 222-231, 8/15, 2008.
- [118] Q. Dong, J. Yao, J. Fang and K. Ding, "Structural characterization and immunological activity of two cold-water extractable polysaccharides from *Cistanche deserticola* Y. C. Ma," *Carbohydrate Research*, vol. 342, pp. 1343-1349, Jul 23, 2007.
- [119] G. Hanrahan and K. Lu, "Application of Factorial and Response Surface Methodology in Modern Experimental Design and Optimization," *Critical Reviews in Analytical Chemistry*, vol. 36, pp. 141-151, 2006.

- [120] J. A. Cornell, *How to Apply Response Surface Methodology*. Amer Society for Quality, 1990.
- [121] M. Khayet, C. Cojocaru and G. Zakrzewska-Trznadel, "Response surface modelling and optimization in pervaporation," *J. Membr. Sci.*, vol. 321, pp. 272-283, 8/15, 2008.
- [122] S. L. C. Ferreira, R. E. Bruns, H. S. Ferreira, G. D. Matos, J. M. David, G. C. Brandão, E. G. P. da Silva, L. A. Portugal, P. S. dos Reis, A. S. Souza and W. N. L. dos Santos, "Box-Behnken design: An alternative for the optimization of analytical methods," *Anal. Chim. Acta*, vol. 597, pp. 179-186, 8/10, 2007.
- [123] A. Jokić, Z. Zavargo, Z. Šereš and M. Tekić, "The effect of turbulence promoter on cross-flow microfiltration of yeast suspensions: A response surface methodology approach," *J. Membr. Sci.*, vol. 350, pp. 269-278, 3/15, 2010.
- [124] R. Malaisamy, G. Annadurai and D. Mohan, "Performance optimization of polysulfone Ultrafiltration membranes for riboflavin separation using design experiments," *Bioprocess and Biosystems Engineering*, vol. 22, pp. 227-232, 2000.
- [125] M. Khayet, M. N. A. Seman and N. Hilal, "Response surface modeling and optimization of composite nanofiltration modified membranes," *J. Membr. Sci.*, vol. 349, pp. 113-122, 3/1, 2010.
- [126] C. Pizarro, J. M. González-Sáiz and N. Pérez-del-Notario, "Multiple response optimisation based on desirability functions of a microwave-assisted extraction method for the simultaneous determination of chloroanisoles and chlorophenols in oak barrel sawdust," *Journal of Chromatography A*, vol. 1132, pp. 8-14, 11/3, 2006.
- [127] N. R. Costa, J. Lourenço and Z. L. Pereira, "Desirability function approach: A review and performance evaluation in adverse conditions," *Chemometrics Intellig. Lab. Syst.*, vol.107, pp.234-244, 2011.
- [128] G. Derringer and R. Suich, "Simultaneous Optimization of Several Response Variables," *J. Qual. Technol.*, vol. 12, pp. 214-218, 1980.
- [129] J. F. Kros and C. M. Mastrangelo, "Comparing Multi-response Design Methods with Mixed Responses," *Qual. Reliab. Eng. Int.*, vol. 20, pp. 527-539, 2004.
- [130] A. Maskooki, S. A. Mortazavi and A. Maskooki, "Cleaning of spiralwound Ultrafiltration membranes using ultrasound and alkaline solution of EDTA," *Desalination*, vol. 264, pp. 63-69, 12/15, 2010.
- [131] N. S. Krishna Kumar, M. K. Yea and M. Cheryan, "Ultrafiltration of soy protein concentrate: performance and modelling of spiral and tubular polymeric modules," *J. Membr. Sci.*, vol. 244, pp. 235-242, 11/15, 2004.